

Development of Hydrogen-Permselective
SiCH-based Organic-Inorganic Hybrid Membranes

水素選択透過性SiCH系
有機・無機ハイブリッド膜の創製

Miwako Kubo
January 2021

Nagoya Institute of Technology

Contents

Chapter 1 Introduction

1.1	Trends in Energy Resources	1
1.2	Production Methods of Hydrogen	2
1.2.1	Hydrogen Production by Steam-Reforming	3
1.2.2	Hydrogen Production via Photoelectrochemical (PEC) Water-Splitting	3
1.3	Hydrogen Separation Systems	5
1.4	Membranes Separation	6
1.4.1	Silica Membranes for Hydrogen Separation	9
1.4.1.1	Mesoporous γ -Al ₂ O ₃ Layer and its Surface Property	10
1.4.2	Organic-Inorganic Hybrids	11
1.4.2.1	Polymer-Derived Ceramics (PDCs) Route	12
1.4.2.2	Polycarbosilanes (PCSs)	14
1.5	Gas Permeation Mechanisms through Porous Membranes	15
1.5.1	Gas Permeances Measurement	24
1.6	Object of Present Study	26
1.7	Outline of This Thesis	28
	References	30

Chapter 2 A hydrostable mesoporous γ -Al₂O₃ membrane modified with SiCH-based organic-inorganic hybrid derived from polycarbosilane

2.1	Introduction	39
2.2	Experimental Procedures	39
2.2.1	Fabrication of mesoporous γ -Al ₂ O ₃ membrane on a macroporous α -Al ₂ O ₃ support	39
2.2.2	Surface modification of γ -Al ₂ O ₃ membrane with SiCH- based organic-inorganic hybrid	41
2.2.3	Characterizations	43
2.3	Results and Discussion	44
2.3.1	Hydrophilic/Hydrophobic characteristics	44
2.3.2	Modification of mesoporous γ -Al ₂ O ₃ membrane on a macroporous support	46
2.3.3	Effect of SiCH-modification on gas permeation properties of mesoporous γ -Al ₂ O ₃ membrane	47
2.3.3.1	Gas permeation behaviors under dry condition	47
2.3.3.2	Gas permeation behaviors under wet condition	49
2.4	Summary	52
	References	52

Chapter 3	Hydrogen selective SiCH-based organic-inorganic hybrid/γ-Al₂O₃ composite membranes	
3.1	Introduction	55
3.2.	Experimental Procedures	56
3.2.1	Preparation of the supported mesoporous γ -Al ₂ O ₃ membrane	56
3.2.2	Modification of a supported γ -Al ₂ O ₃ membrane with AHPCS-derived organic-inorganic SiCH hybrid	56
3.2.3	Characterizations	57
3.3	Results and Discussion	60
3.3.1	Heat treatment temperatures selected for highly cross-linked SiCH-based organic-inorganic hybrid synthesis	60
3.3.2	Hydrophobicity	64
3.3.3	Properties of SiCH hybrid/ γ -Al ₂ O ₃ composite membrane	64
3.4	Summary	74
	References	75
Chapter 4	Superhydrophobic polycarbosilane membranes for purification of solar hydrogen	
4.1	Introduction	78
4.2	Experimental Procedures	79
4.2.1	Synthesis of PCS membranes	79
4.2.2	Characterizations	80
4.3	Results and Discussion	81
4.3.1	Hydrophobicity of as-received PCSs	81
4.3.2	Properties of supported PCS membranes	83
4.3.3	Analysis of gas permeation behaviors	89
4.4	Summary	97
	References	98
Chapter 5	Conclusions	101
	List of Publication	104
	Acknowledgement	105

Chapter 1

Introduction

1.1 Trends in Energy Resources

Energy resources have been no exception, the global economy has been dealt a heavy blow by the impact of the novel coronavirus disease 2019 (COVID-19) infection that has spread around the world since January 2020. In terms of a crude oil, representing fossil fuels making up most of primary energy sources in Japan, crude oil prices have been highly volatile since January 2020, as shown in Fig. 1-1. Instability of market prices of the crude oil prevents a stable supply of an electrical energy. In broad sense, a stable supply of a secondary energy is prevented by the market prices of primary energy resources which are sensitive to international conditions.

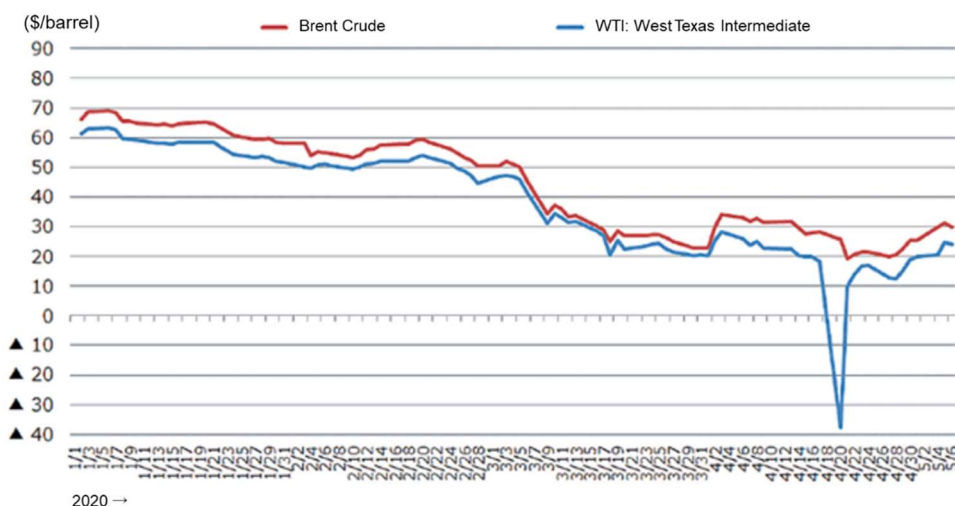


Fig. 1-1. The price movements of the crude oils since January 2020 [1].

For Japan which currently relies on imported primary energy resources, diversifications of primary energy resources supply system which are aimed at remedying the fragile supply structures of the primary energy resources are very important. As one of the means for diversifications of primary energy resources supply system, introduction of a hydrogen energy which can be produced from various energy sources has been promoted.

Hydrogen has been attracting much attention as a clean and sustainable substitute energy for fossil fuels. Hydrogen has high energy yield of 120 J g^{-1} which is about 2.8 times higher than hydrocarbon fuels [2]. Moreover, the combustion product is water and thus completely clean in a carbon dioxide (CO_2)-neutral manner.

According to “Hydrogen Basic Strategies” formulated in December 26, 2017 [3], introduction of a hydrogen energy contributes to the achievement of the goals of “3E+S” which is a basic target of the energy policy: Energy Security, Economic Efficiency and Environment with Safety [4] as shown in Fig. 1-2.

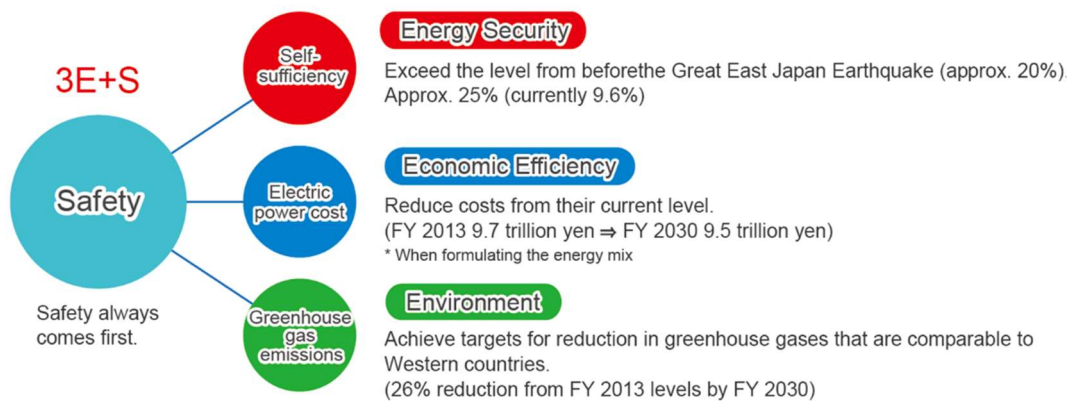


Fig. 1-2. The basic principle of Japan’s energy policy (3E+S) toward 2030 [5].

Hydrogen is the lightest flammable gas on earth. In a mixed gas of hydrogen and oxygen, hydrogen reacts in large range of concentration, 4~95 % [6]. However, adequate control of hydrogen can ensure its safety. In terms of the energy security, hydrogen can be produced from a wide variety of energy sources, and then produced hydrogen can be stored and transported. This means that hydrogen can be supplied from any location, regardless of domestically and internationally. In other words, the introduction of hydrogen energy can not only improve self-sufficiency of primary energy, but also ensure a constant supply of energy, even if energy supply suddenly declines or stops. Concerning the economic efficiency, it is undeniable that the cost of utilization of hydrogen is more expensive than that of conventional fossil fuels. However, considering the depletion of fossil fuels and its environmental burden, the potential for cost reduction by the utilization of hydrogen will be very high in the medium- to long-term. Finally, hydrogen does not emit carbon dioxide when it is used. Adopting production methods, which does not emit carbon dioxide even at the production stage, can make it possible to achieve low-carbon society from hydrogen productions to hydrogen uses in total.

Based on the above, a development of innovative technologies for the production, transportation, storage and utilization of hydrogen is necessary to realize the hydrogen society and to diffuse the use of hydrogen in full scale [3]. The following section explains production methods of hydrogen.

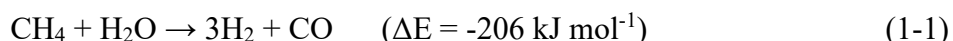
1.2 Production Methods for Hydrogen

As mentioned above, hydrogen can be produced from a wide variety of energy sources. Moreover, hydrogen can be produced using several resources including hydropower, nuclear energy and renewable energy sources like biomass, wind, geothermal and solar. Currently, hydrogen is produced industrially by reforming fossil fuels, or produced as byproducts from steelworks and the soda industry [4]. There are also some other methods with low-carbon technique, biomass and water-splitting. The

following sub-section explains hydrogen productions by steam-reforming and via photoelectrochemical water-splitting representing conventional and novel hydrogen production methods, respectively.

1.2.1 Hydrogen Production by Steam-Reforming

Currently, steam-reforming of natural gas [7–9] has become the mainstream of the hydrogen (H₂) production method. For example, methane (CH₄, main constituent of natural gas) is converted to H₂ and carbon monoxide (CO) through this method as follows.



This reaction is endothermic, so that the steam-reforming reaction is performed at high temperature, approximately 800 °C. In this method, the synthesis gas then proceeds to a CO shift reaction which can convert steam and CO into more H₂ and carbon dioxide (CO₂).



Finally, high purity H₂ can be extracted from the syngas mixture through the Pressure Swing Adsorption (PSA) process. In PSA, a strong adsorbate (CO₂ as impurities) is adsorbed and a weak adsorbate (H₂ as a target gas) extracted from the syngas mixture under higher pressure conditions, while the strong adsorbate in adsorbent (such as molecular sieve or zeolite) can be desorbed and recovered at lower pressure. The target gas in the syngas mixture is purified by repeated adsorption and desorption of impurities.

Steam-reforming is an industrially established method and has few technical problems, but it produces carbon dioxide as a byproduct. However, the application of carbon dioxide capture and storage (CCS) can be substantially low carbon. [4]

1.2.2 Hydrogen Production via Photoelectrochemical (PEC) Water-Splitting

Recently, as one of new approaches for H₂ production, novel solar hydrogen production system has been studied. A representative example is hydrogen production via photoelectrochemical (PEC) water-splitting which has received increased attention as an environmental-friendly and low-cost solar-to-hydrogen pathway because of its potential for high conversion efficiency at low operating temperatures using cost-effective semiconductor-based photoreaction catalysts [10–12].

The PEC reaction simultaneously generates H₂ and oxygen (O₂) by an oxidation-reduction reaction of water under sunlight in the presence of semiconducting catalysts.



This reaction produces H₂ even at low temperature without CO and CO₂ emission. Accordingly, this reaction has a big advantage compared with the conventional steam-reforming reactions.

The solar hydrogen production systems are expected to be used in terms of global-warming prevention and a stable supply of energy. Therefore, in Japan, the research and development of these systems have been promoted by the Ministry of Economy, Trade and Industry (METI). For example, as an ongoing New Energy and Industrial Technology Develop Organization (NEDO) R&D project, the “Artificial Photosynthesis” Project has been conducted by the Japan Technological Research Association of Artificial Photosynthetic Chemical Process (ARPCChem) [13,14]. In this project, photocatalyst sheets with two type of particulate photocatalysts, which use solar energy to produce hydrogen from water, has been developed [15]. A conceptual diagram of the water-splitting process on the surface of the sheet is shown in Fig. 1-3.

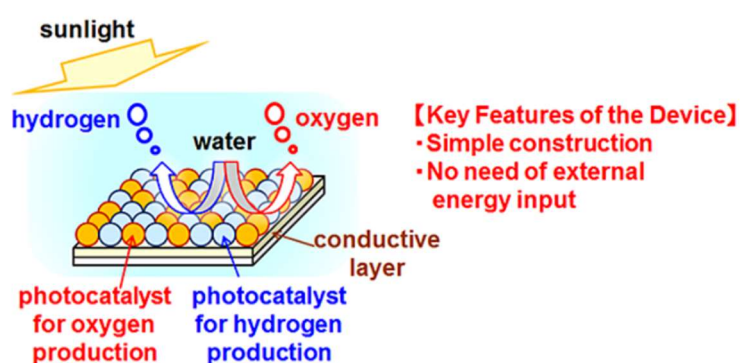
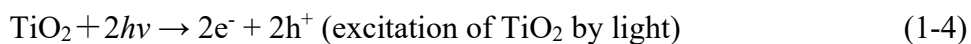


Fig. 1-3. The conceptual diagram of the water-splitting process on the surface of the particulate photocatalyst sheet [15].

The principle of the solar hydrogen production system is based on the Honda-Fujishima effect [16]. This is a very simple reaction of splitting water with light energy. A titanium dioxide (TiO_2) electrode, which is immersed in an aqueous electrolyte solution, induces oxygen evolution from the TiO_2 electrode and hydrogen evolution from a platinum (Pt) counter electrode, when visible light is irradiated to the TiO_2 electrode and some anodic bias (0.5 V) is applied to that. Therefore, water can be decomposed by visible light into oxygen and hydrogen, according to the following schemes:



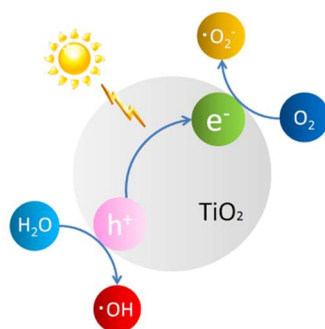


Fig. 1-4. Schematic diagram of photocatalytic H₂O splitting [17].

Recently, a modified aluminum-doped strontium titanate (SrTiO₃:Al) photocatalyst on which the cocatalysts Rh/Cr₂O₃ for hydrogen evolution reactions and CoOOH for oxygen evolution reactions are depositing are used. The hydrogen and oxygen evolution reactions could be promoted separately, because both cocatalysts are deposited on different crystal facets of SrTiO₃:Al [18].

A diagram of the project mentioned above is shown in Fig. 1-5. The solar hydrogen production system of the project is composed of three reactions, water photo-splitting, H₂ separation and CO₂ hydrogenation. After water photo-splitting, H₂ must be separated from the solar product gas with water vapor (Fig. 1-5 (1)). The solar product gas contains H₂ and O₂ which react in large range of H₂ concentration, 4~95% [6]. So that speedy separation of H₂ from solar product gas needs at low temperature (≤ 50 °C) under the wet condition (10 %) [13,14,19], and membrane separation is one of the potential candidates as an energy-saving separation process. Hydrogen purification methods are described in detail in the next section.

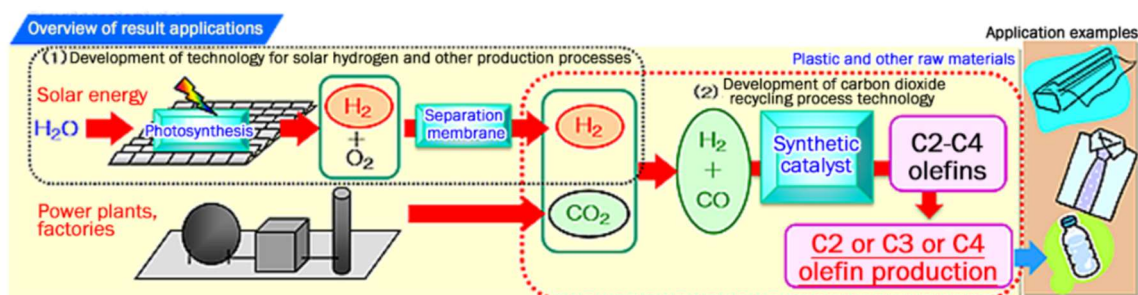


Fig. 1-5. Schematic diagram of the artificial photosynthesis project [14].

1.3 Hydrogen Separation Systems

Since H₂ and O₂ react in a large range of H₂ concentration, the hydrogen production system requires an efficient separation technology for purifying H₂ from the syngas containing O₂. There are several candidate technologies for H₂ purification such as cryogenic distillation, pressure swing adsorption (PSA) and membrane separation.

The cryogenic distillation can separate inorganic and organic gases which have low boiling point by liquefying them at low temperatures. The PSA can separate the desorbed gas with decompression after adsorb the mixed gas under high pressure, due to the nature of the different adsorption forces of each substance to the adsorbent, as described previously. The cryogenic distillation and the PSA are generally not cost effective and are quite energetically demanding for the separation and purification of H₂ [20].

Meanwhile the membrane separation shows some advantages including energy efficiency and simple separation schemes suitable for establish safe operation process for the separation and purification of H₂.

1.4 Membranes Separation

Membranes for hydrogen separation are classified according to the composition of the selective layer: metallic membranes represented by palladium (Pd)-based membranes [21–24], polymer membranes [25] and microporous ceramic membranes represented by silica membranes [26–28].

Dense metallic membranes are commonly used for high purity hydrogen separation. The steps of the hydrogen separation are following: as shown in Fig. 1-6(a), (1) reversible dissociative adsorption of molecular hydrogen on the metallic membrane surface, (2) dissolution of atomic hydrogen into the bulk metal of the membrane, (3) diffusion of atomic hydrogen through the membrane, (4) association of hydrogen atoms on the other surface of membrane, (5) desorption of molecular hydrogen from the surface, and diffusion of molecular hydrogen away from the surface [23].

Polymer membranes have been commercially used for H₂ purification from ammonia purge gas, coke oven gas, petroleum refining gas, and steam reforming gas [19,29]. Dominant gas transport through dense polymer membranes is governed by the solution-diffusion mechanism, and the total permeance of gas molecule (gas-*i*) is a product of the solubility (S) and the diffusivity (D):

$$Q_i = S \times D \quad (1-7)$$

However, under the given operating conditions temperature (≤ 50 °C under the wet condition) of the solar hydrogen production [13,14,19], it is difficult to apply these membranes, which require higher operation temperatures for H₂ separation, approximately above 90 and 350 °C for polymer [25], and metal membranes [21,22,24], respectively.

Moreover, another drawback which should be taken into consideration for dense metallic membranes is that the metal matrix tends to catalyze the reverse reaction of molecular H₂ with O₂ to afford H₂O on the membrane surface (Fig. 1-6(a)).

On the other hand, the intrinsic technical issue for the polymer membranes is water-induced swelling: by assuming the H₂ separation for the solar hydrogen production, Tanaka *et al.* [19] investigated H₂/O₂ separation by using a polyimide hollow-fiber

membrane (PI-HF). The H₂ permeance and H₂/O₂ selectivity of the PI-HF under the humid condition at low temperature were lower than those under dry condition. High water absorbing property of the polymer matrix results in plasticization, that is the swelling as shown in Fig. 1-6 (b), which causes degradation of H₂-selectivity.

Recently, supported ionic liquid membranes (SILMs) [30,31] and supported liquid membranes (SLMs) [32–34] have been investigated for H₂/O₂ separation at low temperature. SILMs and SLMs consist of a porous support on which liquid is impregnated and separate gases by the difference in solubility and diffusivity of each gas species in the liquid at room temperature [35]. The H₂ permeance and H₂/O₂ selectivity reported for the SILMs were 10⁻¹⁰ to 10⁻⁹ mol m⁻² s⁻¹ Pa⁻¹ order and below 4, respectively. The H₂ permeances reported for the SLMs were also in the same order, while the H₂/O₂ selectivities measured for the SLMs using liquid perfluorocarbon (PFC) such as perfluorotributylamine (PFTBA) [34] and perfluorooctanol (PFO) [33] were 140 and 100, respectively. However, PFTBA and PFO were volatile, and thus these PFC-based SLMs were not sufficiently stable for practical applications. In short, H₂ permeance through SILMs and SLMs is insufficient under the given operating conditions of the solar hydrogen production [13,14,19]. Moreover, in humid condition, Castro-Dominguez *et al.* [32] reported that O₂-permeance of the SLM for H₂/O₂ selectivity increased associated with the weight loss of the supported liquid film. The liquid film might be broken up by water molecules, as a result, water molecules formed paths which could be allowed to permeate O₂ molecules.

Ceramic membranes divide into porous ceramic membranes and dense ceramic membranes. One of the dense ceramics, solid proton conductors can also function as the H₂-separation systems. There are both a hydrogen pumping and a H₂-separation membrane. As for the hydrogen pumping, when an electrochemical cell with electrodes attached to the gas feed side and gas permeation side of the dense ceramic membrane, which is consisted of BaCe_{0.95}Y_{0.05}O_{3-x} or SrCe_{0.95}Y_{0.05}O_{3-x} having proton conductivity, is applied direct current, H₂ can be extracted from feed gas and pumped to the electrode of permeation side yielding pure hydrogen [36]. On the other hand, H₂ can be extracted from feed gas without electronic power supply by using the solid proton-electron hole mixed conductors such as Ce_{0.97}Sr_{0.03}PO_{4-y}, as a membrane material [37]. However, such proton conductors require high-operating temperatures of several hundred °C.

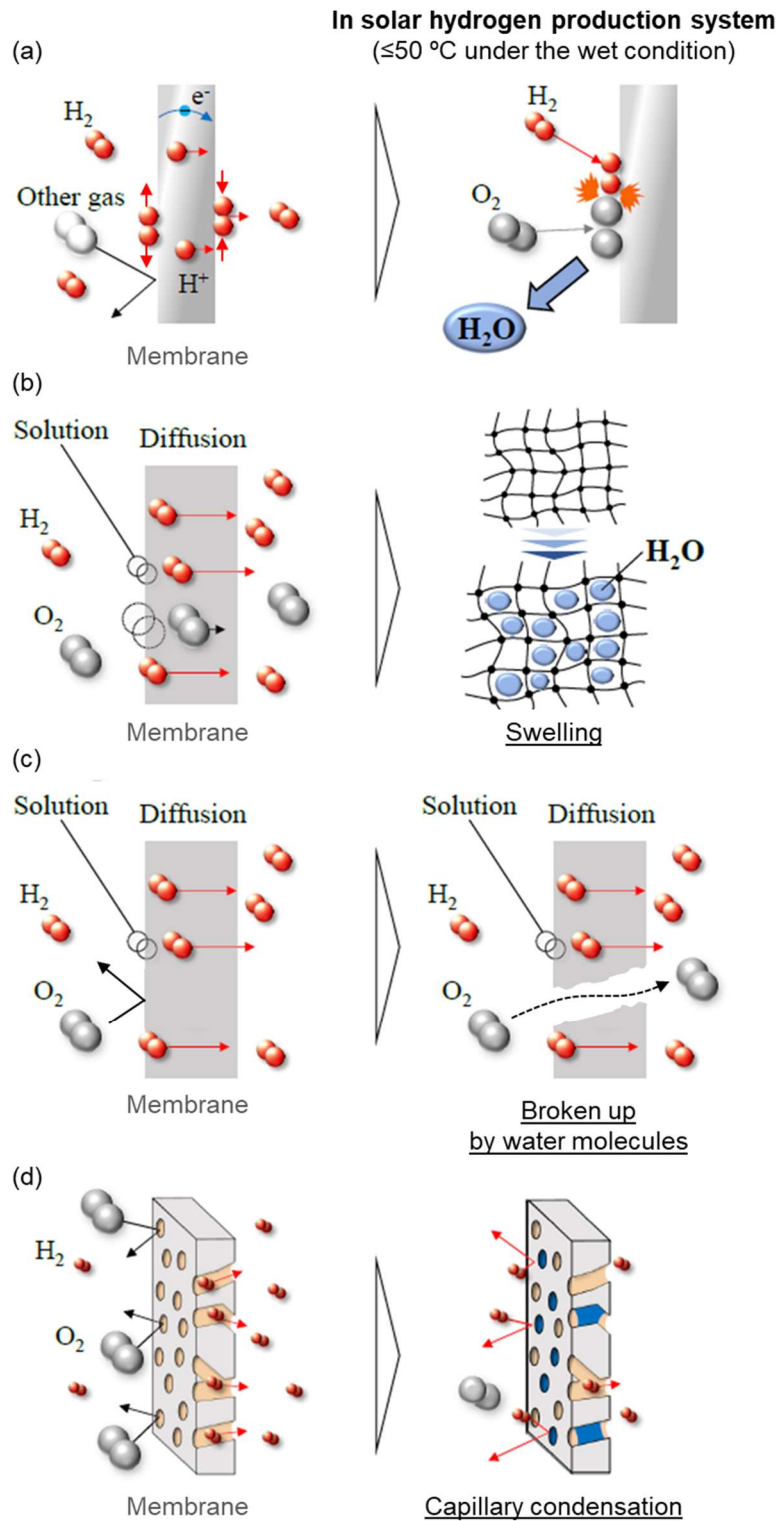


Fig. 1-6. Schematic images of H_2 separation by a (a) dense metallic membrane, (b) polymer membrane, (c) supported liquid membrane (SLM) and (d) microporous ceramic membrane, and the technical issue for each membrane applied to the solar hydrogen purification system.

On the other hand, porous ceramic membranes have been extensively studied because of their superior chemical resistance and heat resistance, and present high gas separation properties. The gas separation of the porous ceramic membranes is thought to be achieved by the molecular sieve-like property due to the sub-nanometers order pores, and thus porous ceramic membranes with strictly controlled microporosity in sub-nanometer range show high selectivity. Moreover, H₂-separation through the porous ceramic membranes can be operated at relatively lower temperatures. As for the humidity, at least, swelling observed in the polymer membranes and film-broken up observed in SMLs by water molecules are not to become a technical issue for H₂-separation of the porous ceramic membranes. Therefore, the porous ceramic membranes have a certain potential to apply the solar hydrogen production system which is operated at low temperatures (≤ 50 °C) under the wet condition (10 %) [13,14,19].

1.4.1 Silica Membranes for Hydrogen Separation

Amorphous silica (SiO₂) with highly controlled micropores is useful as an active separation layer for H₂ separation. As the kinetic diameters of H₂ and O₂ are 0.289 and 0.346 nm [38], respectively, the H₂ permselectivity of microporous amorphous SiO₂ membranes have been thought to be achieved by the molecular sieve-like property derived from the amorphous silica network with micropores of about 0.3 nm [39], as shown in Fig. 1-7.

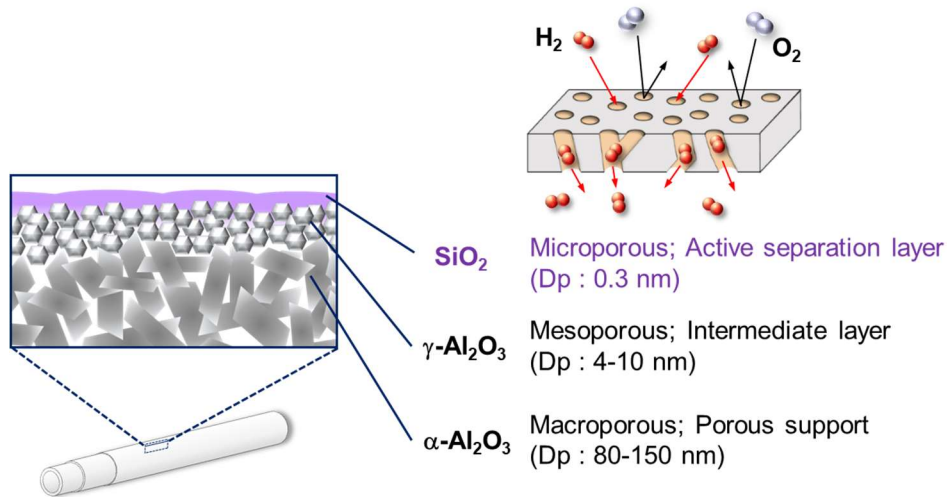


Fig. 1-7. Multi-layered structure of the H₂-permselective microporous amorphous silica membrane fabricated on a mesoporous γ-Al₂O₃ intermediate layer over a macroporous α-Al₂O₃ support.

Compared with SLMs, microporous amorphous SiO₂ membranes show higher H₂ permeance with high H₂ selectivity at high temperatures [7,39–42]. However, under humid condition at around room temperature, serious performance degradation occurs by

blockage of H₂-permeable micropore channels through the surface silanol-induced water monomolecular layer adsorption [43] followed by capillary condensation of water molecules [19,44] as shown in Fig. 1-6 (c). Under humid condition at low temperature, first, water molecules permeated into pores are adsorbed on surface silanol groups ($\equiv\text{Si-OH}$) of the micropores amorphous silica via hydrogen bonding, therefore monomolecular layer adsorption arises [43]. Next, multilayer adsorption dominated by water-water interactions at the silica surfaces causes capillary condensation [44], which leads to the degradation of the H₂ separation performance of the microporous amorphous silica membranes [19].

Moreover, microporous amorphous SiO₂ membranes have been fabricated in the form of multilayered composite membranes, consisting of an active SiO₂ surface layer (active separation layer), a mesoporous intermediate layer, and a macroporous support, as shown in Fig. 1-7. Therefore, in addition to microporous amorphous SiO₂, hydrostability in terms of the stable gas permeations under the humid condition of mesoporous intermediate layer is an additional issue. Generally, α -alumina (Al₂O₃) and γ -Al₂O₃ have been used for the macroporous support and the mesoporous intermediate layer which is placed between the microporous amorphous SiO₂ on the top and the macroporous support, respectively.

1.4.1.1 Mesoporous γ -Al₂O₃ Layer and its Surface Property

α -Al₂O₃ has excellent chemical stability in both acidic and basic pH, while γ -Al₂O₃ is not stable as in the case of α -Al₂O₃ [45–48]. Gestel *et al.* [47] investigated chemical stability of TiO₂/ γ -Al₂O₃/ α -Al₂O₃ (porous support) multilayered composite nanofiltration (NF) membranes and, the stability was discussed based on the corrosion behaviors of each membrane component material at ambient temperature. It was suggested that the chemical stability of the multilayered composite membranes could be governed by the crystallinity of γ -Al₂O₃: Weakly crystallized γ -Al₂O₃ layer fabricated at 400 °C to 600 °C is restricted to mild aqueous media (pH 3-11) or non-aqueous media (organic solvents). Higher fabricating temperature above 600 °C promoted phase transformation from γ - to δ - and θ -Al₂O₃, and the corrosion resistance of Al₂O₃ improved substantially. However, it was impossible to achieve sufficient resistance.

Recently, Duke *et al.* [48] investigated pervaporation of ammonia-solution using γ -Al₂O₃ supported organosilica membrane to understand ammonia removal performance and the membrane material stability under high pH environment (pH 11) at 45 °C to 70 °C. The analytical results by Fourier transform (FT)-IR spectrum, gas porosimetry, scanning electron microscopy (SEM) and X-ray diffraction (XRD) revealed that only slight change in organosilica chemistry and structure was evident, however more significant degradation was observed in the supporting γ -Al₂O₃ layer.

Concerning high-temperature stability under humid condition, *i.e.* hydrothermal stability of mesoporous γ -Al₂O₃ has been studied for application to novel membrane reactors to improve efficiency of methane steam-reforming operated at around 500 °C. The hydrothermal stability of H₂-selective multilayered composite membrane composed

of counter-diffusion CVD-derived microporous SiO₂/sol gel-derived mesoporous γ -Al₂O₃/ α -Al₂O₃ porous support has been investigated, and the performance degradation was found to be due to the defect formations at the SiO₂/ γ -Al₂O₃ hetero interface by the hydrothermally induced densification of microporous SiO₂ and pore growth of γ -Al₂O₃[49,50]. It should be noted that mixed dopants such as gallium (Ga) and lanthanum (La) [51,52], cerium (Ce) and zirconium (Zr)[53,54], and single dopant of nickel (Ni)[55] have been reported as effective to improve the hydrothermal stability in terms of stable gas permeations through the mesoporous γ -Al₂O₃ membranes, and the multilayered composite membrane of CVD-derived microporous SiO₂/Ni-doped mesoporous γ -Al₂O₃/ α -Al₂O₃ porous support showed better H₂ separation membrane performance under the hydrothermal condition at 500 °C [50].

For maintaining stable gas permeations under humid condition, γ -Al₂O₃ surface property in terms of hydrophilicity/hydrophobicity is also important. Similar to other oxide ceramics, γ -Al₂O₃ membranes exhibit hydrophilic character because of the presence of surface hydroxyl (-OH) groups which are favorable adsorption sites for water molecules [56–59]. The hydrophilic character provides high polar surface properties derived from the adsorption of water molecules via a hydrogen bond [60]. Since, a strong adhesion between the surface of Al₂O₃ membrane and foulants (such as deposition and adsorption of proteins in protein separation processes) leads to the membrane fouling, a highly hydrophilic character of the Al₂O₃ membrane surface has been suggested as preferable [61]. On the other side, hydrophobic surface is required as membranes for separations through membrane distillation process: Owing to the liquid water repellent property, solutes in the liquid water cannot transport through the porous ceramic membranes, while water vapor can permeate through the membranes. The hydrophobic porous ceramic-based membranes have been prepared by surface modification with fluoroalkylsilanes (FAS) [57,62–68] or perfluoroalkylsilanes (PFAS) [69,70] and explored for desalination of water, concentration of liquids and wastewater.

1.4.2 Organic-Inorganic Hybrids

Degradations of the H₂ separation performance for the polymer membranes and the amorphous SiO₂ membranes at low temperature under humid condition are discussed previously. To suppress the degradations of the H₂ separation performance of the amorphous SiO₂ membranes, hydrophobization of the amorphous SiO₂ can be made by the following methods: Si-OH groups on the surface are substituted by other organic functional groups (Si-R) to reduce Si-OH groups, or organic cross-linked structures are introduced into the Si-O network to suppress formation of Si-OH, *i.e.* as an appropriate material category, organic-inorganic hybrids are appropriate for these methods.

Recently, increasing attention has been directed to organic-inorganic hybrid materials as promising functional materials in various fields such as optics, electronics and energy. Synergistic properties of hybrid materials can be achieved by harmonizing advantageous properties of an organic component, such as solubility, plasticity and hydrophobicity, with those of an inorganic component such as high strength and thermal

and/or chemical stability [71,72]. In other words, the properties of the organic-inorganic hybrids are not just the sum of the individual contributions from both phases. The role of the inner interfaces can be predominant. The nature of the interface has been used recently to divide these materials into two distinct classes. In class I, organic and inorganic compounds are embedded and only weak bonds (hydrogen, van der Waals or ionic bonds) give the cohesion to the whole structure. In class II, two phases are mainly linked together through strong chemical bonds (covalent or ionocovalent bonds). [73]

1.4.2.1 Polymer-Derived Ceramics (PDCs) Route

Polymer-Derived Ceramics (PDCs) route has been known as a practicable method to produce silicon (Si)-based non-oxide ceramics [74–77]. One of potential advantages of this route is that polymerization and cross-linking provide a means to vary the specific properties of the pre-ceramic polymers, such as solubility, fusibility, or viscosity, extensively providing the versatility in processing and shaping capabilities, including surface coating, thin film and long fiber syntheses which are similar to those successfully achieved with organic polymer materials.

Moreover, the PDCs route is an efficient approach for the synthesis of novel organic-inorganic hybrids, especially categorized as Class II hybrids according to the classification given by Sanchez [73], where the organic and inorganic components are linked together by strong chemical bonds, by polymerization and thermal or chemical cross-linking of polymers. Moreover, this process can provide a means to vary the specific properties of the polymers such as solubility and viscosity, which provides the versatility in shaping capabilities including the formation of surface coatings and membranes.

This PDCs route is composed of the following four steps [75] as shown in Fig. 1-8. For the synthesis organic-inorganic hybrids, first, precursor polymers or oligomers are synthesized from monomer units. The as-synthesized precursors are cross-linked to form two- or three- dimensional preceramic network structures to afford organic-inorganic hybrids.

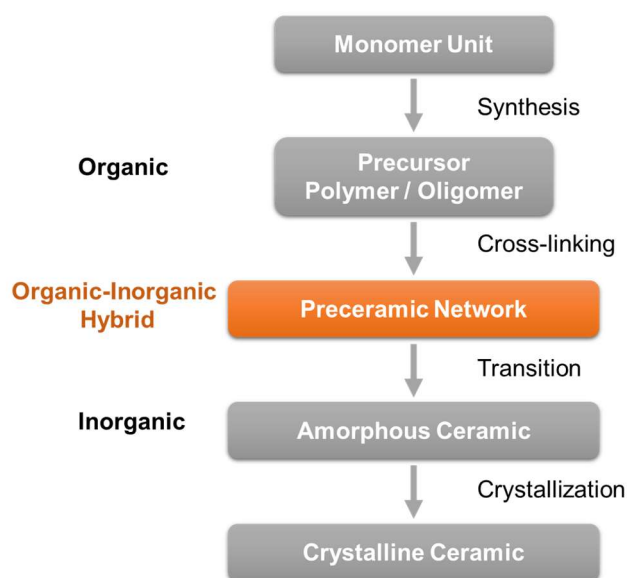


Fig. 1-8. Flow diagram showing synthesis of ceramics via organic-inorganic hybrids through Polymer-Derived Ceramics (PDCs) route.

Wilhelm and Rezwan *et al.* [78–88] reported that porosity in the micro to macropore range and the hydrophilic/hydrophobic surface character of silicon oxycarbide (SiOC) organic-inorganic hybrids and amorphous SiOC ceramics could be systematically controlled by varying mixing ratio of starting methyl polysiloxane/methyl-phenyl polysiloxane and heat treatment temperature [78]. This route has been further extended to develop functional SiOC-based porous materials by use of aminopropyltriethoxysilane and potassium chloride for meso- and macro-porosity formation, respectively [79], mixing with sewage sludge for developing novel adsorbents for removing pharmaceuticals from aqueous solutions [80], tailoring the surfactant concentration in the oil/water emulsion-based monolithic hybrids syntheses [81], use of passive fillers such as alumina platelets and silica spheres for macroporosity controlling in the synthesis of porous ceramic monoliths by freeze casting [82], and use of silicon carbide passive filler with azodicarbonamide as a macropore former in the syntheses of ceramic tapes [83]. In addition to adjusting the porosity and surface property, organo-amino group functionalization has been successfully achieved for the polysiloxane-derived SiOC organic-inorganic hybrids for developing gas adsorbents [84,85]. Moreover, in-situ compositing routes for synthesizing novel CO₂ methanation catalysts, transition metal (M) nanoparticle-dispersed SiOC ceramics (M=Ni [86-88], Co [87]) have been developed.

Polysiloxane derivatives, polydimethylsiloxanes (PDMSs) have been investigated to render hydrophilic membrane surface into hydrophobic by surface modification [89–92]. Compared with fluoroalkylsilanes, PDMS-derived SiOC organic-inorganic hybrid

exhibits better thermal stability up to 300 °C in air [93,94], and the organic component contributes to the hydrophobic surface character, while the inorganic component can be expected to enhance the durability [92].

To synthesize another SiOC organic-inorganic hybrid for membrane separation, perhydropolysilazane (PHPS) is chemically modified with various alcohols or ethers, and resulting polymer precursors are successfully converted to amorphous silica-based organic-inorganic hybrids by exposure to vapors from aqueous ammonia at room temperature [59]. Si-O-C₁₀H₂₁ is an efficient terminated structure for amorphous silica-based organic-inorganic hybrid materials with improved hydrophobicity. However, these hybrid materials are composed of Si-O-Si (silica) network, therefore high permeation temperature is essentially required to obtain high H₂-permselectivities, as with conventional microporous amorphous silica membrane. Moreover, these materials are still difficult to achieve high hydrophobicity due to the presence of polar oxygen atoms that are easy to form hydrogen-bonding to water, *i.e.* offering preferential adsorption sites for water molecules.

1.4.2.2 Polycarbosilanes (PCSs)

Instead of the silica-based organic-inorganic hybrid, polycarbosilanes (PCSs), hydrophobic organic-inorganic hybrid polymers having Si-C backbone with methyl groups as organic substituents [95], is expected to apply for H₂-permselective membranes. The chemical structure of polycarbosilanes and polycarbosilane derivatives is shown in Fig. 1-9. PCSs are well known as precursors for silicon carbide (SiC)-based ceramics [96,97] for PDCs route.

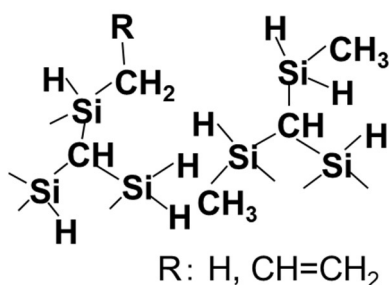


Fig. 1-9. Typical chemical structure of polycarbosilane derivatives (R: H, CH=CH₂).

Their synthesis by the Kumada rearrangement of polydimethylsilane (PDS) has been reported by Yajima *et al.* [96]. Since polymer-derived amorphous silicon (oxy)carbide (SiC and SiCO) show excellent thermal and chemical stabilities [74,98], polydimethylsilane (PDS) [99], PCSs [100–106] and PCS derivatives such as allyl-hydro-polycarbosilane (AHPCS) [107–111] have been applied as precursors of microporous amorphous SiOC [99–103] and SiC [98,104–111] membranes to investigate their gas permeation properties mainly at high temperatures, $T \geq 200$ °C. PCSs are also appropriate as functional Class II hybrids: The silicon-carbon (Si-C) backbone endows several attractive properties of PCSs such as high flexibility and excellent thermal, chemical and

electrical stabilities [112–114]. The hydrocarbon groups attached to the Si-C backbone provide room temperature stability in air and PCSs can be applied as an active binder for the formation of powder compact to fabricate polycrystalline SiC ceramics [115–118].

Moreover, PCSs having many organic structures are expected to show excellent hydrophobic properties. PCSs have Si-C network structure, as a replacement of the silica network structure of the silica-based organic-inorganic hybrid which cannot show high H₂-permselectivity at low temperature, so that PCS-derived organic-inorganic hybrid membranes are expected to show high H₂-permselectivities under the given low-temperatures of the solar hydrogen production.

However, little research has been done for the PCS-derived SiCH organic-inorganic hybrid membranes as H₂ separation membranes, especially under the present humid condition below 50 °C, and there has had no data reported for H₂ permselectivity, even other organic-inorganic hybrid membranes.

1.5 Gas Permeation Mechanisms through Porous Membranes

The ceramic membranes with porous structures include metal oxides (for example, SiO₂, Al₂O₃ and TiO₂) and zeolite, non-oxide ceramics (for example, Si-C, Si-C-N and Si-B-C-N), and carbons. Pores of the porous ceramic membranes act as the paths of the gas molecules. The flux, J [mol m⁻² s⁻¹] and permeance, Q [mol m⁻² s⁻¹ Pa⁻¹] are given by following equations,

$$J = \frac{V}{A} = \frac{V}{\pi r_p^2} \quad (1-8)$$

$$Q = \frac{J}{(p_H - p_L)} \quad (1-9)$$

where V is the permeation rate [mol s⁻¹], A is the membrane surface area [m²], r_p is the pore radius [m], p_H is the pressure of the gas feed side [Pa] and p_L is the pressure of the gas permeate side [Pa].

The dominant mechanism for gas permeation through the porous ceramic membranes depends on the pore size and the interaction between the permeate gas molecules and the pore wall.

The interaction is involved mean free path, molecular weight and kinetic diameter of the permeate gas molecule. The relation between the pore diameter d_p [m] and the mean free path [119,120] of the gas- i molecule λ_i [m] is determined Knudsen number K_n [-] according to the following equations,

$$\lambda_i = \frac{RT}{\sqrt{2}\sigma_i N_A p} = \frac{RT}{\sqrt{2}(\pi r_{k,i}^2) N_A p} \quad (1-10)$$

$$K_n = \frac{\lambda_i}{d_p} \quad (1-11)$$

where R is the gas constant [$\text{J mol}^{-1} \text{K}^{-1}$], T is the permeation temperature [K], σ_i is the scattering cross section [m^2], $r_{k,i}$ is the effective radius [m] which measures the range of interatomic forces, N_A is the Avogadro constant [mol^{-1}] and p is the pressure [Pa]. The gas permeation mechanisms include (a) viscous flow, (b) Knudsen diffusion, (c) Molecule sieving, (d) surface diffusion, (e) gas-translational diffusion and (f) solid-state diffusion [121], as shown in Fig. 1-10.

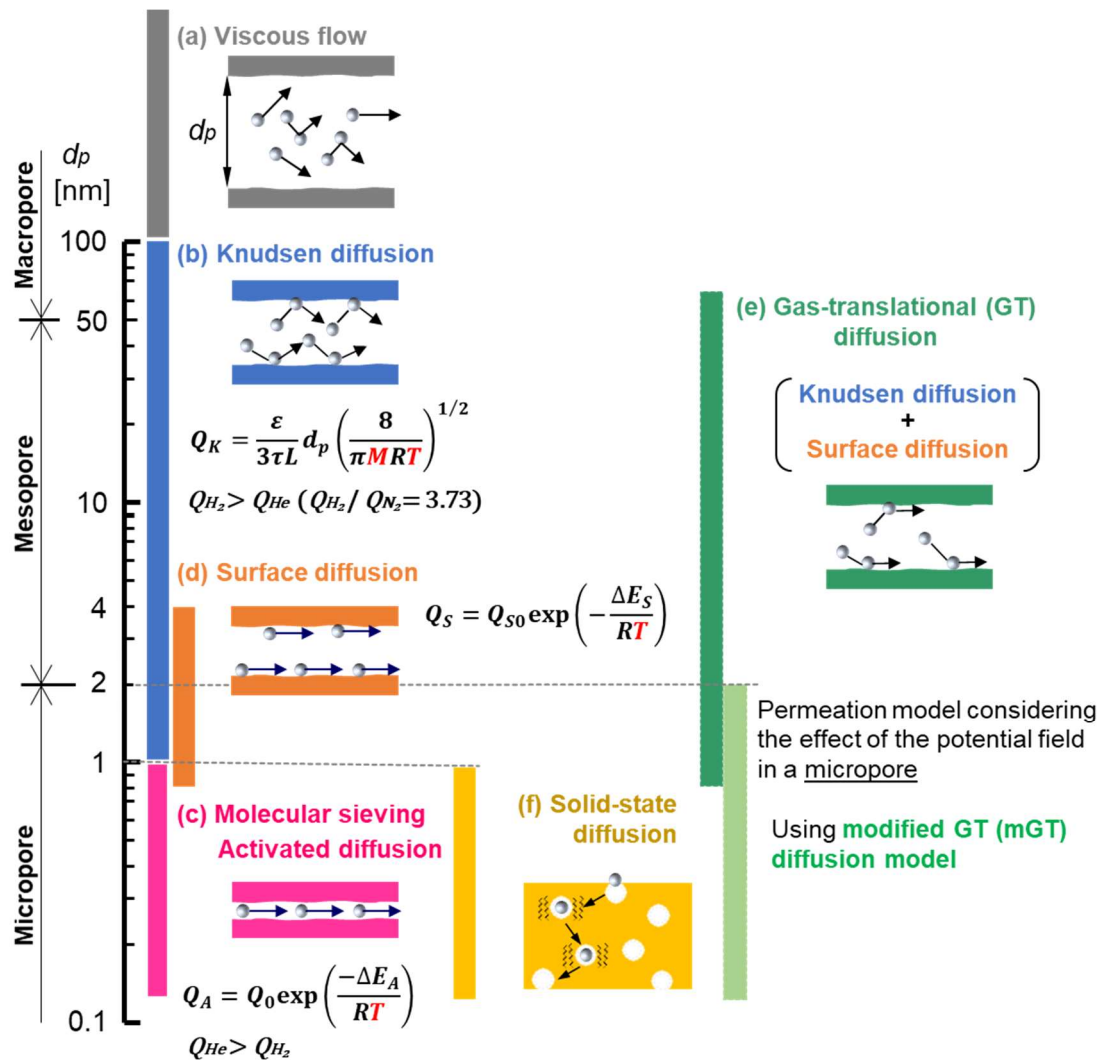


Fig. 1-10. Relationship between pore diameter of the porous ceramics membranes and various gas permeation mechanisms: (a) viscous flow, (b) Knudsen diffusion, (c) Molecule sieving, (d) surface diffusion, (e) gas-translational diffusion and (f) solid-state diffusion.

(a) Viscous Flow

When the pore size is sufficiently large ($\lambda_i \ll d_p$) and Knudsen number is less than 0.1 ($K_n < 0.1$), collisions between gas molecules are dominant, and the gas flow through the pores is governed by the viscous flow. The permeance, Q_v [$\text{mol m}^{-2} \text{s}^{-1} \text{Pa}^{-1}$] is given by following equation,

$$Q_v = \varepsilon \frac{d_p^2}{32\eta} \frac{(p_H + p_L)}{2RTL} \quad (1-12)$$

where ε is the porosity of the membrane [-], L is the thickness of the membrane [m] and η is the gas viscosity [Pa s], and the Q_v is directly proportional to the mean pressure of p_H (pressure of the gas feed side) and p_L (pressure of the gas permeate side).

(b) Knudsen Diffusion

When the d_p is smaller than the λ_i of the gas molecules, $K_n > 10$, and collisions occur between gas molecules and the pore wall, rather than between the gas molecules themselves. In this case, Knudsen diffusion occurs dominantly. Gas permeation by Knudsen diffusion occurs in the gaseous state exclusively because the interaction between diffusing gas molecules and pore wall is negligibly small. The Knudsen permeance of gas- i molecules, $Q_{K,i}$ [$\text{mol m}^{-2} \text{s}^{-1} \text{Pa}^{-1}$] is given by:

$$Q_{K,i} = \frac{\varepsilon}{3\tau L} d_p \left(\frac{8}{\pi M_i RT} \right)^{1/2} \quad (1-13)$$

where τ is the tortuosity [-] and M_i is the molecular weight of the gas- i molecule [g mol^{-1}]. In the ideal Knudsen diffusion, the permeance $Q_{k,i}$ is proportionate to the reciprocal of the square root of the permeation temperature ($T^{-0.5}$). In the case of permeation of mixed gas systems, each gas permeance is proportionate to the reciprocal of the square root of the molecular weight ($M^{-0.5}$) of the permeate gas molecule at the constant permeation temperature. Moreover, the theoretical permselectivity of gas A to another one B, $\alpha(A/B)$ can be calculated as the ratio of the inverse square root of the molecular weight of the two gases, M_A and M_B ,

$$\alpha(A/B) = \left(\frac{M_B}{M_A} \right)^{1/2} \quad (1-14)$$

For example, the permselectivity of H_2 to N_2 ($\alpha(\text{H}_2/\text{N}_2)$) in the ideal Knudsen diffusion is calculated 3.73, and $\alpha(\text{H}_2/\text{He})$ in that is calculated 1.41, that is, the permselectivity is extremely low under the Knudsen diffusion.

(c) Activated Diffusion (Molecule Sieving)

The molecular weight and kinetic diameter of typical gas molecules are shown in Table 1-1. When the pore size closes to the kinetic diameter of the target gas molecule

to separate, it is possible for the porous membranes to show the molecular sieve effect: by controlling the pore size to the ranges of sub-nanometer scale, the gas molecules with a kinetic diameter larger than the pore diameter are impermeable, while other gas molecules with the kinetic diameter smaller than the pore diameter permeate through those pores. As a result, high permselectivity can be achieved for the target gas molecule. The permeance Q_A can be expressed as Eq. (1-15) with the activation energy ΔE_A [J mol⁻¹] required for gas diffusion to overcome the energy barrier due to the size effect and with the pre-exponential factor Q_0 .

$$Q_A = Q_0 \exp\left(\frac{-\Delta E_A}{RT}\right) \quad (1-15)$$

From Eq. (1-15), Q_A increases consistently with the permeation temperature, and the ΔE_A can be estimated as an apparent activation energy by the Arrhenius plot: the permeance ($\log Q_A$) linearly decreases with the reciprocal of the permeation temperature ($1/T$), and the slope of the straight line gives the apparent activation energy. In general, the ΔE_A increases with the kinetic diameter of permeate gas molecules.

Table 1-1. Molecular weight and kinetic diameter of various gas molecules.

Gas	Molecular weight / g·mol ⁻¹	Kinetic diameter / nm
He	4.00	0.26
H ₂ O	18.02	0.265
H ₂	2.01	0.289
O ₂	32.00	0.346
CO ₂	44.01	0.33
N ₂	28.01	0.364

(d) Surface Diffusion

Surface diffusion occurs at low temperatures (lower than 150 °C [122]) when gas molecules cannot escape from potential field of the inner surface of pore wall due to the strong interaction between the inner surface and permeate gas molecules. Gas molecules are adsorbed on the inner surface and are transported by a concentration gradient of the adsorbed gas molecules in the gas permeate direction, z (dq/dz , which is proportion to the pressure difference as shown in Fig. 1-11). The resulting flux, J_S [mol m⁻² s⁻¹] is given by Eq. (1-13).

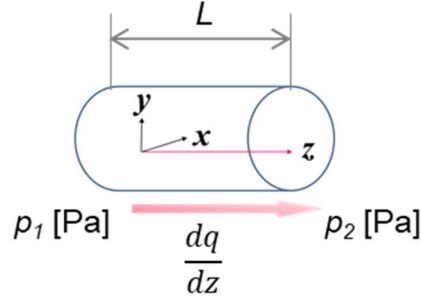


Fig. 1-11. Schematic image of the gas permeation direction through the pore.

$$J_S = D_S \rho_S (1 - \varepsilon) \frac{dq}{dp} \frac{dp}{dz} \quad (1-16)$$

where D_S is the surface diffusion coefficient [$\text{m}^2 \text{s}^{-1}$], ρ_S is the number density of molecules [m^{-3}] and q is the amount of adsorbed gas molecules [mol]. The surface diffusion coefficient D_S is given by Eq. (1-17) using a Fickian diffusion model. The amount of adsorbed gas molecules q is expressed by Eq. (1-18), assumed applying Henry law.

$$D_S = D_{S0} \exp\left(-\frac{\Delta E_D}{RT}\right) \quad (1-17)$$

$$q = ap = a_0 \exp\left(\frac{\Delta H_{ads}}{RT}\right) p \quad (1-18)$$

where D_{S0} is the pre-exponential factor [$\text{m}^2 \text{s}^{-1}$], ΔE_D is the energy barrier to jump to other adsorption sites [J mol^{-1}], a is the adsorption equilibrium constant [mol Pa^{-1}], a_0 is the pre-exponential factor [mol Pa^{-1}] and ΔH_{ads} is the heat of adsorption [J mol^{-1}]. The flux, J_S [$\text{mol m}^{-2} \text{s}^{-1}$] is given by introducing Eq. (1-17) and Eq. (1-18) into Eq. (1-16):

$$J_S = D_{S0} \rho_S (1 - \varepsilon) a_0 \frac{(p_H - p_L)}{L} \exp\left(-\frac{-\Delta H_{ads} + \Delta E_D}{RT}\right) \quad (1-19)$$

The permeance for the surface diffusion Q_S [$\text{mol m}^{-2} \text{s}^{-1} \text{Pa}^{-1}$] is given by introducing Eq. (1-19) into Eq. (1-9):

$$Q_S = Q_{S0} \exp\left(-\frac{\Delta E_S}{RT}\right), \quad \Delta E_S = -\Delta H_{ads} + \Delta E_D \quad (1-20)$$

where Q_{S0} is the frequency factor [$\text{mol m}^{-2} \text{s}^{-1} \text{Pa}^{-1}$]. In general, ΔE_S is a negative quantity and the overall exponent can be positive, because the gas adsorption became superior to

the moving to adsorption sites ($-\Delta H_{ads} < 0$, $\Delta E_D < |\Delta H_{ads}|$). Therefore, permeance Q_s decreases with increasing permeation temperature.

(e) Gas-translational Diffusion

The gas translational diffusion occurs when the interaction between diffusing gas molecules and the pore wall arises, with small pore size caused Knudsen diffusion. Therefore, this mechanism has been proposed as a combination of the Knudsen diffusion model and the surface diffusion model. So that, this is called an activated Knudsen diffusion model or gas-translational model (GT-model). By introducing a probability for diffusion through the pore channels, ρ [-] to the Knudsen diffusion model (Eq. (1-13)), Q_{KL} is given by Eq. (1-21).

$$Q_{KL} = \frac{\varepsilon d_p \rho}{\tau L} \left(\frac{8}{\pi M_i RT} \right)^{1/2} \quad (1-21)$$

The probability (ρ) is given by Eq. (1-22) with a frequency factor, ρ_g and the kinetic energy, $\Delta E_{act,i}$ to overcome the diffusion barrier [J mol⁻¹].

$$\rho = \rho_g \exp \left(-\frac{\Delta E_{act,i}}{RT} \right) \quad (1-22)$$

Therefore, the permeance can be expressed as the following Eq. (1-23) by the product of the Knudsen diffusion equation and the activation energy term to overcome the diffusion barrier of the pore wall.

$$Q_{KL} = \frac{\varepsilon d_e \rho_g}{\tau L} \left(\frac{8}{\pi M_i RT} \right)^{1/2} \exp \left(-\frac{\Delta E_{act,i}}{RT} \right) \quad (1-23)$$

$$\Delta E_{act,i} = -\Delta H_{ads} + \Delta E_d$$

where d_e is the diffusion length of permeating molecule [m] and ρ_g is the probability of the velocity in the right direction [m s⁻¹], ΔH_{ads} is the adsorption energy [J mol⁻¹] and ΔE_d is the activation energy for diffusion in the pore [J mol⁻¹].

In GT-model, the permeating molecule is treated as a sizeless simple mass point, so that the pore diameter, d_p is equal to the diffusion length of permeating gas molecules, d_e . However, in reality, the permeating molecule of gas- i is an object of finite size, d_i . In the modified GT-model (mGT-model) [122–125], the diffusion length of permeating molecule is supposed to be a circle with a diameter of $d_e = d_p - d_i$. The true cross-sectional area of pore, A_0 and the effective cross-sectional area of pore, A_e are given by Eq. (1-24).

$$A_0 = \frac{\pi}{4} d_p^2, \quad A_e = \frac{\pi}{4} d_e^2 = \frac{\pi}{4} (d_p - d_i)^2 \quad (1-24)$$

Therefore, the probability for diffusion (ρ) and the porosity (ε) are defined by A_0 , A_e and the membrane area A_m and the number of pore N_p .

$$\rho = \frac{1}{3} \frac{A_e}{A_0} \exp\left(-\frac{\Delta E_{act,i}}{RT}\right), \quad \varepsilon = \frac{A_0 N_p}{A_m} \quad (1-25)$$

Moreover, to discuss the gas permeation through a micropore, the potential field in the micropore $\Delta E_{att,i}$ and the gas molecule size d_i in the micropore with the diameter d_p are considered. The Knudsen permeance, Q_{cKL} of the gas state molecules, which are concentrated by the attractive nature of potential field of the pore wall, shown by Eq. (1-26) using Eq. (1-23) considered $\Delta E_{att,i}$, because the gas molecules can be transported in the gas-phase without a phase transition from gas to liquid. Introducing Eqs. (1-24) and (1-25) into Eq. (1-26), Q_{cKL} is given by Eq. (1-27).

$$Q_{cKL} = \frac{\varepsilon d_e \rho}{\tau L} \left(\frac{8}{\pi M_i RT}\right)^{1/2} \exp\left(-\frac{\Delta E_{att,i}}{RT}\right) \quad (1-26)$$

$$= \frac{k_0}{\sqrt{M_i RT}} (d_p - d_i)^3 \exp\left(-\frac{E_{act,i} + E_{att,i}}{RT}\right), \quad k_0 = \frac{N_p \sqrt{2\pi}}{6\tau A_m L} \quad (1-27)$$

Eq. (1-27) provides a more detailed description of the gas permeation model equation by considering not only the gas molecular size but also activation energy and adsorption energy [122].

In the range of the pore size applied the mGT-model, the gas permeation mechanisms through micropores can classify with a simple gas-permeation model equation considering the Knudsen diffusion and the Henry-type concentration enhancement of density in micropores [126]. In the conventional gas permeation model, the flux, J in a given direction for Knudsen diffusion is given by Eq. (1-28) according to Fick's first law of diffusion and ideal gas relation ($p = cRT$) for non-adsorptive gas.

$$J = -C_d \left(\frac{8RT}{\pi M}\right)^{1/2} \frac{dc}{dx} = C_d \left(\frac{8}{\pi MRT}\right)^{1/2} \frac{\Delta p}{L} \quad (1-28)$$

where Δp is the pressure drop across the membrane and C_d is the coefficient depended on the pore geometry.

In micropores, it is necessary to consider the effect of the potential field E_p to the permeating gas molecules as shown in Fig. 1-12 reported by Yoshioka *et al.* [126] In this gas-permeation model, gas molecules are assumed to permeate through straight micropores with cylindrical shape by their thermal movements. Furthermore, potential E_p , which exists in the radial and lateral directions homogeneously, is zero outside of the pore. And thermodynamic equilibrium condition between the outer-pore phase (gas

phase) and the inner-pore phase are satisfied both at pore entrance and exit. The pressure drop Δp_p between the pore entrance and the pore exit is given by Eq. (1-29).

$$\Delta p_p = \Delta p_a \exp\left(-\frac{E_p}{RT}\right) \quad (1-29)$$

where Δp_a is the apparent pressure drop across the membrane. Since the thermodynamic equilibrium condition between the outer- and the inner-pore phase are satisfied both at pore entrance and exit, the permeance Q_p is given by introducing Eq. (1-29) into Eq. (1-28):

$$Q_p = \frac{J_p}{\Delta p_a} = \frac{C_p}{\sqrt{MRT}} \exp\left(-\frac{E_p}{RT}\right) \quad (1-30)$$

The value of potential field, E_p depends on the pore size, d_e involved in the preexponential term, C_p which is a constant with membrane structures. Therefore, the gas permeation model from Knudsen diffusion to activated diffusion can be classified depending on the size of the micropores, considering an attractive or a repulsive potential field with negative or positive value respectively [126].

Figure 1-12 shows the dependence of the value of E_p on the pore size and the characteristics of the permeating gas molecule. For Type I with relatively large micropores, where E_p is nearly zero, gas molecules can permeate by normal Knudsen diffusion. In the case of Type II, the pore size becomes smaller than in the case of Type I, where E_p represents negative values, the attractive potential is effective for permeating gas molecules. The pressure drop of the inner-pore phase, Δp_p is larger than that of gas phase, Δp_a , because exponential term is larger than unity. In this case, permeation flux surpasses that by the Knudsen diffusion, therefore high gas-permeation is promoted through the surface diffusion. As for Type III with slightly smaller pore, E_p is nearly zero because the attractive potential field is nearly equal to the repulsive attractive one, as a result, the Knudsen-like mechanism is represented. For Type IV with much smaller pores than Type III, where E_p represents positive values, the repulsive potential from the pore wall works on permeating molecules and the pressure drop of the inner-pore phase, Δp_p becomes smaller than that of gas phase, Δp_a . In this case, Eq. (1-30) can be used to express gas-activated diffusion.

Note that the curve of E_p presented the broken line with a deeper bow at the smaller pore diameter shows that the permeating molecule is a little smaller and has greater interaction with the pore surface.

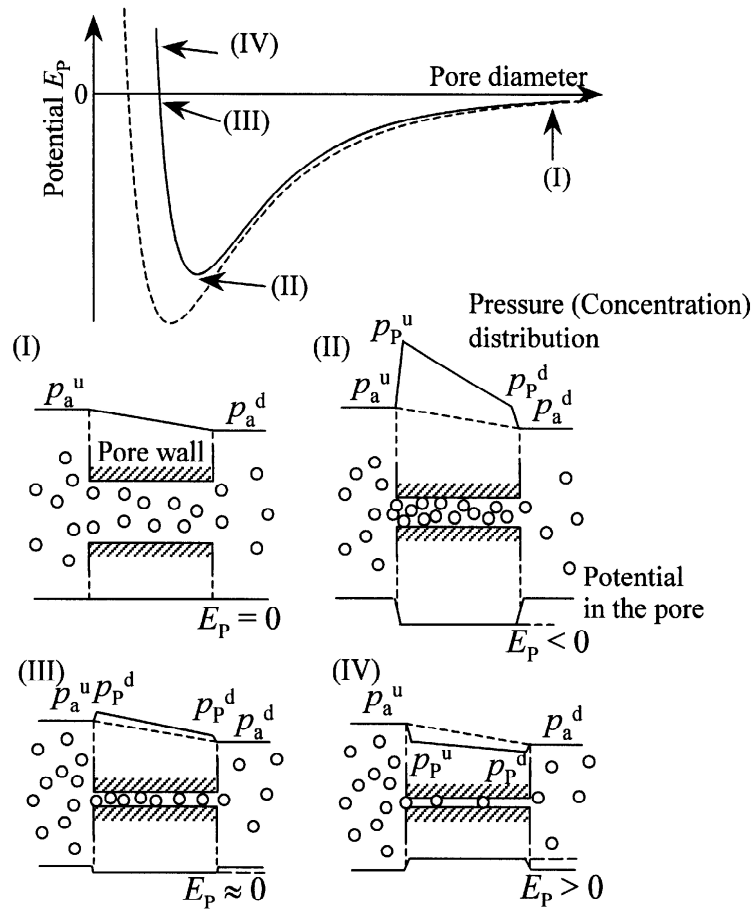


Fig. 1-12. Levelled potential in micropore as a function of pore size ($I > II > III > IV$) and gas pressure (concentration) distributions in the lateral direction, reported by Yoshioka *et al.* [126] (The potential within the pore was treated as uniform)

(f) Solid-state Diffusion

Solid-state diffusion occurs with further decrease in the pore size than Knudsen diffusion occurs, where the gas molecule interacts strongly with the membrane material behaving as a dense material. In this case, the solubility of the gas molecule is necessary to consider, so that the permeance of gas molecules through the membrane (Q_{ss} [$\text{mol m}^{-2} \text{s}^{-1} \text{Pa}^{-1}$]) is given by:

$$Q_{ss} = S_{ss} \times D_{ss} \quad (1-31)$$

where S_{ss} is the solubility [$\text{mol m}^{-3} \text{Pa}^{-1}$], and D_{ss} is the solid-state diffusivity [$\text{m}^2 \text{s}^{-1}$]. The S_{ss} is derived from the equilibrium between the solubility sites and the gaseous phase [127]. The D_{ss} is supposed that the process of gas atom movement between solubility sites

in the membrane is a random walk process with an equilibrium established between atoms in solubility sites and those moving between sites [128].

$$S_{ss} = \left(\frac{h^2}{2\pi mkT} \right)^{3/2} \times \frac{1}{kT} \frac{N_s}{N_A} \left(\frac{e^{-hv/2kT}}{1 - e^{-hv/kT}} \right)^3 e^{-\frac{\Delta E_{(0)}}{RT}} \quad (1-32)$$

$$D_{ss} = \frac{1}{6} \left(\frac{kT}{h} \right) d^2 \times \frac{\left(e^{hv/2kT} - e^{-hv/2kT} \right)^3}{\left(e^{hv^*/2kT} - e^{-hv^*/2kT} \right)^2} e^{-\frac{\Delta E_{ss}}{RT}} \quad (1-33)$$

Gas molecules, vibrating at solubility sites with a characteristic frequency, jump to an adjacent solubility site by surmounting a potential barrier. The permeance ($Q_{ss} = S_{ss} \times D_{ss}$) is given by following equation, considering the effect of rotation of polyatomic gas molecule:

$$Q_{ss} = \frac{d^2 h^2}{6L} \left(\frac{1}{2\pi mkT} \right)^{3/2} \left(\frac{\sigma h^2}{8\pi^2 I kT} \right)^\alpha \times \frac{(N_s/N_A)}{\left(e^{hv^*/2kT} - e^{-hv^*/2kT} \right)^2} e^{-\frac{\Delta E_{ss}}{RT}} \quad (1-34)$$

where d is jump distance [m], h is Planck's constant [$\text{m}^2 \text{kg s}^{-1}$], m is the mass [kg], ν^* is vibrational frequency of the gas molecules in the passageways between the sorption sites [s^{-1}], k is Boltzmann's constant [J K^{-1}], σ is the symmetry factor of the species ($\sigma=2$ for H_2), I is the moment of inertia [kg m^2], N_s is number of solubility sites per area [m^{-3}], ΔE_{ss} is activation energy for permeation [J mol^{-1}] and α is an exponent accounting for incomplete loss of rotation ($\alpha=0$ for monoatomic molecule, He, and $\alpha=0.2$ for polyatomic molecule, H_2).

1.5.1 Gas Permeances Measurement

The gas permeance measurement methods can be categorized into a non-equable pressure method and an equable pressure method, and the equable pressure method includes a manometric (variable-pressure) method and a volumetric (variable-volume) method. The volumetric method described below is suitable for this study because this method can determine not only the permeance of a single gas but also that of a mixed gas, under dry and wet condition.

Schematic diagram of apparatus for gas permeation measurements by the volumetric method is shown in Fig. 1-13. According to Fick's first law, the amount of gas molecular through the membrane is related to the gradient of concentration between the feed side and permeate side, which acts as the driving forces of the gas permeation. The gradient of concentration is proportion to the pressure difference between the gas feed side and the gas permeation side. In this method, the pressure difference maintains as predetermined constant value. At the steady state of the gas permeation through the membrane under the

given condition, the permeate molar flow rate of gas- i , V_i [mol s⁻¹] is measured to calculate a gas permeance, Q_i [mol m⁻² s⁻¹ Pa⁻¹] using Eq. (1-35).

$$Q_i = \frac{V_i}{A(p_H - p_L)} \quad (1-35)$$

The permeances of each gas included in the mixed gas can be calculated based on gas composition analysis by a gas chromatography and a flow rate measurement. To introduce a sufficient amount of the permeate gas with a small amount of flow rate into the gas chromatography, Ar gas flow is applied to sweep the permeate gas. In the mixed gas containing distinct gases, it is necessary that the pressure difference, $p_H - p_L$ of Eq. (1-35) is converted to an appropriate partial gas pressure difference for gas- i , $p_{H,i} - p_{L,i}$ where i denotes the target gas component to evaluate permeance. For example, in the mixed gas including H₂ and N₂, with Ar as the sweep gas, H₂ permeance is calculated using Eq. (1-36),

$$Q_{H_2} = \frac{V_{H_2}}{A(p_{H,H_2} - p_{L,H_2})} = \frac{V_{H_2+N_2} r_{L,H_2}}{A\left(r_{H,H_2} p_H - \frac{p_L V_{H_2+N_2} r_{L,H_2}}{V_{H_2+N_2+Ar}}\right)} \quad (1-36)$$

where V_{H_2} [mol s⁻¹] is the partial molar flow rate of H₂; $V_{H_2+N_2}$ [mol s⁻¹] is the permeate molar flow rate of H₂ and N₂; $V_{H_2+N_2+Ar}$ [mol s⁻¹] is the permeate molar flow rate with sweep gas; r_{H,H_2} [-] is molar ratio of H₂ in the feed mixed gas; r_{L,H_2} [-] is volume ratio of H₂ in the permeate mixed gas. The permeate molar flow rate, $V_{H_2+N_2}$ is calculated by $V_{H_2+N_2+Ar} - V_{Ar}$, each value is measured by the flowmeters. The r_{L,H_2} [-] is calculated based on the gas chromatographic determination. The partial molar flow rate of H₂, V_{H_2} [mol s⁻¹] is calculated by $V_{H_2} = V_{H_2+N_2} \times r_{L,H_2}$.

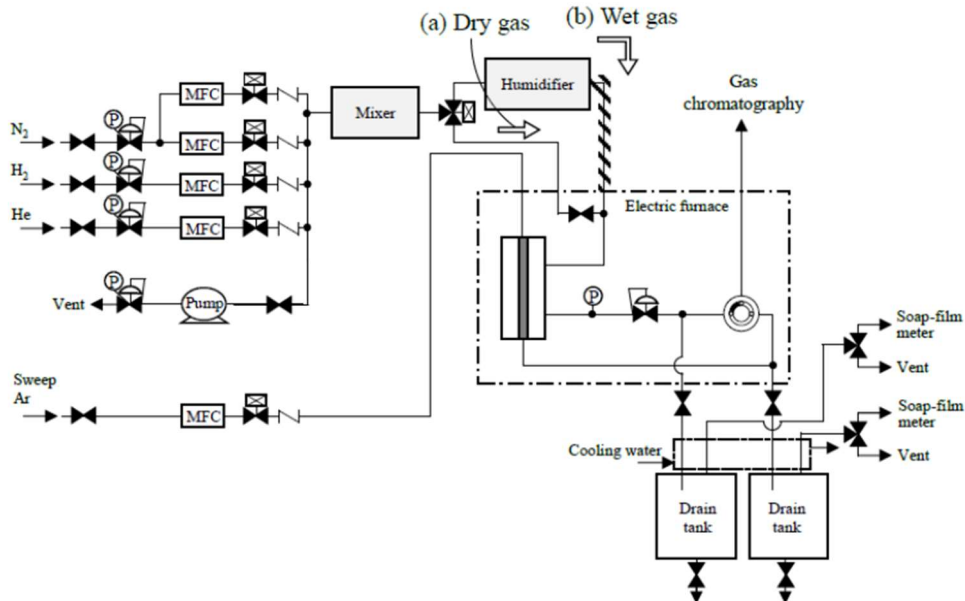


Fig. 1-13. Schematic of apparatus for gas permeation measurements by the volumetric method.

The measurement of the gas permeance under humid condition is performed under predetermined water partial vapor pressures (p/p_0). The volume of permeate water vapor is analyzed by a gas chromatography for polar gas analysis.

1.6 Object of Present Study

As described previously in this chapter, in the hope of significant reduction of CO₂ emissions, many research and development are conducting to aim at creating a hydrogen society. Mentioned in the previous sub-section 1.2.2, the PEC water-splitting has received much attention as an environmental-friendly hydrogen production method, because of its high potential to replace the current hydrogen production by the steam reforming of hydrocarbons. Due to its co-production of gaseous H₂ and O₂, H₂ gas must be immediately separated from the syngas under the high-humidity conditions at low temperatures around 50 °C.

However, under such given condition, H₂-permselectivity of membranes have been studied little. Moreover, due to safety reasons, membrane performance in terms of hydrogen selectivity is generally evaluated using N₂ as a reference molecule and evaluated as H₂/N₂ selectivity, $\alpha(\text{H}_2/\text{N}_2)$ which is given by the ratio of $Q_{\text{H}_2}/Q_{\text{N}_2}$. Figure 1-14 shows data of membrane performance in terms of H₂-permeance and $\alpha(\text{H}_2/\text{N}_2)$ evaluated for same membranes under dry condition at $T \leq 50$ °C.

It should be noted that the kinetic diameters of H₂, O₂ and N₂ are 0.289, 0.346 and 0.364 nm, respectively [38], and thus for practical application, evaluation of $\alpha(\text{H}_2/\text{O}_2)$ should be required after the brief evaluation using N₂ as a reference gas molecule. As shown in Fig. 1-14, SiO₂-based organic-inorganic hybrid membranes showed high H₂ permeances of 1.79×10^{-6} and 7.66×10^{-7} mol m⁻² s⁻¹ Pa⁻¹, while the $\alpha(\text{H}_2/\text{N}_2)$ remained at 12 and 20 [129]. On the other hand, zeolite/CMS (carbon molecular sieve) composite membranes showed a high $\alpha(\text{H}_2/\text{N}_2)$ of 61 to 100.2, however the H₂ permeance at 30 °C was 10^{-9} - 10^{-8} mol m⁻² s⁻¹ Pa⁻¹ order [130,131]. Accordingly, these membranes show typical trade-off relationship between H₂ permeance and $\alpha(\text{H}_2/\text{N}_2)$ at $T \leq 50$ °C under dry condition.

On the other hand, there are some reports on the excellent membrane performance of novel membranes evaluated at $T \leq 50$ °C under dry condition: an ultrathin (9 nm thickness) graphene oxide membrane formed on an anodic oxidized alumina support exhibited a H₂ permeance of approximately 1×10^{-7} mol m⁻² s⁻¹ Pa⁻¹ with $\alpha(\text{H}_2/\text{N}_2)$ of 900 at 20 °C [132,133]. A zeolite imidazolate framework (ZIF) nanosheet membrane (#08) also showed H₂ permeance of 2.04×10^{-7} mol m⁻² s⁻¹ Pa⁻¹ with high $\alpha(\text{H}_2/\text{N}_2)$ of 66.6 at 30 °C [134,135]. These results suggest that novel design concept for membrane material can be expected as one of key technologies to surpass the trade-off relationship of the previously reported membrane samples shown in Fig. 1-14.

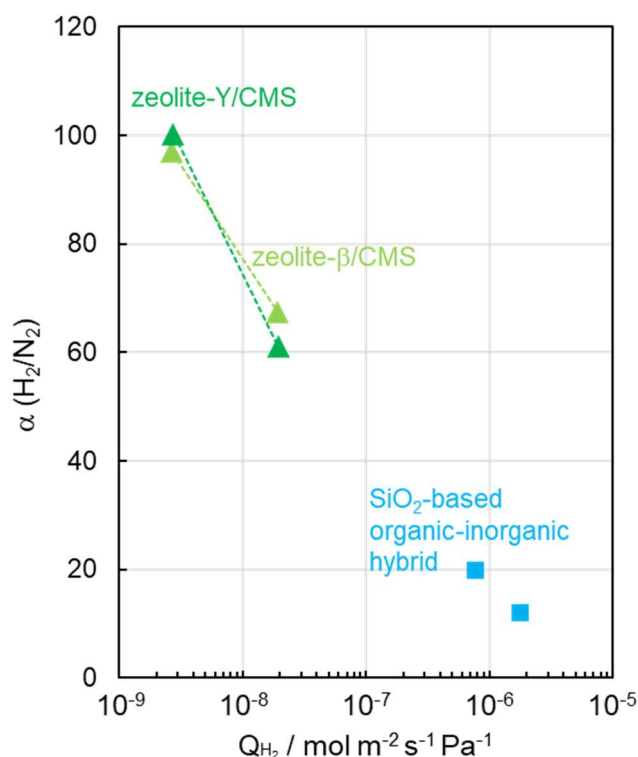


Fig.1-14. H₂-permeance and H₂/N₂ selectivity ($\alpha(H_2/N_2)$) of porous membranes evaluated at $T \leq 50$ °C under dry condition.

In addition to the high performance as H₂-selective membranes, hydrostability in terms of stable gas permeation is a critical technical issue of porous ceramic membranes for application to novel solar hydrogen production systems. With regard to the hydrostability of the microporous amorphous SiO₂, amorphous SiO₂-based organic-inorganic hybrids which were chemically modified with alkoxy groups were previously suggested [59]. However, as shown in Fig. 1-14, introduction of the organic alkyl substitutes to amorphous silica network leads to degradation of H₂ selectivity.

To overcome the technical issues of the SiO₂-based system, PCS-derived ternary Si-C-H organic-inorganic hybrid system can be expected to show excellent hydrophobic properties: PCSs are composed of Si-C backbones partly substituted with methyl (CH₃) group, *i.e.* smallest hydrophobic alkyl group, and thus expected to show stable H₂ gas permeation with relatively high H₂-selectivity under such a high humidity operation condition of the solar hydrogen production systems.

In addition, as mentioned in the previous section 1.4.1.1, as well as the active molecular sieving microporous top layer, stable gas permeation through the mesoporous γ -Al₂O₃ intermediate layer beneath the microporous layer, typically composed of amorphous SiO₂ is the technical issue. However, almost no one has studied on the gas permeation properties of the supported mesoporous γ -Al₂O₃ intermediate layer itself under the given condition of high humidity at $T \leq 50$ °C. As mentioned in the section

1.4.2.1, the PDCs route can offer opportunities for surface modification as well as thin film (membrane) synthesis through conventional dip or spin coating of the starting polymer precursor solution or melt impregnation of liquid state polymer precursor to porous substrates. Accordingly, PCSs are expected to be useful as a surface modifier for mesoporous γ -Al₂O₃ to improve hydrophobicity in terms of stable gas permeations under the solar hydrogen system operation condition.

Based on these materials background and research strategies, this study was conducted aiming to develop novel hydrogen permselective SiCH-based organic-inorganic hybrid membranes for the solar hydrogen production systems which are operated under high humidity condition at $T \leq 50$ °C.

1.7 Outline of This Thesis

Chapter 1 describes a brief introduction of hydrogen as a clean energy carrier, and novel CO₂ emission-free hydrogen production system via the PEC water-splitting and its technical requirement of H₂ selective membrane for the purification of hydrogen from the syngas including O₂ under the highly humid condition at low-temperatures (≤ 50 °C). Then, based on the materials background and research strategies shown in the sections 1.4.1 to 1.6, develop novel hydrogen permselective SiCH-based organic-inorganic hybrid membranes has been performed:

In Chapter 2, characterization of excellent hydrophobicity of PCS-derived SiCH-based organic-inorganic hybrids was performed by measuring water vapor adsorption-desorption isotherms at room temperature. Then, under the simulated high humidity condition for the system operation of solar hydrogen production at 50 °C, the intrinsic gas permeation property, *i.e.* degradation of H₂ permeations through the mesoporous γ -Al₂O₃ intermediate layer was assessed by evaluating the gas permeations. It was experimentally confirmed that the degradation of the gas permeations through the mesoporous γ -Al₂O₃ layer occurred due to the blockage of the gas permeable mesopore channels by adsorbed water molecules as shown in Fig. 1-15(a). Then, the hydrostability in terms of stable gas permeations through the supported mesoporous γ -Al₂O₃ membrane was significantly improved (Fig. 1-16(a)) by surface modification with the PCS-derived SiCH-based organic-inorganic hybrid (Fig. 1-15(b)).

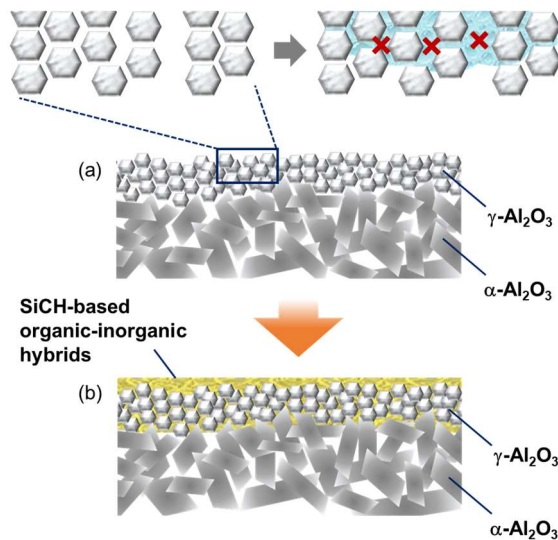


Fig.1-15. Schematic diagram showing (a) degradation in gas permeation property under the high humidity condition at $T \leq 50$ °C due to the condensation within the gas permeable mesopore channels of $\gamma\text{-Al}_2\text{O}_3$ membrane formed on a macroporous $\alpha\text{-Al}_2\text{O}_3$ support, and (b) complete surface modification with highly hydrophobic PCS-derived Si-C-H organic-inorganic hybrid to achieve stable gas permeations.

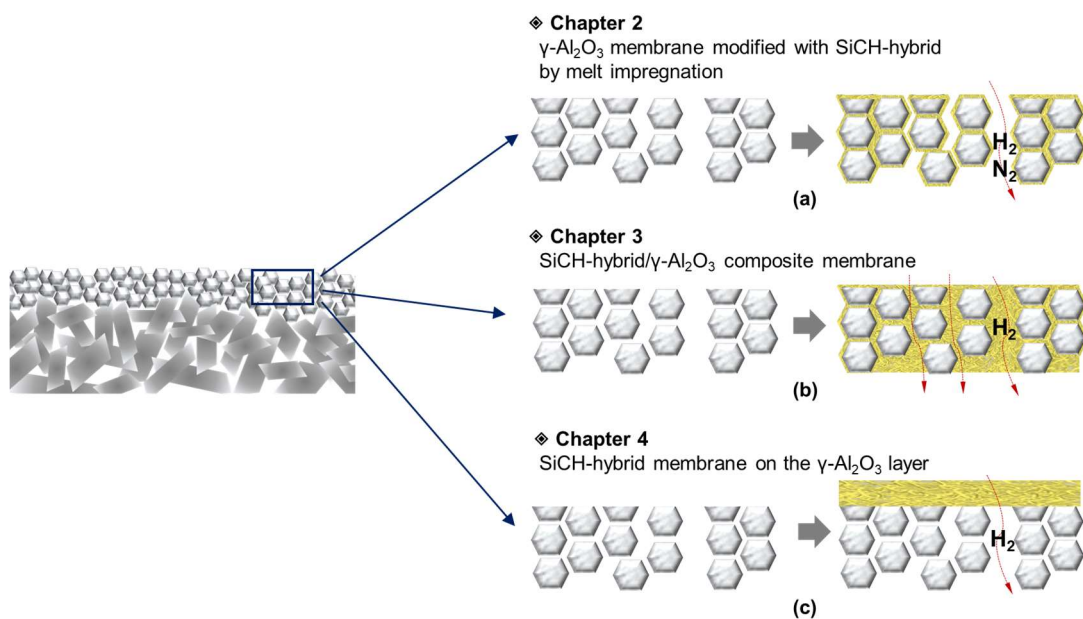


Fig.1-16. Schematic diagram of the membranes with SiCH-organic-inorganic hybrids to harmonize hydrostability in terms of stable gas permeation and H_2 -selectivity of the porous membranes having highly hydrophilic mesoporous $\gamma\text{-Al}_2\text{O}_3$ layer as an intermediate layer component in their multi-layer construction in Chapters 2, 3 and 4.

In Chapter 3, SiCH-based organic-inorganic hybrid/ γ -Al₂O₃ composite membranes were attempted to fabricate using another PCS derivative, allyl-hydro-polycarbosilane (AHPCS) which can be chemically and/or thermally cross-linked via hydrosilylation between the Si-H and C=C in allyl groups. This synthesis strategy was expected to be essential to achieve H₂-permselectivity of the composite membranes. Fig. 1-16(b)). AHPCS was converted to highly cross-linked ternary SiCH-based organic-inorganic hybrids with enhanced thermal stability and hydrophobicity by heat treatment at temperatures as low as 300–500 °C in argon (Ar). Highly hydrophobic property of the AHPCS-derived SiCH-based organic-inorganic hybrids was characterized by the water vapor adsorption–desorption isotherm measurement at 25 °C. Relations between the polymer/hybrid conversion temperature, hydrophobicity, and H₂ affinity of the AHPCS-derived SiCH-hybrids were studied to functionalize the composite membranes as H₂-selective under saturated water vapor partial pressure at 50 °C. In addition, the composite membrane was further modified by the PCS-derived SiCH-hybrid and the gas permeance through that composite membrane was also measured under the saturated water vapor partial pressure at 50 °C under a H₂-N₂ (2:1) mixed gas flow as a simulated syngas produced by the PEC reaction.

In Chapter 4, a layered-composite membrane composed of the SiCH hybrid top-layer supported on a mesoporous γ -Al₂O₃ layer and that was attempted to fabricate to clarify the intrinsic gas permeation properties of the SiCH organic-inorganic hybrid itself (Fig. 1-16(c)). Then, gas permeation properties of the supported SiCH-hybrid membrane were characterized by measuring single gas permeances of He, H₂ and N₂ under dry and wet condition. Possible mechanisms for gas permeations through the supported SiCH-hybrid membranes were discussed based on the gas permeation behaviors with unique H₂/He selectivity under wet condition, improved H₂/N₂ selectivity under the high-humidity conditions at 50 °C. Moreover, excellent H₂-selectivity under saturated humidity at 50 °C of the supported SiCH-based membrane was demonstrated by using a H₂-N₂ (2:1) mixed feed gas as a simulated syngas produced by the PEC reaction.

References

- [1] Annual report concerning energy (Energy white paper 2020), Agency for Natural Resources and Energy (Ministry of Economy, Trade and Industry), 2020.
- [2] J.M. Ogden, R.H. Williams, E.D. Larson, Societal lifecycle costs of cars with alternative fuels/engines, *Energy Policy* 32 (2004) 7–27.
- [3] Basic Hydrogen Strategy, Ministerial Council on Renewable Energy, Hydrogen and Related Issues held its second meeting, 2017.
- [4] Hydrogen energy white paper by NEDO, New Energy and Industrial Technology Development Organization, 2015.
- [5] 2019 – Understanding the current energy situation in Japan (Part 1), Agency Nat. Resour. Energy. (2019).
https://www.enecho.meti.go.jp/en/category/special/article/energyissue2019_01.html (accessed October 10, 2020).

- [6] S. Yagyu, H. Matsui, T. Matsuda, H. Yasumoto, Studies of explosive characteristics of hydrogen (1st report), Minist. Labour, Res. Inst. Ind. Saf. (1969) RIIS-RR-18-1.
- [7] A.K. Prabhu, S.T. Oyama, Highly hydrogen selective ceramic membranes: Application to the transformation of greenhouse gases, *J. Memb. Sci.* 176 (2000) 233–248.
- [8] S. Kurungot, T. Yamaguchi, S. Nakao, Rh/ γ -Al₂O₃ catalytic layer integrated with sol – gel synthesized microporous silica membrane for compact membrane reactor applications, *Catal. Letters.* 86 (2003) 273–278.
- [9] K. Akamatsu, T. Murakami, T. Sugawara, R. Kikuchi, S. Nakao, Stable equilibrium shift of methane steam reforming in membrane reactors with hydrogen-selective silica membranes, *AIChE J.* 57 (2011) 1882–1888.
- [10] K. Maeda, K. Domen, New non-oxide photocatalysts designed for overall water splitting under visible light, *J. Phys. Chem. C.* 111 (2007) 7851–7861.
- [11] Q. Wang, T. Hisatomi, Q. Jia, H. Tokudome, M. Zhong, C. Wang, Z. Pan, T. Takata, M. Nakabayashi, N. Shibata, Y. Li, I.D. Sharp, A. Kudo, T. Yamada, K. Domen, Scalable water splitting on particulate photocatalyst sheets with a solar-to-hydrogen energy conversion efficiency exceeding 1%, *Nat. Mater.* 15 (2016) 611–615.
- [12] Y. Goto, T. Hisatomi, Q. Wang, T. Higashi, K. Ishikiriyama, T. Maeda, Y. Sakata, S. Okunaka, H. Tokudome, M. Katayama, S. Akiyama, H. Nishiyama, Y. Inoue, T. Takewaki, T. Setoyama, T. Minegishi, T. Takata, T. Yamada, K. Domen, A Particulate Photocatalyst Water-Splitting Panel for Large-Scale Solar Hydrogen Generation, *Joule* 2 (2018) 509–520.
- [13] T. Yamada, K. Domen, Development of Sunlight Driven Water Splitting Devices towards Future Artificial Photosynthetic Industry, *ChemEngineering* 2 (2018) 36.
- [14] Development of Basic Chemical Processes for Carbon Dioxide as Raw Material, *New Energy Ind. Technol. Dev. Organ.* (2014).
https://www.nedo.go.jp/activities/EV_00296.html (accessed August 2, 2020).
- [15] Development of a Particulate Photocatalyst Sheet to Achieve Artificial Photosynthesis, *New Energy Ind. Technol. Dev. Organ.* (2016).
https://www.nedo.go.jp/news/press/AA5_100533.html (accessed October 6, 2020).
- [16] A. Fujishima, K. Honda, Electrochemical Photolysis of Water at a Semiconductor Electrode, *Nature* 238 (1972) 37–38.
- [17] The world of titanium dioxide Market dialogue and breakthrough, Univ. Tokyo.
https://www.u-tokyo.ac.jp/focus/en/features/f_00057.html.
- [18] T. Takata, J. Jiang, Y. Sakata, M. Nakabayashi, N. Shibata, V. Nandal, K. Seki, T. Hisatomi, K. Domen, Photocatalytic water splitting with a quantum efficiency of almost unity, *Nature* 581 (2020) 411–414.
- [19] K. Tanaka, Y. Sakata, Present and Future Prospects of Hydrogen Production Process Constructed by the Combination of Photocatalytic H₂O Splitting and Membrane Separation Process, *Membrane* 36 (2011) 113–121.
- [20] N.W. Ockwig, T.M. Nenoff, Membranes for hydrogen separation, *Chem. Rev.* 107 (2007) 4078–4110.
- [21] S. Yun, S. Ted Oyama, Correlations in palladium membranes for hydrogen separation: A review, *J. Memb. Sci.* 375 (2011) 28–45.

- [22] S. Liguori, A. Iulianelli, F. Dalena, P. Pinacci, F. Drago, M. Broglia, Y. Huang, A. Basile, Performance and long-term stability of Pd/PSS and Pd/Al₂O₃ membranes for hydrogen separation, *Membranes* 4 (2014) 143–162.
- [23] F. Gallucci, J.A. Medrano, E. Fernandez, J. Melendez, M. Van Sint Annaland, D.A. Pacheco-Tanaka, Advances on high temperature Pd-based membranes and membrane reactors for hydrogen purification and production, *J. Membr. Sci. Res.* 3 (2017) 142–156.
- [24] D. Alique, D. Martinez-Diaz, R. Sanz, J.A. Calles, Review of supported pd-based membranes preparation by electroless plating for ultra-pure hydrogen production, *Membranes* 8 (2018) 5.
- [25] S.T. Oyama, S.M. Stagg-Williams, *Inorganic, Polymeric and Composite Membranes: Structure, Function and Other Correlations*, Elsevier, Amsterdam, 2011.
- [26] Y. Mise, S.J. Ahn, A. Takagaki, R. Kikuchi, S.T. Oyama, Fabrication and evaluation of trimethylmethoxysilane (TMMOS)-derived membranes for gas separation, *Membranes* 9 (2019) 123.
- [27] H. Kato, S.-T.B. Lundin, S.-J. Ahn, A. Takagaki, R. Kikuchi, S.T. Oyama, Gas Separation Silica Membranes Prepared by Chemical Vapor Deposition of Methyl-Substituted Silanes, *Membranes* 9 (2019) 144.
- [28] S. Ted Oyama, H. Aono, A. Takagaki, T. Sugawara, R. Kikuchi, Synthesis of silica membranes by chemical vapor deposition using a dimethyldimethoxysilane precursor, *Membranes* 10 (2020) 50.
- [29] S. Sato, K. Nagai, Polymer Membranes with Hydrogen-Selective and Hydrogen-Rejective Properties, *Membrane* 30 (2005) 20–28.
- [30] L.A. Neves, J.G. Crespo, I.M. Coelho, Gas permeation studies in supported ionic liquid membranes, *J. Memb. Sci.* 357 (2010) 160–170.
- [31] Q. Gan, D. Rooney, M. Xue, G. Thompson, Y. Zou, An experimental study of gas transport and separation properties of ionic liquids supported on nanofiltration membranes, *J. Memb. Sci.* 280 (2006) 948–956.
- [32] B. Castro-Dominguez, P. Leelachaikul, A. Takagaki, T. Sugawara, R. Kikuchi, S.T. Oyama, Supported perfluorotributylamine liquid membrane for H₂/O₂ separation, *J. Memb. Sci.* 448 (2013) 262–269.
- [33] P. Leelachaikul, B. Castro-Dominguez, A. Takagaki, T. Sugawara, R. Kikuchi, S.T. Oyama, Perfluorooctanol-based liquid membranes for H₂/O₂ separation, *Sep. Purif. Technol.* 122 (2014) 431–439.
- [34] T. Yamaguchi, A. Takagaki, T. Sugawara, R. Kikuchi, S.T. Oyama, Supported fluorocarbon liquid membranes for hydrogen/oxygen separation, *J. Memb. Sci.* 520 (2016) 272–280.
- [35] M.F. San Román, E. Bringas, R. Ibañez, I. Ortiz, Liquid membrane technology: Fundamentals and review of its applications, *J. Chem. Technol. Biotechnol.* 85 (2010) 2–10.
- [36] T. Schober, Applications of oxidic high-temperature proton conductors, *Solid State Ionics* 162–163 (2003) 277–281.
- [37] A. Unemoto, N. Kitamura, K. Amezawa, T. Kawada, Hydrogen Permeation Properties in (Ce,Sr) PO₄, *Electrochem. Solid-State Lett.* 12 (2009) 43–47.
- [38] D.W. Breck, *Zeolite Molecular Sieves: Structure, Chemistry, and Use*, John Wiley & Sons, New York, 1974.

- [39] Y. Iwamoto, Precursors-Derived Ceramic Membranes for High-Temperature Separation of Hydrogen, *J. Ceram. Soc. Japan* 115 (2007) 947–954.
- [40] R.M. de Vos, H. Verweij, High-Selectivity, High-Flux Silica Membranes for Gas Separation, *Science* 279 (1998) 1710–1711.
- [41] Y. Iwamoto, K. Sato, T. Kato, T. Inada, Y. Kubo, A hydrogen-permselective amorphous silica membrane derived from polysilazane, *J. Eur. Ceram. Soc.* 25 (2005) 257–264.
- [42] T. Nagano, S. Fujisaki, K. Sato, K. Hataya, Y. Iwamoto, M. Nomura, S.-I. Nakao, Relationship between the mesoporous intermediate layer structure and the gas permeation property of an amorphous silica membrane synthesized by counter diffusion chemical vapor deposition, *J. Am. Ceram. Soc.* 91 (2008) 71–76.
- [43] A. Burneau, J. Lepage, G. Maurice, Porous silica-water interactions. I. Structural and dimensional changes induced by water adsorption, *J. Non. Cryst. Solids* 217 (1997) 1–10.
- [44] T. Tsuru, T. Hino, T. Yoshioka, M. Asaeda, Permporometry characterization of microporous ceramic membranes, *J. Memb. Sci.* 186 (2001) 257–265.
- [45] A.B. Kołtuniewicz, E. Drioli, *Membranes in clean technologies: theory and practice*, WILEY-VCH Verlag GmbH & Co. KGaA, Weinheim, 2008.
- [46] S.A. Younssi, M. Breida, B. Achiou, in: M. Eyavz, E. Yüksel (Eds.), Chapter 11. Alumina Membranes for Desalination and Water Treatment in *Desalin. Water Treat.*, IntertechOpen, 2018.
- [47] T. Van Gestel, C. Vandecasteele, A. Buekenhoudt, C. Dotremont, J. Luyten, R. Leysen, B. Van der Bruggen, G. Maes, Alumina and titania multilayer membranes for nanofiltration: Preparation, characterization and chemical stability, *J. Memb. Sci.* 207 (2002) 73–89.
- [48] X. Yang, L. Ding, M. Wolf, F. Velterop, H.J.M. Bouwmeester, S. Smart, J.C. Diniz da Costa, A. Liubinas, J.-D. Li, J. Zhang, M. Duke, Pervaporation of ammonia solution with γ -alumina supported organosilica membranes, *Sep. Purif. Technol.* 168 (2016) 141–151.
- [49] K. Miyajima, T. Eda, B.N. Nair, S. Honda, Y. Iwamoto, Hydrothermal stability of hydrogen permselective amorphous silica membrane synthesized by counter diffusion chemical vapor deposition method, *J. Ceram. Soc. Japan* 121 (2013) 992–998.
- [50] T. Nagano, K. Sato, Degradation mechanism of an H₂-permselective amorphous silica membrane, *J. Mater. Sci.* 49 (2014) 4115–4120.
- [51] M.H. Zahir, K. Sato, Y. Iwamoto, Development of hydrothermally stable sol-gel derived La₂O₃-doped Ga₂O₃-Al₂O₃ composite mesoporous membrane, *J. Memb. Sci.* 247 (2005) 95–101.
- [52] M.H. Zahir, K. Sato, H. Mori, Y. Iwamoto, M. Nomura, S.I. Nakao, Preparation and properties of hydrothermally stable γ -alumina-based composite mesoporous membranes, *J. Am. Ceram. Soc.* 89 (2006) 2874–2880.
- [53] M.H. Zahir, Y.H. Ikuhara, S. Fujisaki, K. Sato, T. Nagano, Y. Iwamoto, Preparation and characterization of mesoporous ceria-zirconia-alumina nanocomposite with high hydrothermal stability, *J. Mater. Res.* 22 (2007) 3201–3209.

- [54] M.H. Zahir, S. Fujisaki, K. Sato, T. Nagano, Y. Iwamoto, Mesoporous CeO₂-ZrO₂- γ -Al₂O₃ nanocomposite membranes exhibiting remarkable hydrothermal stability, *Desalin. Water Treat.* 2 (2009) 229–236.
- [55] T. Nagano, K. Sato, T. Saitoh, S. Takahashi, Hydrothermal stability of mesoporous Ni-doped γ -Al₂O₃, *J. Ceram. Soc. Japan* 117 (2009) 832–835.
- [56] Z.D. Hendren, J. Brant, M.R. Wiesner, Surface modification of nanostructured ceramic membranes for direct contact membrane distillation, *J. Memb. Sci.* 331 (2009) 1–10.
- [57] A. Larbot, L. Gazagnes, S. Krajewski, M. Bukowska, W. Kujawski, Water desalination using ceramic membrane distillation, *Desalination* 168 (2004) 367–372.
- [58] S. Koonaphapdeelert, K. Li, Preparation and characterization of hydrophobic ceramic hollow fibre membrane, *J. Memb. Sci.* 291 (2007) 70–76.
- [59] M.N. Mohd Sokri, T. Onishi, Y. Daiko, S. Honda, Y. Iwamoto, Hydrophobicity of amorphous silica-based inorganic-organic hybrid materials derived from perhydropolysilazane chemically modified with alcohols, *Microporous Mesoporous Mater.* 215 (2015) 183–190.
- [60] J. Mendret, M. Hatat-Fraile, M. Rivallin, S. Brosillon, Hydrophilic composite membranes for simultaneous separation and photocatalytic degradation of organic pollutants, *Sep. Purif. Technol.* 111 (2013) 9–19.
- [61] N.F. Ishak, N.A. Hashim, M.H.D. Othman, P. Monash, F.M. Zuki, Recent progress in the hydrophilic modification of alumina membranes for protein separation and purification, *Ceram. Int.* 43 (2017) 915–925.
- [62] B. Van Der Bruggen, C. Vandecasteele, T. Van Gestel, W. Doyen, R. Leysen, A Review of Pressure-Driven Membrane Processes in Wastewater Treatment and Drinking Water Production, *Environ. Prog.* 22 (2003) 46–56.
- [63] S. Krajewski, W. Kujawski, M. Bukowska, C. Picard, A. Larbot, Application of fluoroalkylsilanes (FAS) grafted ceramic membranes in membrane distillation process of NaCl solutions, *J. Memb. Sci.* 281 (2006) 253–259.
- [64] F. Gabino, M.-P. Belleville, L. Preziosi-Belloy, M. Dornier, J. Sanchez, Evaluation of the cleaning of a new hydrophobic membrane for osmotic evaporation, *Sep. Purif. Technol.* 55 (2007) 191–197.
- [65] S. Cerneaux, I. Strużyńska, W.M. Kujawski, M. Persin, A. Larbot, Comparison of various membrane distillation methods for desalination using hydrophobic ceramic membranes, *J. Memb. Sci.* 337 (2009) 55–60.
- [66] C.C. Wei, K. Li, Preparation and characterization of a robust and hydrophobic ceramic membrane via an improved surface grafting technique, *Ind. Eng. Chem. Res.* 48 (2009) 3446–3452.
- [67] J. Gu, C. Ren, X. Zong, C. Chen, L. Winnubst, Preparation of alumina membranes comprising a thin separation layer and a support with straight open pores for water desalination, *Ceram. Int.* 42 (2016) 12427–12434.
- [68] T. Liu, L. Lei, J. Gu, Y. Wang, L. Winnubst, C. Chen, C. Ye, F. Chen, Enhanced water desalination performance through hierarchically-structured ceramic membranes, *J. Eur. Ceram. Soc.* 37 (2017) 2431–2438.
- [69] J. Kujawa, S. Cerneaux, W. Kujawski, Investigation of the stability of metal oxide powders and ceramic membranes grafted by perfluoroalkylsilanes, *Colloids Surfaces A Physicochem. Eng. Asp.* 443 (2014) 109–117.

- [70] J. Kujawa, S. Cerneaux, W. Kujawski, M. Bryjak, J. Kujawski, How to Functionalize Ceramics by Perfluoroalkylsilanes for Membrane Separation Process? Properties and Application of Hydrophobized Ceramic Membranes, *ACS Appl. Mater. Interfaces* 8 (2016) 7564–7577.
- [71] U. Díaz, A. Corma, Organic-Inorganic Hybrid Materials: Multi-Functional Solids for Multi-Step Reaction Processes, *Chem. - A Eur. J.* 24 (2018) 3944–3958.
- [72] S.H. Mir, L.A. Nagahara, T. Thundat, P. Mokarian-Tabari, H. Furukawa, A. Khosla, Review—Organic-Inorganic Hybrid Functional Materials: An Integrated Platform for Applied Technologies, *J. Electrochem. Soc.* 165 (2018) B3137–B3156.
- [73] P. Judeinstein, C. Sanchez, Hybrid organic–inorganic materials: a land of multidisciplinary, *J. Mater. Chem.* 6 (1996) 511–525.
- [74] P. Colombo, G. Mera, R. Riedel, G.D. Sorarù, Polymer-derived ceramics: 40 Years of research and innovation in advanced ceramics, *J. Am. Ceram. Soc.* 93 (2010) 1805–1837.
- [75] J. Bill, F. Aldinger, Precursor-derived Covalent Ceramics, *Adv. Mater.* 7 (1995) 775–787.
- [76] R. Riedel, Advanced Ceramics from Inorganic Polymers, in: R.J. Brook (Ed.), *Mater. Sci. Technol.*, Wiley-VCH, Weinheim, 1996: pp. 1–50.
- [77] E. Kroke, Y.L. Li, C. Konetschny, E. Lecomte, C. Fasel, R. Riedel, Silazane derived ceramics and related materials, *Mater. Sci. Eng. R Reports* 26 (2000) 97–199.
- [78] T. Prenzel, M. Wilhelm, K. Rezwan, Pyrolyzed polysiloxane membranes with tailorable hydrophobicity, porosity and high specific surface area, *Microporous Mesoporous Mater.* 169 (2013) 160–167.
- [79] T. Prenzel, K. Döge, R.P.O. Motta, M. Wilhelm, K. Rezwan, Controlled hierarchical porosity of hybrid ceramics by leaching water soluble templates and pyrolysis, *J. Eur. Ceram. Soc.* 34 (2014) 1501–1509.
- [80] G.S. dos Reis, C.H. Sampaio, E.C. Lima, M. Wilhelm, Preparation of novel adsorbents based on combinations of polysiloxanes and sewage sludge to remove pharmaceuticals from aqueous solutions, *Colloids Surfaces A Physicochem. Eng. Asp.* 497 (2016) 304–315.
- [81] F. Schlüter, M. Wilhelm, K. Rezwan, Surfactant assisted syntheses of monolithic hybrid ceramics with hierarchical porosity, *J. Eur. Ceram. Soc.* 35 (2015) 2963–2972.
- [82] D. Schumacher, M. Wilhelm, K. Rezwan, Modified solution based freeze casting process of polysiloxanes to adjust pore morphology and surface functions of SiOC monoliths, *Mater. Des.* 160 (2018) 1295–1304.
- [83] R.K. Nishihora, M.G.N. Quadri, D. Hotza, K. Rezwan, M. Wilhelm, Tape casting of polysiloxane-derived ceramic with controlled porosity and surface properties, *J. Eur. Ceram. Soc.* 38 (2018) 4899–4905.
- [84] T. Prenzel, T.L.M. Guedes, F. Schlüter, M. Wilhelm, K. Rezwan, Tailoring surfaces of hybrid ceramics for gas adsorption - From alkanes to CO₂, *Sep. Purif. Technol.* 129 (2014) 80–89.
- [85] T. Prenzel, M. Wilhelm, K. Rezwan, Tailoring amine functionalized hybrid ceramics to control CO₂ adsorption, *Chem. Eng. J.* 235 (2014) 198–206.

- [86] F. Schlüter, J. Meyer, M. Wilhelm, K. Rezwani, Hierarchical emulsion based hybrid ceramics synthesized with different siloxane precursor and with embedded nickel nanoparticles, *Colloids Surfaces A Physicochem. Eng. Asp.* 492 (2016) 160–169.
- [87] M. Schubert, M. Wilhelm, S. Bragulla, C. Sun, S. Neumann, T.M. Gesing, P. Pfeifer, K. Rezwani, M. Bäumer, The Influence of the Pyrolysis Temperature on the Material Properties of Cobalt and Nickel Containing Precursor Derived Ceramics and their Catalytic Use for CO₂ Methanation and Fischer–Tropsch Synthesis, *Catal. Letters.* 147 (2017) 472–482.
- [88] H.P. Macedo, R.L.B.A. Medeiros, J. Ilsemann, D.M.A. Melo, K. Rezwani, M. Wilhelm, Nickel-containing hybrid ceramics derived from polysiloxanes with hierarchical porosity for CO₂ methanation, *Microporous Mesoporous Mater.* 278 (2019) 156–166.
- [89] C. Leger, H.L. De Lira, R. Paterson, Preparation and properties of surface modified ceramic membranes. Part II. Gas and liquid permeabilities of 5 nm alumina membranes modified by a monolayer of bound polydimethylsiloxane (PDMS) silicone oil, *J. Memb. Sci.* 120 (1996) 135–146.
- [90] A.F.M. Pinheiro, D. Hoogendoorn, A. Nijmeijer, L. Winnubst, Development of a PDMS-grafted alumina membrane and its evaluation as solvent resistant nanofiltration membrane, *J. Memb. Sci.* 463 (2014) 24–32.
- [91] G. Huang, Q. Yang, Q. Xu, S.-H. Yu, H.-L. Jiang, Polydimethylsiloxane Coating for a Palladium/MOF Composite: Highly Improved Catalytic Performance by Surface Hydrophobization, *Angew. Chemie Int. Ed.* 128 (2016) 7505–7509.
- [92] J. Gu, J. Wang, Y. Li, X. Xu, C. Chen, L. Winnubst, Engineering durable hydrophobic surfaces on porous alumina ceramics using in-situ formed inorganic-organic hybrid nanoparticles, *J. Eur. Ceram. Soc.* 37 (2017) 4843–4848.
- [93] G. Camino, S.M. Lomakin, M. Lazzari, Polydimethylsiloxane thermal degradation. Part 1. Kinetic aspects., *Polymer* 42 (2001) 2395–2402.
- [94] G. Camino, S.M. Lomakin, M. Lazard, Thermal polydimethylsiloxane degradation. Part 2. The degradation mechanisms, *Polymer* 43 (2002) 2011–2015.
- [95] Nippon Carbon Co, LTD, Technical Information, Polycarbosilanes “Nipusi®”, 19, May, 1995, (1995).
- [96] S. Yajima, J. Hayashi, M. Omori, Continuous silicon carbide fiber of high tensile strength, *Chem. Lett.* 4 (1975) 931–934.
- [97] S. Yajima, K. Okamura, J. Hayashi, M. Omori, Synthesis of Continuous SiC Fibers with High Tensile Strength, *J. Am. Ceram. Soc.* 59 (1976) 324–327.
- [98] D. Hotza, M. Di Luccio, M. Wilhelm, Y. Iwamoto, S. Bernard, J.C. Diniz da Costa, Silicon carbide filters and porous membranes: A review of processing, properties, performance and application, *J. Memb. Sci.* 610 (2020) 118193.
- [99] L.-L. Lee, D.-S. Tsai, A Hydrogen-Permeable Silicon Oxycarbide Membrane Derived from Polydimethylsilane, *J. Am. Ceram. Soc.* 82 (1999) 2796–2800.
- [100] A.B. Shelekhin, E.J. Grosgogeat, S.T. Hwang, Gas separation properties of a new polymer/inorganic composite membrane, *J. Memb. Sci.* 66 (1992) 129–141.
- [101] K. Kusakabe, Z. Yan Li, H. Maeda, S. Morooka, Preparation of supported composite membrane by pyrolysis of polycarbosilane for gas separation at high temperature, *J. Memb. Sci.* 103 (1995) 175–180.

- [102] Z. Li, K. Kusakabe, S. Morooka, Preparation of thermostable amorphous Si-C-O membrane and its application to gas separation at elevated temperature, *J. Memb. Sci.* 118 (1996) 159–168.
- [103] Z. Li, K. Kusakabe, S. Morooka, Pore Structure and Permeance of Amorphous Si-C-O Membranes with High Durability at Elevated Temperature, *Sep. Sci. Technol.* 32 (1997) 1233–1254.
- [104] H. Suda, H. Yamauchi, Y. Uchimarui, I. Fujiwara, K. Haraya, Preparation and gas permeation properties of silicon carbide-based inorganic membranes for hydrogen separation, *Desalination* 193 (2006) 252–255.
- [105] T. Nagano, K. Sato, T. Saitoh, Y. Iwamoto, Gas permeation properties of amorphous SiC membranes synthesized from polycarbosilane without oxygen-curing process, *J. Ceram. Soc. Japan* 114 (2006) 533–538.
- [106] A. Takeyama, M. Sugimoto, M. Yoshikawa, Gas permeation property of SiC membrane using curing of polymer precursor film by electron beam irradiation in helium atmosphere, *Mater. Trans.* 52 (2011) 1276–1280.
- [107] B. Elyassi, W. Deng, M. Sahimi, T.T. Tsotsis, On the use of porous and nonporous fillers in the fabrication of silicon carbide membranes, *Ind. Eng. Chem. Res.* 52 (2013) 10269–10275.
- [108] S. Dabir, W. Deng, M. Sahimi, T. Tsotsis, Fabrication of silicon carbide membranes on highly permeable supports, *J. Memb. Sci.* 537 (2017) 239–247.
- [119] R.J. Ciora, B. Fayyaz, P.K.T. Liu, V. Suwanmethanon, R. Mallada, M. Sahimi, T.T. Tsotsis, Preparation and reactive applications of nanoporous silicon carbide membranes, *Chem. Eng. Sci.* 59 (2004) 4957–4965.
- [110] F. Sandra, A. Ballester, V.L. Nguyen, M.N. Tsampas, P. Vernoux, C. Balan, Y. Iwamoto, U.B. Demirci, P. Miele, S. Bernard, Silicon carbide-based membranes with high soot particle filtration efficiency, durability and catalytic activity for CO/HC oxidation and soot combustion, *J. Memb. Sci.* 501 (2016) 79–92.
- [111] Q. Wang, M. Yokoji, H. Nagasawa, L. Yu, M. Kanezashi, T. Tsuru, Microstructure evolution and enhanced permeation of SiC membranes derived from allylhydridopolycarbosilane, *J. Memb. Sci.* (2020) 118392.
- [112] L.V. Interrante, Q. Shen, Polycarbosilanes, in: R.G. Jones, W. Ando, J. Chojnowski (Eds.), *Silicon-Containing Polym.*, Kluwer Academic Publisher, Netherlands, 2000: pp. 247–321.
- [113] K. Matsumoto, Polycarbosilanes, in: H.F. Mark (Ed.), *Encycl. Polym. Sci. Technol.*, 3rd ed., John Wiley & Sons, New York, 2003: pp. 426–438.
- [114] K. Matsumoto, T. Endo, Synthesis and ring-opening polymerization of functional silacyclobutane derivatives and their application to lithium ion batteries, *Macromol. Symp.* 349 (2015) 21–28.
- [115] S. Yajima, T. Shishido, K. Okamura, SiC Bodies Sintered with Three-Dimensional Cross-Linked Polycarbosilane, *AMER. CERAM. SOC. BULL.* 56 (1977) 1060–1063.
- [116] Y.-W. Kim, J.-G. Lee, Effect of polycarbosilane addition on mechanical properties of hot-pressed silicon carbide, *J. Mater. Sci.* 27 (1992) 4746–4750.
- [117] P. Czubarow, D. Seyferth, Application of poly(methylsilane) and Nicalon® polycarbosilane precursors as binders for metal/ceramic powders in preparation of functionally graded materials, *J. Mater. Sci.* 32 (1997) 2121–2130.

- [118] Y. Sawai, Y. Iwamoto, S. Okuzaki, Y. Yasutomi, K. Kikuta, S. Hirano, Synthesis of Silicon Carbide Ceramics Using Chemically Modified Polycarbosilanes as a Compaction Binder, *J. Am. Ceram. Soc.* 82 (1999) 2121–2125.
- [119] G.B. Arfken, D.F. Griffing, D.C. Kelly, J. Priest, Kinetic Theory, in: *Univ. Phys.*, 1984: pp. 460–473.
- [120] S.N. Ahmed, Interaction of radiation with matter, in: *Phys. Eng. Radiat. Detect.*, Elsevier, 2015: pp. 65–155.
- [121] S.T. Oyama, M. Yamada, T. Sugawara, A. Takagaki, R. Kikuchi, Review on mechanisms of gas permeation through inorganic membranes, *J. Japan Pet. Inst.* 54 (2011) 298–309.
- [122] T. Yoshioka, M. Kanezashi, T. Tsuru, Micropore size estimation on gas separation membranes: A study in experimental and molecular dynamics, *AIChE J.* 59 (2013) 2179–2194.
- [123] A.B. Shelekhin, A.G. Dixon, Y.H. Ma, Theory of gas diffusion and permeation in inorganic molecular-sieve membranes, *AIChE J.* 41 (1995) 58–67.
- [124] R.S.A. de Lange, K. Keizer, A.J. Burggraaf, Analysis and theory of gas transport in microporous sol-gel derived ceramic membranes, *J. Memb. Sci.* 104 (1995) 81–100.
- [125] A.J. Burggraaf, Single gas permeation of thin zeolite (MFI) membranes: Theory and analysis of experimental observations, *J. Memb. Sci.* 155 (1999) 45–65.
- [126] T. Yoshioka, E. Nakanishi, T. Tsuru, M. Asaeda, Experimental studies of gas permeation through microporous silica membranes, *AIChE J.* 47 (2001) 2052–2063.
- [127] P.L. Studt, J.F. Shackelford, R.M. Fulrath, Solubility of Gases in Glass—A Monatomic Model, *J. Appl. Phys.* 41 (1970) 2777–2780.
- [128] J.S. Masaryk, R.M. Fulrath, Diffusivity of helium in fused silica, *J. Chem. Phys.* 59 (1973) 1198–1202.
- [129] X. Ren, T. Tsuru, Organosilica-based membranes in gas and liquid-phase separation, *Membranes* 9 (2019) 107.
- [130] L. Li, C. Wang, N. Wang, Y. Cao, T. Wang, The preparation and gas separation properties of zeolite/carbon hybrid membranes, *J. Mater. Sci.* 50 (2015) 2561–2570.
- [131] L. Li, R. Xu, C. Song, B. Zhang, Q. Liu, T. Wang, A review on the progress in nanoparticle/C hybrid CMS membranes for gas separation, *Membranes* 8 (2018) 134.
- [132] H. Li, Z. Song, X. Zhang, Y. Huang, S. Li, Y. Mao, H.J. Ploehn, Y. Bao, M. Yu, Ultrathin, molecular-sieving graphene oxide membranes for selective hydrogen separation, *Science* 342 (2013) 95–98.
- [133] L. Huang, H. Lin, Engineering sub-nanometer channels in two-dimensional materials for membrane gas separation, *Membranes* 8 (2018) 100.
- [134] Y. Li, L. Lin, M. Tu, P. Nian, A.J. Howarth, O.K. Farha, J. Qiu, X. Zhang, Growth of ZnO self-converted 2D nanosheet zeolitic imidazolate framework membranes by an ammonia-assisted strategy, *Nano Res.* 11 (2018) 1850–1860.
- [135] M. Fang, C. Montoro, M. Semsarilar, Metal and covalent organic frameworks for membrane applications, *Membranes* 10 (2020) 107.

Chapter 2

A hydrostable mesoporous γ -Al₂O₃ membrane modified with SiCH-based organic-inorganic hybrid derived from polycarbosilane

2.1 Introduction

As described in the previous section 1.2.2, the solar driven water splitting photocatalyst reaction can generate hydrogen (H₂) and oxygen (O₂) by an oxidation-reduction reaction of water with particulate semiconductors [1,2]. After water photo-splitting, speedy separation of H₂ from solar product gas needs at low temperatures (≤ 50 °C) under high humidity condition [3]. Microporous amorphous SiO₂ membranes, represented to the active separation layer, have been studied for application to high-temperature separation of H₂ [4–8]. However, under such high humidity conditions at $T \leq 50$ °C, serious performance degradation occurs by blockage of H₂-permeable micropore channels through the surface silanol-induced water monomolecular layer adsorption [9] followed by capillary condensation of water molecules [3,10]. Moreover, microporous amorphous SiO₂ membranes have been fabricated in the form of multilayered composite membranes, consisting of an active SiO₂ top layer, a mesoporous γ -Al₂O₃ intermediate layer, and a macroporous α -Al₂O₃ support. Therefore, in addition to microporous amorphous SiO₂, hydrostability in terms of the stable gas permeations under the humid condition of the mesoporous γ -Al₂O₃ intermediate layer is an additional issue as discussed in the previous section 1.4.1.1. However, almost no one has studied on the permeance degradation of the mesoporous γ -Al₂O₃ intermediate layer itself under the given condition.

In this chapter, gas permeation properties under the wet condition of the supported mesoporous γ -Al₂O₃ membrane layer was characterized, then its hydrostability in terms of stable gas permeation was tried to be improved by surface modification with hydrophobic compound, PCS-derived SiCH-based organic-inorganic hybrid. This chapter describes (1) Characterization of hydrophobicity of PCS-derived SiCH-based organic-inorganic hybrids by measuring water vapor adsorption-desorption isotherms at room temperature, (2) Effect of water vapor partial pressure on gas permeation behaviors at 50 °C of hydrophilic mesoporous γ -Al₂O₃ membrane formed on a macroporous α -Al₂O₃ support, and (3) Improvement in the hydrostability in terms of stable gas permeations through the mesoporous γ -Al₂O₃ membrane by modification with PCS-derived hydrophobic SiCH-based organic-inorganic hybrid.

2.2 Experimental Procedures

2.2.1 Fabrication of mesoporous γ -Al₂O₃ membrane on a macroporous α -Al₂O₃ support

In this study, a commercially available α -Al₂O₃ tubular support (6 mm outer diameter, 4 mm inner diameter and 60 mm length, Noritake Co., Ltd., Aichi, Japan) was used. The α -Al₂O₃ support had a two-layer structure: a core with a mean pore diameter of 700 nm, and a fine outer surface layer (rim) with a mean pore diameter of 150 nm. The total porosity of the support was 40 %.

The γ -Al₂O₃ precursor solution was prepared according to the published procedure [11–14]: A mixture of 12.7 g of aluminum-tri-sec-butoxide (Al(OCH(CH₃)CH₂CH₃)₃, ATSB, 97 % purity, Sigma-Aldrich Co. LLC, STL, USA) and 7.70 ml of isopropyl alcohol (HOCH(CH₃)₂, IPA, purity \geq 99.7 %, Kishida Chemical Co., Ltd., Osaka, Japan) was stirred under argon (Ar) atmosphere at room temperature for 1 h. Then, the mixture was added to distilled water (90 ml) maintained at 90 °C. After the addition completed, the mixture was stirred for at least 1 h to evaporate off the IPA and butanol formed by the hydrolysis of ATSB. After the evaporation completed, the reaction mixture was diluted with 90 ml of additional distilled water and cooled down to room temperature, then peptized with 1M HNO₃ (60.0-61.0 %, Kishida Chemical Co., Ltd., Osaka, Japan) at a pH of about 3. During the synthesis, the sol was stirred vigorously. The peptized mixture was stirred at 60 °C for about 15 h so as to adjust the total volume to 60 ml, yielding a boehmite (γ -AlOOH) sol (0.83 mol L⁻¹) with a clear whitish-blue appearance.

Flow chart for preparation of γ -AlOOH coating solution is shown in Fig. 2-1. The as-prepared γ -AlOOH sol was mixed with 3.5 wt% solution of polyvinyl alcohol (PVA, degree of saponification ca. 86.5-89 mol%, Kanto Chemical Co., Inc., Tokyo, Japan) at the volume ratio of 2 to 3 followed by stirring at room temperature for 1 h to afford γ -AlOOH coating solution.

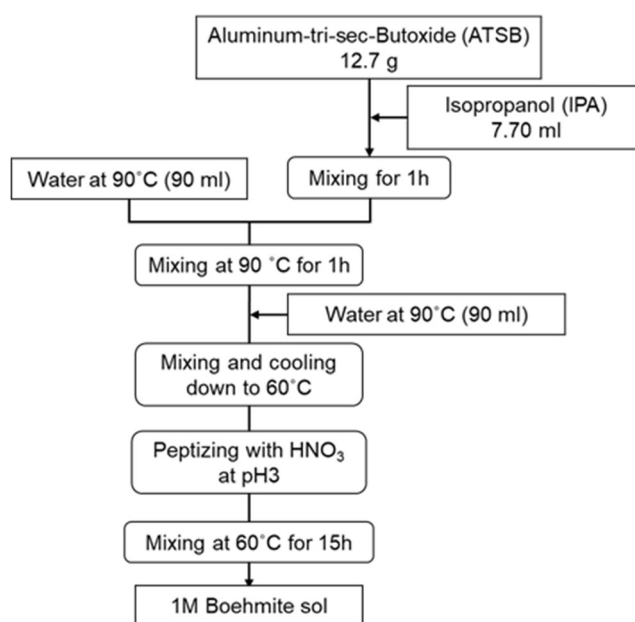


Fig. 2-1. Flow chart for preparation of γ -Al₂O₃ precursor solution.

Prior to coating step, the α -Al₂O₃ tubular support was cleaned by rinsing in ethanol (C₂H₅OH, purity \geq 99.5 %, Kishida Chemical Co., Ltd., Osaka, Japan) at 78 °C for 30 min and dried at 120 °C for 50 min. Each end of the tubular support was plugged, and the support was dipped into the γ -AlOOH coating solution at a constant speed of 10 mm s⁻¹, remained in the solution for 10 sec, then pulled out at a constant speed of 1 mm s⁻¹. The dip-coated support was dried at 60 °C for 1 h in air before calcination at 600 °C for 3 h at a heating/cooling rate of 100 °C h⁻¹. This dipping-drying-calcining sequence was repeated once to form a defect-free mesoporous γ -Al₂O₃ membrane on the outer surface of a macroporous α -Al₂O₃ tubular support.

2.2.2 Surface modification of γ -Al₂O₃ membrane with SiCH-based organic-inorganic hybrid

In this study, a commercially available PCS (Type L, Nippon Carbon Co., Ltd., Tokyo, Japan) was used. Table 2-1 listed melting point (m.p.) and chemical composition of PCS Type L (hereafter PCS(L)) in comparison with those of PCS Type UH (hereafter PCS(UH)) which was previously used for developing a compaction binder [15]. All the data was provided by the supplier [16]. Chemical composition of PCS(L) was similar to that of PCS(UH). However, PCS(L) had a low m.p. of 80 °C, while PCS(UH) had no distinct m.p. (partly melt \sim 350 °C). In the previous study, PCS(UH) was found as useful to fabricate a He and H₂-selective amorphous SiC thin layer on a mesoporous γ -Al₂O₃ formed as an intermediate thin layer on the outer surface of a porous α -Al₂O₃ support [17]. The polymer/amorphous SiC conversion was performed by cross-linking at 300 °C followed by heat treatment at 800 °C in Ar. Based on this previous result, it was obvious that, even under such a high temperature condition, PCS(UH) had no chance to modify the supported mesoporous γ -Al₂O₃ thin layer sufficiently deep inside to achieve hydrophobicity for the stable gas permeations under the humid condition. On the other hand, as shown in Fig. 2-2, Gel Permeation Chromatography (GPC) analysis at our laboratory revealed that the mean molecular weight (Mw) and number average molecular weight (Mn) of PCS(L) were 1704 and 951, respectively, which were much smaller than those of PCS(UH) (Mw and Mn were 7194 and 2806, respectively). These features of PCS(L) offered a melt impregnation method for modifying entire mesoporous γ -Al₂O₃ membrane, and thus PCS(L) was selected in the present study.

Table 2-1. Properties of commercial PCSs. [16]

Type	m.p./ °C	Chemical composition/ wt%				
		Si	C	H	O	N
L	80	49	38	9.0	1.5	2.0
UH	-	50	40	8.2	1.4	1.7

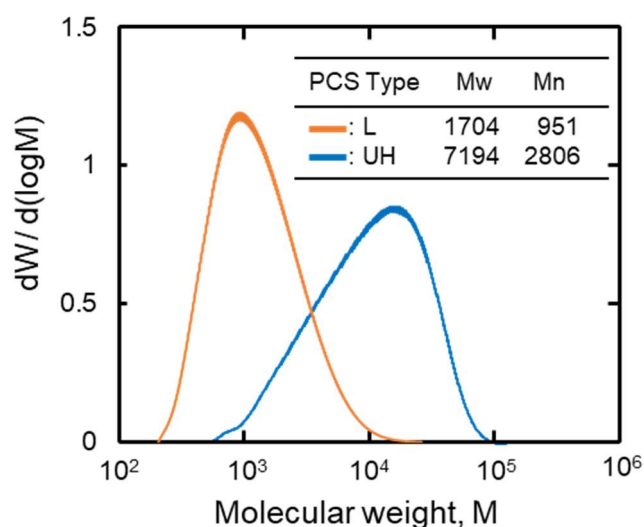


Fig. 2-2. Molecular-weight distribution of as-received PCS Type L and Type UH.

As-received PCS(L) was dissolved in dry xylene (super dehydrated grade, 99.5 % purity, Wako Pure Chemical Co., Ltd., Osaka, Japan) to afford 1 wt% PCS(L)/ dry xylene solution. A mesoporous γ -Al₂O₃ membrane on a tubular support was cleaned and dried under the same manner as mentioned above, and each end of the membrane sample was plugged. Then, the modification was performed by following two steps: (1) Dip coating of the PCS(L)/ dry xylene solution under the same manner as mentioned for the γ -AlOOH coating and (2) Heat treatment at 120 °C for 1h in air for conducting melt impregnation to afford PCS(L)-derived organic-inorganic SiCH-based hybrid-modified γ -Al₂O₃ membrane placed on a microporous α -Al₂O₃ support. Flow chart of modification for mesoporous γ -Al₂O₃ intermediate layer with PCS(L)-derived SiCH-based organic-inorganic hybrid is shown in Fig. 2-3.

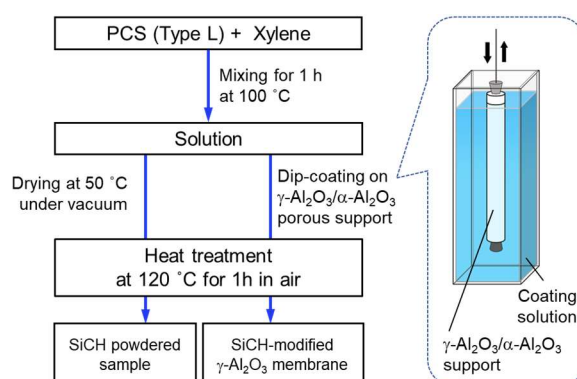


Fig. 2-3. Flow chart of modification for mesoporous γ -Al₂O₃ intermediate layer with PCS(L)-derived SiCH-based organic-inorganic hybrid and preparation of that powder.

2.2.3 Characterizations

The Mw and Mn of as-received PCSs were determined at 40 °C by GPC (Model ShodexGPC-104 equipped with two tandem columns (Model Shodex LF-404) and a refractive index detector (Model Shodex RI-74S), Showa Denko K.K., Tokyo, Japan). The columns were calibrated against polystyrene standards. Tetrahydrofuran (THF) was used as the eluent at a flow rate of 1.0 mL min⁻¹.

Fourier transform (FT)-IR spectrum was recorded on as-received PCSs by the potassium bromide (KBr) disk method (Model FT/IR-4200IF, JASCO Corp., Tokyo, Japan).

Hydrophobicity of the mesoporous γ -Al₂O₃ and PCS(L)-derived organic-inorganic SiCH-based hybrid were characterized by measuring the water vapor adsorption-desorption isotherms of the powdered samples at 25 °C (Model BELSORP-aqua 3, MicrotracBEL Corp., Osaka, Japan). The powdered sample of γ -Al₂O₃ was prepared by drying the γ -AlOOH coating solution at 120 °C followed by calcination at 600 °C for 3 h under the same manner for the synthesis of supported membrane samples. The polymer-derived SiCH powder sample was also prepared by solvent removal from the PCS(L) coating solution at 50 °C under vacuum followed by heat treatment at 120 °C for 1h in air, as shown in Fig. 2-3. In this study, the measurement was also performed on the following reference samples: another organic-inorganic SiCH hybrid derived from PCS(UH) [15] synthesized under the same manner as PCS(L)-derived SiCH, perhydropolysilazane (PHPS)-derived amorphous SiO₂ and n-decyl (n-C₁₀H₂₁) group-functionalized amorphous SiO₂ which were synthesized according to the reference [18].

Cross-sectional structure of the supported γ -Al₂O₃ membrane was observed by a scanning electron microscope (SEM, Model JSM-6360LV, JEOL Ltd., Tokyo, Japan). Distribution of the SiCH within the modified mesoporous γ -Al₂O₃ membrane after the PCS(L)-coating and subsequent 120 °C-heat treatment was investigated by conventional element mapping for the PCS(L)-derived Si using an energy dispersive X-ray spectrometer mounted on a SEM (Model JSM-6010LA, JEOL Ltd., Tokyo, Japan).

The pore size distribution was measured for the supported mesoporous γ -Al₂O₃ membrane using the capillary condensation technique (Model Porometer nano, MicrotracBEL Corp., Osaka, Japan) after sample drying at 120 °C for 200 min under He flow.

Single gas permeances through a sample membrane were measured by the volumetric method at constant pressure. The gas permeances at 25, 50 and 80 °C were measured in order of a kinetic diameter for He (0.26 nm), H₂ (0.289 nm) and N₂ (0.364 nm). At 50 °C, the single gas permeances were also measured at water partial vapor pressures (p/p₀ (H₂O)) ranging from 0.1 to 1.

The setup for the measurements is illustrated in Fig. 1-13 in Chapter 1. The outer side of the tubular sample membrane was filled with a single gas (high purity, >99.99%) under an atmospheric pressure. The inner side of the tubular sample membrane was evacuated

using a vacuum pump so as to maintain the pressure difference between the inner side (gas permeation side) and the outer side (gas feed side) as 100 kPa. After terminating evacuation, the permeate molar flow rate (V) was measured by a flow meter (High Precision Film Flow Meter, Model SF-1U·2U, HORIBA, Ltd., Kyoto, Japan) to calculate a gas permeance (Q) using Eq. (1-35) in Chapter 1. In this experiment, $p_H - p_L$ in Eq. (1-35), had a constant value of 100 kPa.

2.3 Results and Discussion

2.3.1 Hydrophilic/Hydrophobic characteristics

The hydrophilic/hydrophobic characteristics of mesoporous γ - Al_2O_3 and PCS(L)-derived organic-inorganic SiCH hybrid samples were assessed by the water vapor adsorption-desorption isotherm measured at 25 °C (Fig. 2-4).

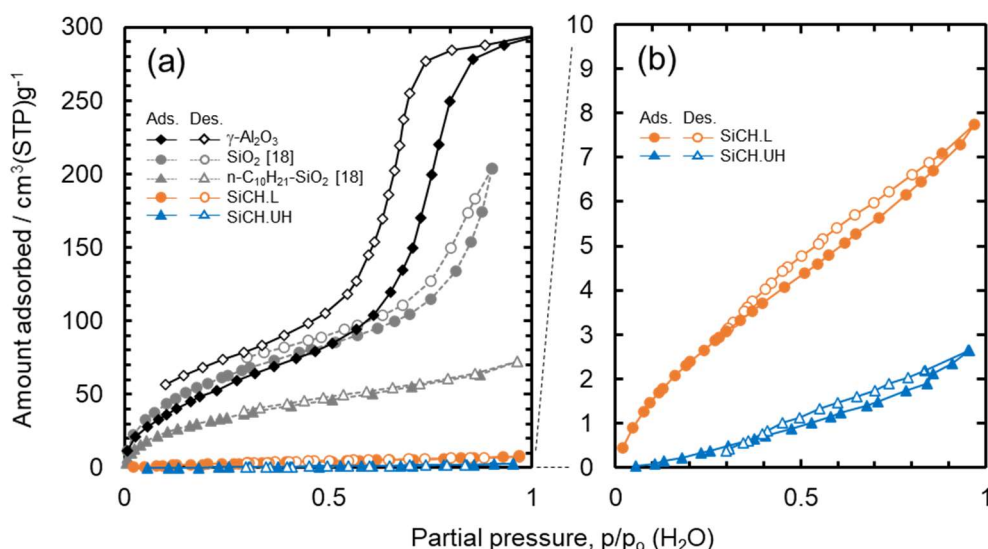


Fig. 2-4. Water vapor sorption-desorption isotherms for powdered samples of (a) mesoporous γ - Al_2O_3 and PCS-derived SiCH-based organic-inorganic hybrid samples synthesized in this study, reference samples of PHPS-derived amorphous SiO_2 [18] and n- $\text{C}_{10}\text{H}_{21}$ -functionalized amorphous SiO_2 [18], (b) magnified view of (a) at lower water vapor adsorptions below 8 cm³(STP)g⁻¹.

The γ - Al_2O_3 generated type IV isotherms with type H3 hysteresis loops, normally observed for the solids having cylindrical and spherical pores [19,20]. This result was inconsistent with previous reports [21–23]: Mesoporous γ - Al_2O_3 composed of plate-shaped crystallites forms slit-shaped pores, which was detected as type H2 hysteresis loops by the adsorption-desorption isotherms measurement using an inert prove gas molecule such as N_2 . The detection of type H3 hysteresis loops in the present study could

be due to the highly condensable water vapor used as a probe gas molecule or formation of γ -Al₂O₃ particle aggregates [24].

The maximum water vapor adsorption ($V_a(\text{H}_2\text{O})$) of γ -Al₂O₃ reached 297 cm³(STP)g⁻¹ (Fig. 2-4(a)), showing higher hydrophilic character compared with amorphous SiO₂ [18]. On the other hand, the PCS(L)-derived SiCH hybrid (labeled as SiCH.L) presented an excellent hydrophobic character. The $V_a(\text{H}_2\text{O})$ of SiCH.L was below 8 cm³(STP)g⁻¹ (Fig. 2-4(b)). This value was much lower than that previously achieved for the n-decyl (n-C₁₀H₂₁) group-functionalized amorphous SiO₂ [18] (labeled as n-C₁₀H₂₁-SiO₂ and shown in Fig. 2-4(a)).

Another reference sample, the PCS(UH)-derived SiCH hybrid (labeled as SiCH.UH) showed highest hydrophobicity, and the associated isotherms was classified as type III isotherms, signifying weak interactions between adsorbent and adsorbate (Fig. 2-4(b)) [19,20]. To examine the slight difference in the hydrophobic character between the SiCH.L and SiCH.UH, FT-IR spectroscopic analysis was performed on these samples (Fig. 2-5). The spectra of the two samples presented common absorption bands correspond to the organic group at 2950-2900 cm⁻¹ (ν C-H), 2100 cm⁻¹ (ν Si-H), 1450-1350 cm⁻¹ (ν C-H in CH, CH₂ and CH₃), 1250 cm⁻¹ (ν Si-CH₃), 1020 cm⁻¹ (γ CH₂ in Si-CH₂-Si) and around 800 cm⁻¹ (γ Si-CH₃ and ν Si-H in SiC₄) [25,26]. As expanded and shown in Fig. 2-5, both of the two samples exhibited weak bands above 3000 cm⁻¹. The broad band centered at 3400 cm⁻¹ was attributed to intermolecular hydrogen-bonded silanol (Si-OH) group and adsorbed water molecules originated from ambient moisture, whereas the sharp band at 3674 cm⁻¹ was assigned to free Si-OH group [15,26]. The density of the free Si-OH group in each SiCH hybrid sample was determined from the relative ratio of the FT-IR absorption band intensities: $I(\text{Si-OH})$ at 3674 cm⁻¹/ $I(\text{Si-CH}_2\text{-Si})$ at 1020 cm⁻¹, and found as 0.07 in SiCH.L. This value was 3.5 times higher than that in the SiCH.UH (0.02).

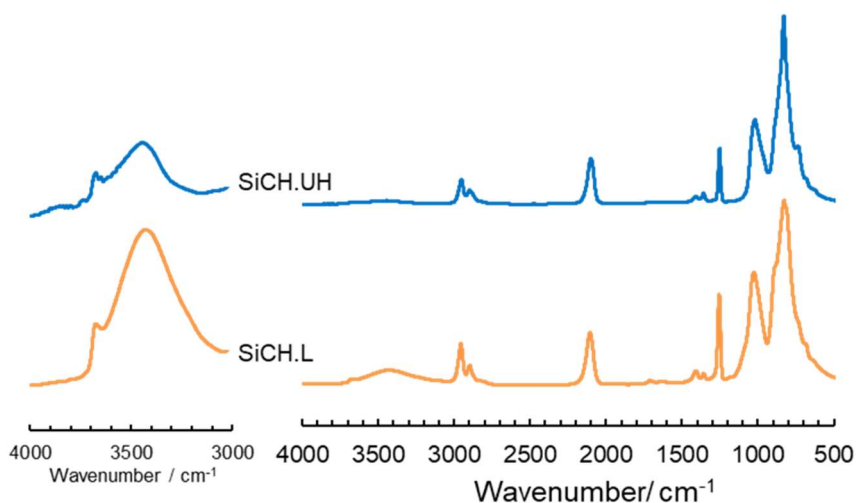


Fig. 2-5. FT-IR spectra for PCS-derived SiCH-based organic-inorganic hybrid samples derived from PCS Type L and Type UH.

The heat treatment condition applied for the SiCH synthesis in this study was 120 °C in air, and thus PCS.UH could keep the solid state of the starting PCS(UH), while PCS.L was formed through the melt-solidification of PCS(L) having much smaller Mw, *i.e.* having higher number of end group (Fig. 2-2). One possible reason for the higher Si-OH density in the PCS.L was due to the additional Si-OH groups formed in-situ by the air-oxidation at the end groups of carbosilane polymer molecules during the melt-solidification process.

As previously discussed [18,26–29], surface Si-OH groups offered preferential adsorption sites for water molecules which could lead to increasing amount of adsorbed water on the SiCH.L at lower humidity. However, at $p/p_0(\text{H}_2\text{O}) > 0.3$, the SiCH.L presented type III isotherms and remained significantly hydrophobic, which was consistent with the purpose of our present study.

2.3.2 Modification of mesoporous $\gamma\text{-Al}_2\text{O}_3$ membrane on a macroporous support

A typical cross-sectional SEM image of the supported $\gamma\text{-Al}_2\text{O}_3$ membrane is shown in Fig. 2-6. Defect-free thin layer with a thickness of approximately 4.5 μm was observed on a macroporous $\alpha\text{-Al}_2\text{O}_3$ support. As shown in Fig. 2-7, the pore size distribution of the $\gamma\text{-Al}_2\text{O}_3$ membrane located below 4 nm and presented a dominant peak at 3.3 nm. The mesoporous $\gamma\text{-Al}_2\text{O}_3$ membrane was modified by dip-coating of PCS(L) and subsequent 120 °C-heat treatment. Then, EDS mapping analysis was performed on the modified membrane. As a typical result, the line scan of EDS mapping for the PCS(L)-derived Si is shown in Fig. 2-8. By the melt impregnation of PCS(L) utilized in this study, the entire mesoporous $\gamma\text{-Al}_2\text{O}_3$ membrane layer was successfully modified with hydrophobic SiCH-based organic-inorganic hybrid.

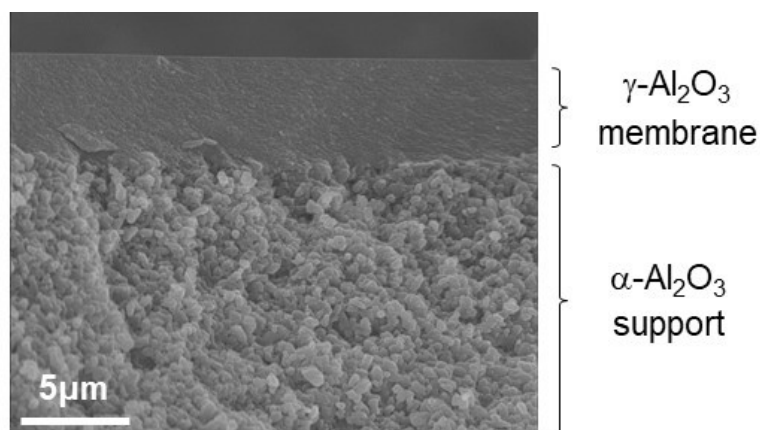


Fig. 2-6. Cross-sectional SEM image of mesoporous $\gamma\text{-Al}_2\text{O}_3$ membrane formed on a macroporous $\alpha\text{-Al}_2\text{O}_3$ support.

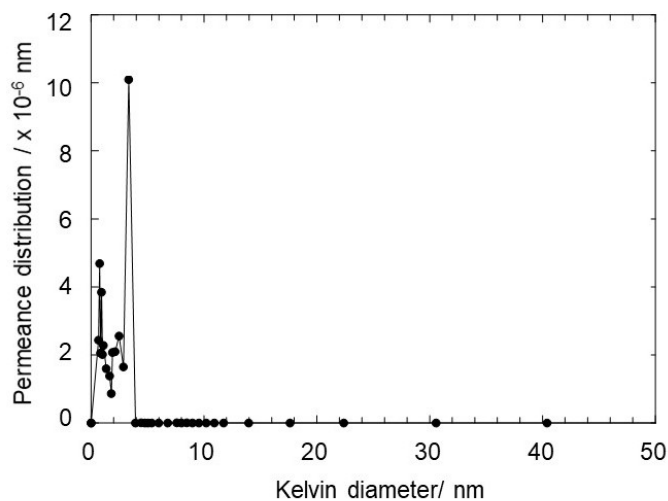


Fig. 2-7. Pore size distribution of the supported mesoporous γ - Al_2O_3 membrane.

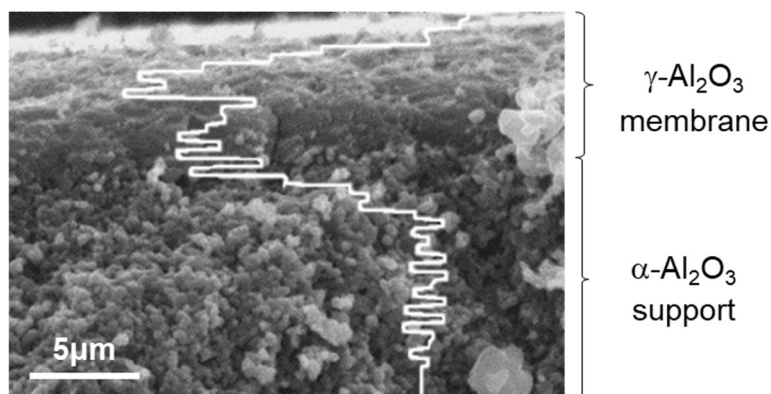


Fig. 2-8. Quantitative line scan of EDS mapping for Si showing nearly uniform distribution of SiCH-based organic-inorganic hybrid within the mesoporous γ - Al_2O_3 membrane after modification by the melt-impregnation of PCS(L).

2.3.3 Effect of SiCH-modification on gas permeation properties of mesoporous γ - Al_2O_3 membrane

2.3.3.1 Gas permeation behaviors under dry condition

The gas permeances at 25 to 80 °C under dry condition of as-synthesized mesoporous γ - Al_2O_3 membrane were proportional to the reciprocal of the square root of the molecular weight, M (Fig. 2-9(a)). Moreover, for all the gas permeation behaviors, the variation of gas permeance with the reciprocal of the square root of permeation temperature gave the linear relationship (Fig. 2-9(b)).

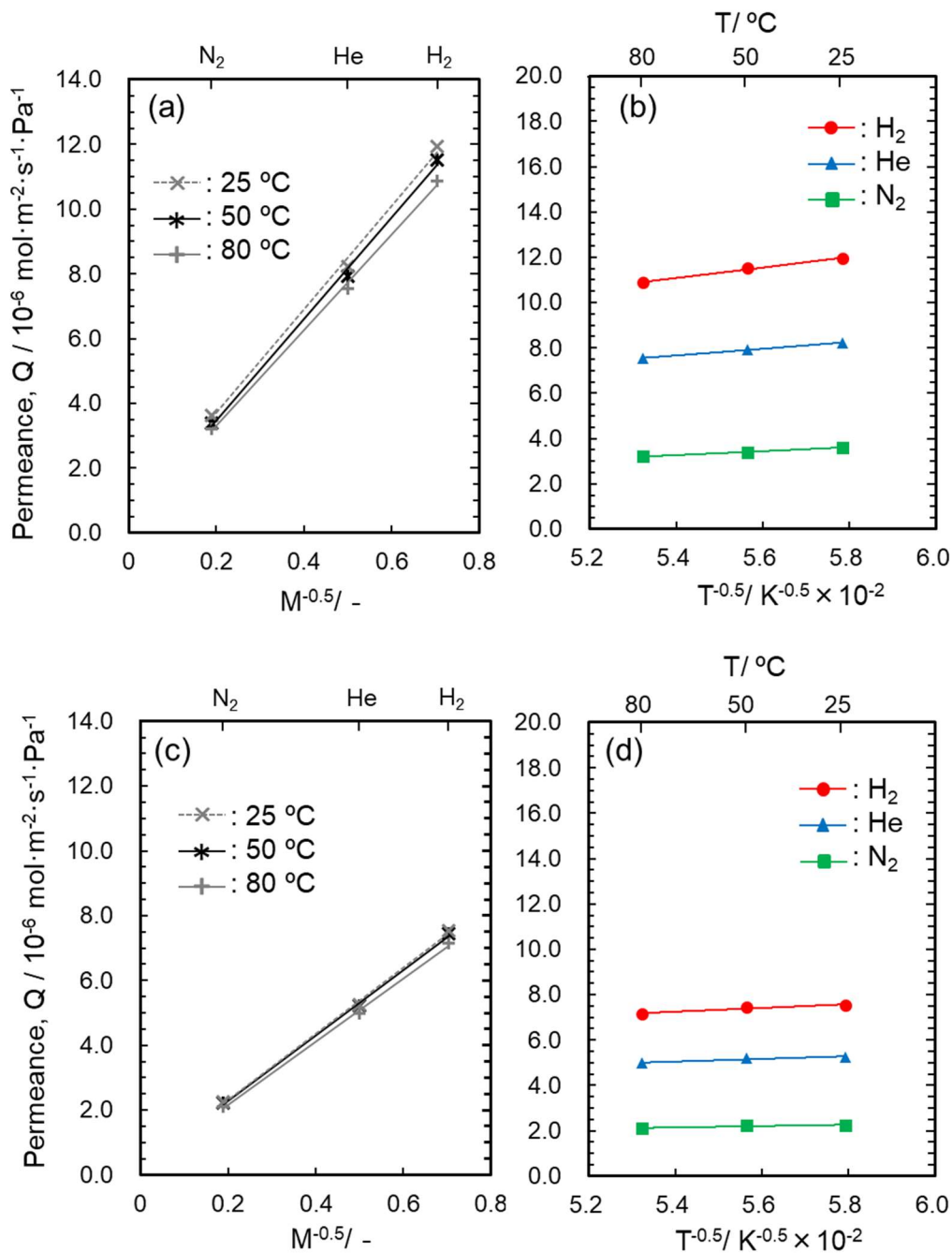


Fig. 2-9. Gas permeation behaviors under dry condition of mesoporous $\gamma\text{-Al}_2\text{O}_3$ membrane. (a), (b) as-synthesized and (c), (d) after modification with PCS (Type L)-derived SiCH-based organic-inorganic hybrid.

The theoretical gas permeance based on the Knudsen diffusion through a membrane having membrane pore radius (d_p), porosity (ϵ), tortuosity (τ) and thickness (L) is formulated using the molecular weight of the permeating component (M) and the temperature (T) as follows,

$$Q_i = \varepsilon_i d_{p,i} \rho_i \left(\frac{8RT}{\pi M_i} \right)^{1/2} \frac{1}{RT \tau_i L_i} \quad (2-1)$$

where probability, ρ , which indicates the probability of diffusion through the pore channel, and the membrane structural factors expressed as ρ_i , ε_i , $d_{p,i}$, τ_i , and L_i , due to possible dependence on molecular sizes. Accordingly, Eq. (2-1) gives that permeance (Q_i) is inversely proportional to the square root of M and T .

As shown in Figs. 2-9 (a) and (b), the dominant mechanism for gas permeations through the mesoporous γ -Al₂O₃ membrane synthesized in this study could be explained by the Knudsen's diffusion [11–14]. This indicated that the gas molecules permeated not through defects, but through the micro- and meso-pore channels of the γ -Al₂O₃ membrane.

After the modification with PCS(L)-derived SiCH-based organic-inorganic hybrid, the gas permeation behaviors through the γ -Al₂O₃ membrane were also proportional to $M^{-0.5}$ and $T^{-0.5}$, and thus could be governed by the Knudsen's diffusion mechanism (Figs. 2-9 (c) and (d)). The H₂ permeance at 50 °C changed from 11.5 to 7.5 x 10⁻⁶ mol m⁻² s⁻¹ Pa⁻¹, *i.e.* decreased in 34.5 %, and found to remain sufficiently high [11–14].

2.3.3.2 Gas permeation behaviors under wet condition

The operation temperature for the membrane separation process for hydrogen purification after the water photo-splitting in the novel solar hydrogen production system has been proposed as 50 °C [30]. Thus, under wet condition in this study, gas permeance measurement temperature was fixed as 50 °C. As shown in Figs. 2-10 (a) and (b), the gas permeation behaviors under p/p_0 (H₂O) up to 0.75 of as-synthesized and SiCH-modified mesoporous γ -Al₂O₃ membranes were similar; H₂, He and N₂ permeances slightly decreased with increasing p/p_0 (H₂O). However, at the p/p_0 (H₂O) = 1.0 (saturated water vapor partial pressure at 50 °C), all the gas permeances through the as-synthesized mesoporous γ -Al₂O₃ membrane were below the limit of detection, and only water vapor permeance was measured to be 7 x 10⁻⁷ mol m⁻² s⁻¹ Pa⁻¹ (Fig. 2-10(a)).

Meanwhile, even under the saturated water vapor partial pressure (p/p_0 (H₂O) = 1.0), the SiCH-modified mesoporous γ -Al₂O₃ membrane exhibited much higher gas permeances ranging from 1.2 to 3.0 x 10⁻⁶ mol m⁻² s⁻¹ Pa⁻¹ (Fig. 2-10(b)).

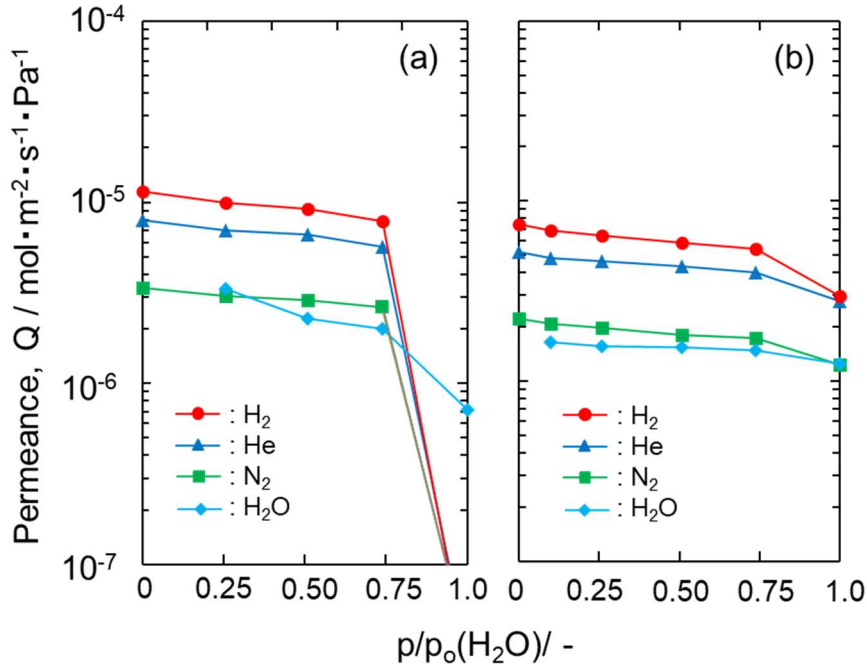


Fig. 2-10. Gas permeances and water vapor permeance evaluated for mesoporous γ - Al_2O_3 membrane under p/p_0 (H_2O) ranging from 0 to 1.0 at 50 °C. (a) as-synthesized and (b) after modification with PCS (Type L)-derived SiCH-based organic-inorganic hybrid.

To investigate the effect of p/p_0 (H_2O) on gas permeation behaviors in more details, water vapor permeances measured in this study were compared with the ideal values calculated by using normalized Knudsen-based permeance (NKP) [31,32]. The NKP (f_{NKP}) is defined as the ratio of the permeance of a target component to that predicted from a reference component based on the Knudsen diffusion mechanism. He, the smallest gas molecule with no sorption properties, would be suitable for the reference component, and the f_{NKP} can be given as follows,

$$f_{NKP} = \frac{Q_i \sqrt{M_i}}{Q_{He} \sqrt{M_{He}}} \quad (2-2)$$

When the f_{NKP} equals one, the target component behaves according to the ideal Knudsen mechanism. Therefore, Q_{k,H_2O} which is the permeance of the target component (H_2O) predicted from the He permeance under the Knudsen diffusion mechanism, can be given as follows,

$$Q_{k,H_2O} = Q_{He} \left(\frac{M_{He}}{M_{H_2O}} \right)^{1/2} \quad (2-3)$$

As shown in Fig. 2-11(a), under the $p/p_0(\text{H}_2\text{O}) = 0.25$, the water vapor permeance measured for the as-synthesized mesoporous $\gamma\text{-Al}_2\text{O}_3$ membrane was consistent with the $Q_{k,\text{H}_2\text{O}}$ calculated from Eq. (2-3). Then, under the $p/p_0(\text{H}_2\text{O})$ ranging from 0.5 to 0.75, the measured water vapor permeance was lower than the $Q_{k,\text{H}_2\text{O}}$. Since the water vapor adsorption-desorption isotherm curves for as-synthesized $\gamma\text{-Al}_2\text{O}_3$ exhibited H3 type hysteresis loop at higher humidity above $p/p_0(\text{H}_2\text{O}) = 0.5$ (Fig. 2-4(a)), the lower water vapor permeance could be due to the partial blockage of micro- and meso-pore channels by condensation of water molecules. At the $p/p_0(\text{H}_2\text{O}) = 1.0$, most of the pore channels could be blocked, which lead to the observed rejection of other gas molecules, while water vapor kept the driving force for permeating through the $\gamma\text{-Al}_2\text{O}_3$ membrane.

In contrast to the as-synthesized $\gamma\text{-Al}_2\text{O}_3$ membrane, the water vapor permeance through the SiCH-modified $\gamma\text{-Al}_2\text{O}_3$ membrane was lower than the $Q_{k,\text{H}_2\text{O}}$ under whole range of $p/p_0(\text{H}_2\text{O})$ (Fig. 2-11(b)). Essentially, the water vapor permeation through the $\gamma\text{-Al}_2\text{O}_3$ membrane was found to be suppressed by modifying inner surfaces of micro- and meso-pore channels with highly hydrophobic SiCH-based organic-inorganic hybrid. This could contribute to preventing the serious water condensation under the present humid condition of saturated water vapor partial pressure at 50 °C.

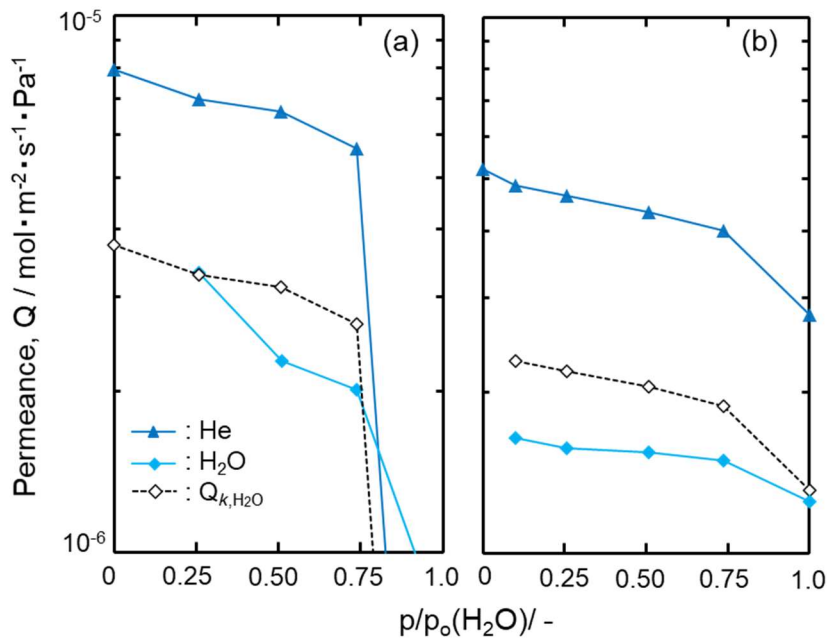


Fig. 2-11. Comparison of experimentally evaluated He and water vapor permeances with $Q_{k,\text{H}_2\text{O}}$ predicted by using f_{NKP} for mesoporous $\gamma\text{-Al}_2\text{O}_3$ membrane under $p/p_0(\text{H}_2\text{O})$ ranging from 0 to 1.0 at 50 °C. (a) as-synthesized and (b) after modification with PCS (Type L)-derived SiCH-based organic-inorganic hybrid.

2.4 Summary

In the present study, excellent hydrophobicity of PCS-derived SiCH-based organic-inorganic hybrid was characterized by measuring water vapor adsorption and desorption isotherms at room temperature. Then, the effect of the SiCH modification on gas permeation properties of conventional sol-gel-derived hydrophilic mesoporous γ -Al₂O₃ membrane placed on a macroporous α -Al₂O₃ support was assessed and discussed to prepare a gas permeable mesoporous intermediate layer essential for a stable H₂ gas separation ceramic-based membrane that functions under the proposed humid condition up to 50 °C for the H₂ purification process in the novel solar hydrogen production system. The results can be summarized as follows:

Water vapor adsorption-desorption isotherms measurement revealed that the maximum amount of water adsorption (V_a (H₂O)) at room temperature of conventional sol-gel-derived γ -Al₂O₃ was as high as 297 cm³(STP)g⁻¹. In contrast, V_a (H₂O) at room temperature of the PCS-derived SiCH-based organic-inorganic hybrid was below 8 cm³(STP)g⁻¹, showing excellent hydrophobicity.

Under the present humid condition, the permeances of He, H₂ and N₂ gas molecules through the supported mesoporous γ -Al₂O₃ membrane slightly decreased consistently with the p/p_0 (H₂O) up to 0.75. Then, under p/p_0 (H₂O) =1.0, all the gas permeances dropped below the detection limit, which could be due to the blockage of the gas permeable micro- and meso-pore channels by water condensation.

Modification with PCS(L)-derived SiCH-based organic-inorganic hybrid successfully improved the gas permeability through the mesoporous γ -Al₂O₃ membrane under the high humid condition: even under the saturated water vapor partial pressure (p/p_0 (H₂O) =1.0) at 50 °C, all the gas molecules of He, H₂ and N₂ kept high permeances of 1.2 to 3.0 x 10⁻⁶ mol m⁻² s⁻¹ Pa⁻¹.

PCS(L)-derived SiCH-based organic-inorganic hybrid investigated in this study is useful as a modifier to maintain sufficient gas permeations through an intrinsically hydrophilic ceramic-based mesoporous intermediate layer placed within the multilayered ceramic-based composite membrane, which is expected to contribute to develop H₂-selective ceramic-based membranes with applications to novel solar hydrogen system.

References

- [1] Q. Wang, T. Hisatomi, Q. Jia, H. Tokudome, M. Zhong, C. Wang, Z. Pan, T. Takata, M. Nakabayashi, N. Shibata, Y. Li, I.D. Sharp, A. Kudo, T. Yamada, K. Domen, Scalable water splitting on particulate photocatalyst sheets with a solar-to-hydrogen energy conversion efficiency exceeding 1%, *Nat. Mater.* 15 (2016) 611–615.
- [2] Y. Goto, T. Hisatomi, Q. Wang, T. Higashi, K. Ishikiriyama, T. Maeda, Y. Sakata, S. Okunaka, H. Tokudome, M. Katayama, S. Akiyama, H. Nishiyama, Y. Inoue, T. Takewaki, T. Setoyama, T. Minegishi, T. Takata, T. Yamada, K. Domen, A Particulate Photocatalyst Water-Splitting Panel for Large-Scale Solar Hydrogen Generation, *Joule* 2 (2018) 509–520.

- [3] K. Tanaka, Y. Sakata, Present and Future Prospects of Hydrogen Production Process Constructed by the Combination of Photocatalytic H₂O Splitting and Membrane Separation Process, *Membrane* 36 (2011) 113–121.
- [4] R.M. de Vos, H. Verweij, High-Selectivity, High-Flux Silica Membranes for Gas Separation, *Science* 279 (1998) 1710–1711.
- [5] Y. Iwamoto, K. Sato, T. Kato, T. Inada, Y. Kubo, A hydrogen-permselective amorphous silica membrane derived from polysilazane, *J. Eur. Ceram. Soc.* 25 (2005) 257–264.
- [6] Y. Iwamoto, Precursors-Derived Ceramic Membranes for High-Temperature Separation of Hydrogen, *J. Ceram. Soc. Japan* 115 (2007) 947–954.
- [7] T. Nagano, S. Fujisaki, K. Sato, K. Hataya, Y. Iwamoto, M. Nomura, S.-I. Nakao, Relationship between the mesoporous intermediate layer structure and the gas permeation property of an amorphous silica membrane synthesized by counter diffusion chemical vapor deposition, *J. Am. Ceram. Soc.* 91 (2008) 71–76.
- [8] A.K. Prabhu, S.T. Oyama, Highly hydrogen selective ceramic membranes: Application to the transformation of greenhouse gases, *J. Memb. Sci.* 176 (2000) 233–248.
- [9] A. Burneau, J. Lepage, G. Maurice, Porous silica-water interactions. I. Structural and dimensional changes induced by water adsorption, *J. Non. Cryst. Solids* 217 (1997) 1–10.
- [10] T. Tsuru, T. Hino, T. Yoshioka, M. Asaeda, Permporometry characterization of microporous ceramic membranes, *J. Memb. Sci.* 186 (2001) 257–265.
- [11] M.H. Zahir, K. Sato, Y. Iwamoto, Development of hydrothermally stable sol–gel derived La₂O₃-doped Ga₂O₃–Al₂O₃ composite mesoporous membrane, *J. Memb. Sci.* 247 (2005) 95–101.
- [12] M.H. Zahir, K. Sato, H. Mori, Y. Iwamoto, M. Nomura, S.I. Nakao, Preparation and properties of hydrothermally stable γ -alumina-based composite mesoporous membranes, *J. Am. Ceram. Soc.* 89 (2006) 2874–2880.
- [13] M.H. Zahir, Y.H. Ikuhara, S. Fujisaki, K. Sato, T. Nagano, Y. Iwamoto, Preparation and characterization of mesoporous ceria–zirconia–alumina nanocomposite with high hydrothermal stability, *J. Mater. Res.* 22 (2007) 3201–3209.
- [14] M.H. Zahir, S. Fujisaki, K. Sato, T. Nagano, Y. Iwamoto, Mesoporous CeO₂-ZrO₂- γ -Al₂O₃ nanocomposite membranes exhibiting remarkable hydrothermal stability, *Desalin. Water Treat.* 2 (2009) 229–236.
- [15] Y. Sawai, Y. Iwamoto, S. Okuzaki, Y. Yasutomi, K. Kikuta, S. Hirano, Synthesis of Silicon Carbide Ceramics Using Chemically Modified Polycarbosilanes as a Compaction Binder, *J. Am. Ceram. Soc.* 82 (1999) 2121–2125.
- [16] Nippon Carbon Co, LTD, Technical Information, Polycarbosilanes “Nipusi®”, 19, May, 1995, (1995).
- [17] T. Nagano, K. Sato, T. Saitoh, Y. Iwamoto, Gas permeation properties of amorphous SiC membranes synthesized from polycarbosilane without oxygen-curing process, *J. Ceram. Soc. Japan* 114 (2006) 533–538.
- [18] M.N. Mohd Sokri, T. Onishi, Y. Daiko, S. Honda, Y. Iwamoto, Hydrophobicity of amorphous silica-based inorganic-organic hybrid materials derived from perhydropolysilazane chemically modified with alcohols, *Microporous Mesoporous Mater.* 215 (2015) 183–190.

- [19] K.S.W. Sing, D.H. Everett, R.A.W. Haul, L. Moscou, R.A. Pierotti, J. Rouquerol, T. Siemienieska, Reporting physisorption data for gas/solid systems with special reference to the determination of surface area and porosity, *Pure Appl. Chem.* 57 (1985) 603–619.
- [20] S. Lowell, J.E. Shields, M.A. Thomas, M. Thommes, *Characterization of porous solids and powders*, Springer, Netherlands, 2004.
- [21] A.F.M. Leenaars, K. Keizer, A.J. Burggraaf, The preparation and characterization of alumina membranes with ultra-fine pores, *J. Mater. Sci.* 19 (1984) 1077–1088.
- [22] A.F.M. Leenaars, A.J. Burggraaf, The preparation and characterization of alumina membranes with ultrafine pores. 2. The formation of supported membranes, *J. Colloid Interface Sci.* 105 (1985) 27–40.
- [23] R.J.R. Uhlhorn, M.H.B.J. Huis In't Veld, K. Keizer, A.J. Burggraaf, Synthesis of ceramic membranes - Part I Synthesis of non-supported and supported γ -alumina membranes without defects, *J. Mater. Sci.* 27 (1992) 527–537.
- [24] M. May, J. Navarrete, M. Asomoza, R. Gomez, Tailored mesoporous alumina prepared from different aluminum alkoxide precursors, *J. Porous Mater.* 14 (2007) 159–164.
- [25] H.Q. Ly, R. Taylor, R.J. Day, F. Heatley, Conversion of polycarbosilane (PCS) to SiC-based ceramic: Part 1. Characterisation of PCS and curing products, *J. Mater. Sci.* 36 (2001) 4037–4043.
- [26] Z. Mouline, K. Asai, Y. Daiko, S. Honda, S. Bernard, Y. Iwamoto, Amine-functionalized polycarbosilane hybrids for CO₂-selective membranes, *J. Eur. Ceram. Soc.* 37 (2017) 5213–5221.
- [27] Z.D. Hendren, J. Brant, M.R. Wiesner, Surface modification of nanostructured ceramic membranes for direct contact membrane distillation, *J. Memb. Sci.* 331 (2009) 1–10.
- [28] A. Larbot, L. Gazagnes, S. Krajewski, M. Bukowska, W. Kujawski, Water desalination using ceramic membrane distillation, *Desalination* 168 (2004) 367–372.
- [29] S. Koonaphapdeelert, K. Li, Preparation and characterization of hydrophobic ceramic hollow fibre membrane, *J. Memb. Sci.* 291 (2007) 70–76.
- [30] T. Yamada, K. Domen, Development of Sunlight Driven Water Splitting Devices towards Future Artificial Photosynthetic Industry, *ChemEngineering* 2 (2018) 36.
- [31] H.R. Lee, M. Kanezashi, Y. Shimomura, T. Yoshioka, T. Tsuru, Evaluation and fabrication of pore-size-tuned silica membranes with tetraethoxydimethyl disiloxane for gas separation, *AIChE J.* 57 (2011) 2755–2765.
- [32] T. Yoshioka, M. Kanezashi, T. Tsuru, Micropore size estimation on gas separation membranes: A study in experimental and molecular dynamics, *AIChE J.* 59 (2013) 2179–2194.

Chapter 3

Hydrogen Selective SiCH-based Organic-Inorganic Hybrid/ γ -Al₂O₃ Composite Membranes

3.1 Introduction

In Chapter 2, PCSs were found to show an excellent hydrophobic property: gas permeations under highly humid condition at 50 °C of a hydrophilic mesoporous γ -Al₂O₃ membrane were successfully stabilized by modification with SiCH-based organic-inorganic hybrid via melt impregnation of PCS-Type L at 120 °C. However, there was room for advancement in terms of H₂-permselectivity at low temperature and under humid condition, because modified mesoporous γ -Al₂O₃ only showed poor H₂-permselectivity based on the Knudsen' diffusion. Therefore, it was focused that H₂ separation was performed through the PCS-based organic-inorganic hybrid itself by filling the mesopore channels of γ -Al₂O₃ membrane completely. This strategy is expected to be effective in the simultaneous improvement of the hydrostability in terms of stable gas permeations and H₂-permselectivity for the H₂-selective membranes for applications to novel solar hydrogen system.

In this chapter, SiCH-based organic-inorganic hybrid/ γ -Al₂O₃ composite membranes were attempted to fabricate by selecting the chemical structure of a starting Si-based polymer: one of the PCS derivatives, allyl-hydro-polycarbosilane (AHPCS) was selected and converted to highly cross-linked ternary SiCH-based organic-inorganic hybrids with enhanced thermal stability and hydrophobicity by heat treatment at temperatures as low as 300–500 °C in argon (Ar). Highly hydrophobic property of the AHPCS-derived SiCH-based hybrids was characterized by the water vapor adsorption–desorption isotherm measurement at 25 °C. Then, the SiCH-based organic-inorganic hybrid served to modify a mesoporous γ -Al₂O₃ membrane via dip-coating with AHPCS followed by the heat treatment of the composite at 300–500 °C in Ar.

Single gas permeances of helium (He), hydrogen (H₂) and nitrogen (N₂) under dry condition at 25–80 °C were measured to characterize the intrinsic low-temperature gas permeation properties of the SiCH-based organic-inorganic hybrid/ γ -Al₂O₃ composite membrane. Then, as the primary accelerated degradation test for the suggested solar H₂ purification condition of high humidity at 50 °C [1,2], the gas permeance measurements were performed under the saturated water vapor partial pressure at 50 °C. In this measurement, a H₂-N₂ mixed feed gas in the molar ratio 2:1 was used as a simulated syngas produced via photoelectrochemical (PEC) water-splitting reaction (2H₂O→2H₂+O₂) in which O₂ (0.346 nm) [3] was replaced by inert N₂ having a similar kinetic diameter (0.364 nm) [3] to avoid explosion accidents. Moreover, for some selected membrane samples and the supported mesoporous γ -Al₂O₃ membrane itself, cyclic gas permeation measurements were continuously performed under water vapor partial pressures ranging from 0 to 1.0 at 50 °C. Effect of the composite membrane synthesis

temperature on the hydrophobicity and gas permeation properties under dry and wet conditions were discussed aiming to develop novel hydrophobic membranes for the purification of solar hydrogen at low temperatures around 50 °C.

3.2 Experimental Procedures

3.2.1 Preparation of the supported mesoporous γ -Al₂O₃ membrane

A mesoporous γ -Al₂O₃ membrane was prepared under the same manner as mentioned in the section 2.2.1 in Chapter 2, and commercially available macroporous α -Al₂O₃ tubular support (6 mm outer diameter, 4 mm inner diameter and 60 mm length, Noritake Co., Ltd., Nagoya, Japan) was used. The α -Al₂O₃ support was composed of a fine outer surface layer (mean pore diameter: 150 nm) and a core (mean pore diameter: 700 nm). Total porosity of the tubular support was 40%. A mesoporous γ -Al₂O₃ membrane was fabricated by dip coating of a boehmite (γ -AlOOH) sol on the α -Al₂O₃ tubular support followed by heat treatment in air at 600 °C for 3 h.

3.2.2 Modification of a supported γ -Al₂O₃ membrane with AHPCS-derived organic-inorganic SiCH hybrid

Commercially available AHPCS (SMP-10 was provided by Starfire Systems, Inc., Glenville, NY, USA. Anal. Found (wt %): Si, 54.8; C, 35.0; H, 8.3; O, 1.9. FT-IR (ATR/cm⁻¹): ν (C-H) = 3076 (s), 3003 (s), 2958 (s), 2895 (s), 2850 (m), ν (Si-H) = 2123 (vs), δ (allyl) = 1629 (m), δ (CH₂) = 1395 (m), δ (Si-CH₃) = 1251 (s), δ (Si-CH₂-Si) = 1049 (s), δ (Si-H) = 941.1 (s), δ (Si-C) = 854.3 (s), δ (SiCH₃) = 770 (s); ¹H NMR (300 MHz, CDCl₃, δ /ppm): 0.05 (br, -Si-CH₃), 0.4 (br, -Si-CH₂-), 1.56–1.9 (br, -Si-CH₂-CH=CH₂), 3.4–3.84 (br, -SiH₃C), 3.8–4.1 (br, -SiH₂CH₂), 4.85–5.05 (br, -Si-CH₂-CH=CH₂), 5.71–5.93 (br, Si-CH₂-CH=CH₂). Chemical structure of the AHPCS is shown in Fig. 3-1.

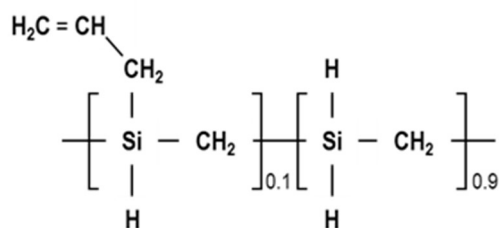


Fig. 3-1. Structure of commercially available allyl-hydrido-polycarbosilane (AHPCS).

As a precursor solution for modifying the supported γ -Al₂O₃ membrane, 1 wt % dry xylene (super dehydrated grade, 99.5% purity, Wako Pure Chemical Co., Ltd., Osaka, Japan) solution of as-received AHPCS was prepared under the inert atmosphere of Ar. By following the procedures described in the section 2.2.2 in Chapter 2, the AHPCS solution was dip-coated on the supported γ -Al₂O₃ membrane, then dried and heat-treated under flowing Ar at 300, 400 and 500 °C for 1 h at a heating/cooling rate of 100 °C h⁻¹ to afford SiCH-based organic-inorganic hybrid-modified γ -Al₂O₃ membrane placed on the

α -Al₂O₃ tubular support (SiCH-based hybrid/ γ -Al₂O₃ composite membrane). Flow chart of fabrication for SiCH-based hybrid/ γ -Al₂O₃ composite membranes is shown in Fig. 3-2.

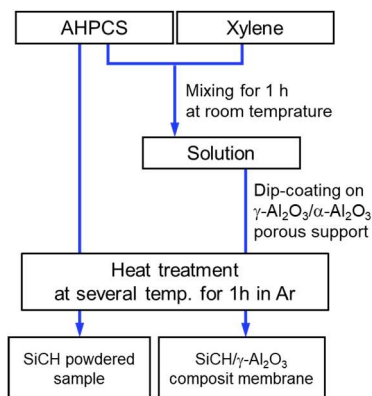


Fig. 3-2. Flow chart of fabrication for SiCH-based hybrid/ γ -Al₂O₃ composite membranes and preparation of AHPCS-derived powder samples.

The 500 °C-heat treated membrane was further modified by the melt impregnation of a commercially available PCS at 120 °C under Ar atmosphere (Type L, Nippon Carbon Co., Ltd., Tokyo, Japan) according to the section 2.2.2 in Chapter 2.

3.2.3 Characterizations

The molecular weight distribution curve of as-received AHPCS was measured at 40 °C by using gel permeation chromatography (GPC, Model ShodexGPC-104 equipped with two tandem columns (Model Shodex LF-404, Showa Denko K.K., Tokyo, Japan) and a refractive index detector (Model Shodex RI-74S, Showa Denko K.K., Tokyo, Japan). The columns were calibrated against polystyrene standards. Tetrahydrofuran (THF, 99.5% purity, Wako Pure Chemical Co., Ltd., Osaka, Japan) was used as the eluent and a flow rate was adjusted to 1.0 mL min⁻¹.

The thermal decomposition and cross-linking behaviors of as-received AHPCS up to 1000 °C was studied by thermogravimetry combined with mass spectrometry (TG-MS) analyses (Model STA7200, Hitachi High Technologies Ltd., Tokyo, Japan/Model JMS-Q1500 GC, JEOL, Tokyo, Japan). The measurements were performed under He atmosphere with a heating rate of 10 °C min⁻¹.

Powder samples of the heat-treated AHPCS were prepared under the same manner for the heat treatment of the supported mesoporous γ -Al₂O₃ membrane after dip-coating of the AHPCS solution (Fig. 3-2).

Fourier transform (FT)-IR spectrum was recorded on the as-received AHPCS and AHPCS-derived powder samples by the potassium bromide (KBr) disk method (Model FT/IR-4200IF, JASCO Corp., Tokyo, Japan). Note that FT-IR spectrum was also recorded on the powder sample of 700 °C-heat treated AHPCS. Raman spectrum was

recorded on as-received AHPCS and heat-treated AHPCS (Renishaw, inVia Reflex, New Mills, England).

Hydrophobicity of the heat-treated AHPCS powder samples was characterized by measuring the water vapor adsorption–desorption isotherms at 25 °C (Model BELSORP-aqua 3, MicrotracBEL Corp., Osaka, Japan). The powder samples were pretreated at 120 °C for 6 h under vacuum.

The cross-sectional structure and top surface of the SiCH-hybrid/ γ -Al₂O₃ composite membrane were observed by a scanning electron microscope (SEM, Model JSM-6360LV, JEOL Ltd., Tokyo, Japan). The distribution of the SiCH hybrid within the composite membrane was examined by the energy dispersive X-ray spectroscopic (EDS) analysis (Model JSM-6010LA mounted on SEM, JEOL Ltd., Tokyo, Japan).

Single gas permeances through the membrane samples under dry conditions were measured for He, H₂ and N₂ by the volumetric method at constant pressure. The setup of the equipment and procedure for the measurements was shown in the section 1.5.1 and Fig. 1-13 in Chapter 1. The gas permeances at 25, 50 and 80 °C were measured in the size order of a kinetic diameter for He (0.26 nm), H₂ (0.289 nm) and N₂ (0.364 nm) [3]. In this study, the ($p_H - p_L$) in Eq. (1-35) was fixed as 100 kPa.

The permselectivity (α) was evaluated by calculating the single gas permeance ratio of two different kinds of gases.

H₂ and N₂ gas permeances under dry and wet condition of the saturated water vapor partial pressure (p/p_0 (H₂O) = 1.0) were measured at 50 °C using a mixed feed gas with a 2:1 molar ratio of H₂ and N₂ as a simulated syngas produced by the PEC reaction. For some selected membranes and the supported mesoporous γ -Al₂O₃ membrane itself, cyclic gas permeation measurements were performed under various p/p_0 (H₂O) ranging from 0 to 1.0 at 50 °C.

The permeances of each gas included in the mixed gas can calculate based on gas composition analysis by a gas chromatography and a flow rate measurement by using Eq. (1-36). The permeate gas composition was analyzed using a gas chromatograph (GC, Model CP-4900 Micro-GC, Varian medical systems Inc., Palo Alto, CA, USA) and Ar sweep gas (50 mL min⁻¹). Each gas permeance of H₂ and N₂ was calculated using the analyzed composition and the measured mixed gas permeate molar flow rate. The water vapor permeance was evaluated using a gas chromatograph for the polar gas analysis (GC323, GL Sciences Inc., Tokyo, Japan).

The membrane performance under the H₂-N₂ (2:1) mixed feed gas flow at p/p_0 (H₂O) = 1.0 was assessed in terms of the separation factor (SF):

$$SF = \frac{Y_A/Y_B}{X_A/X_B} \quad (3-1)$$

where Y and X are the mass fractions of permeate and feed, respectively and subscripts A and B denote H₂ and N₂, respectively.

The permselectivity (α) was evaluated by calculating the gas permeance ratio of two different kinds of gases.

To examine the hydrogen affinity of the AHPCS-derived SiCH organic-inorganic hybrids, the amount of H₂ adsorption onto a thin film of the AHPCS-derived hybrid was measured using a quartz-crystal microbalance (QCM), which is one of the useful methods for detecting in-situ minute mass changes [4]. Commercially available quartz crystal unit (SEN-9E-H-10, Tamadevice Co., Ltd., Kawasaki, Japan) connected with a crystal oscillator circuit (Tamadevice Co. Ltd., Kawasaki, Japan), power supply (GPS-S, GW Instek, Texio Technology Co., Yokohama, Japan) and frequency counter (SC-7205A, UNIVERSALCOUNTER, Iwatsu Electric Co., Ltd., Tokyo, Japan) were used, and the measurement system shown in Fig. 3-3 was set-up at our laboratory.

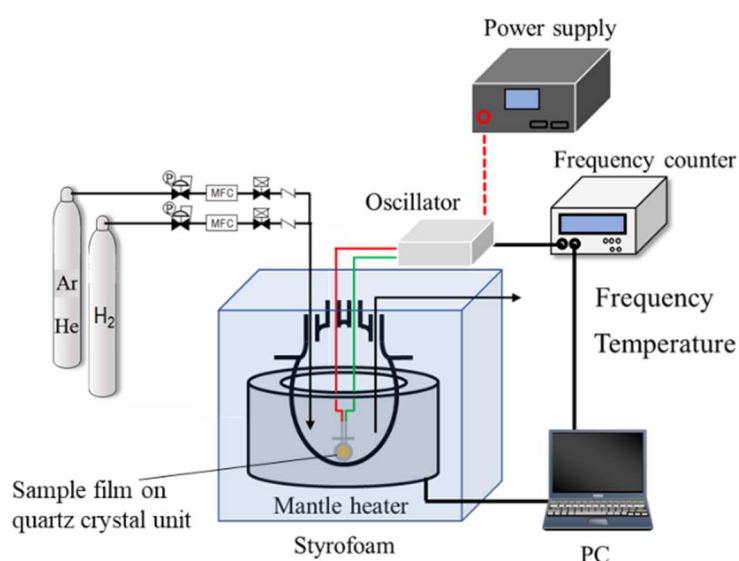


Fig. 3-3. Schematic diagram of the weight change measurement with the quartz crystal microbalance (QCM).

The sample film was formed on the quartz crystal unit surface using the dry xylene solution of as-received AHPCS under the same manner as mentioned for the 300 °C-synthesized membrane. The sample film on the quartz crystal unit was placed in a four-necked round-bottom glass flask. Then, the temperature inside the flask was precisely adjusted at 30 °C (± 0.1 °C) by a styrofoam-covered mantle heater operated by the PID control. The sample film was exposed to He atmosphere maintained by a continuous He gas flow at 30 mL min⁻¹. After 15 h, the frequency shift was measured for 90 ks to confirm that the He adsorption reached the equilibrium. Then, the weight change measurement under a H₂ flow (30 mL min⁻¹) was started by switching the feed gas from He to H₂, and the weight change was monitored for an additional 90 ks. The measurement system was controlled by a standard PC with a software (Labview, National Instruments Corp., Austin, TX, USA) for recording the transition of the frequencies corresponding to the mass change.

Conversion from the measured frequency shift Δf (Hz) to the mass change Δm (g) was calculated using the Sauerbrey equation [5],

$$\Delta f = -\frac{2f_0^2}{\sqrt{\mu_q \rho_q}} \frac{\Delta m}{A_e} \quad (3-2)$$

where, f_0 is the frequency of the quartz crystal prior to a mass change (9.0×10^6 [Hz]), μ_q is the shear modulus of quartz (2.947×10^{13} [$\text{g m}^{-1} \text{s}^{-2}$]), ρ_q is the density of quartz (2.648 [g cm^{-3}]) and A_e is the electrode area (3.93×10^{-5} [m^2]).

3.3 Results and Discussion

3.3.1 Heat treatment temperatures selected for highly cross-linked SiCH-based organic-inorganic hybrid synthesis

Chemical structure and molecular weight distribution of the AHPCS are shown in Figs. 3-1 and 3-4, respectively. In this study, the SiCH-based hybrid polymer of AHPCS was converted into the highly cross-linked SiCH-based organic-inorganic hybrid as a component of the hydrogen separation membrane. The temperatures for thermal conversion of AHPCS to highly cross-linked SiCH-based hybrid in this study was selected as 300, 400 and 500 °C based on the results obtained by the TG-MS analyses (Figs. 3-5 and 3-6) as well as FT-IR and Raman spectroscopic analyses for the heat-treated AHPCSs (Figs. 3-7 and 3-8). The thermal behavior of AHPCS has been already studied by several research groups [6–11], and the results obtained in this study were well consistent with those previously reported: As shown in Fig. 3-4, as-received AHPCS had a considerable amount of low molecular weight fraction below 1000. TG-MS analyses revealed the thermal decomposition of the low molecular weight fraction proceeded during the first weight loss at 100–300 °C and a second one from 350 to 500 °C by detecting gaseous species assigned to the fragments of carbosilane species (Fig. 3-5 and 3-6). On the other hand, thermal cross-linking was observed up to 300 °C for the formation of $\equiv\text{Si-CH}_2\text{-CH}_2\text{-CH}_2\text{-Si}\equiv$ and/or $\equiv\text{Si-CH}(\text{CH}_3)\text{-CH}_2\text{-Si}\equiv$ via hydrosilylation between $\equiv\text{Si-H}$ and $\equiv\text{Si-CH}_2\text{-CH=CH}_2$ groups in AHPCS, which was identified by the disappearance of the FT-IR absorption band at 1629 cm^{-1} attributed to the C=C bond of the allyl group [8,9] associated with the decrease in the relative FT-IR band intensities assigned to $\nu(\text{Si-H})$ at 2123 cm^{-1} and $\delta(\text{Si-H})$ at 947 cm^{-1} [8,9] (Fig. 3-7).

At 400–700 °C, formation of $\equiv\text{Si-Si}\equiv$ between Si-H and Si-CH₃ groups [6] was suggested by detecting gaseous species at the m/z ratio of 15 assigned to methane (CH₄; Fig. 3-6(b)). Since the thermal decomposition and cross-linking contentiously proceeded at 300–500 °C, the quantity of organic groups and microporosity of the SiCH hybrid differed depending on the specific heat treatment temperature in this temperature range. On the other hand, the FT-IR spectrum for the 700 °C-heat treated AHPCS revealed that polymer/inorganic silicon carbide conversion almost completed (Fig. 3-7). It should be noted that the samples heat-treated at 300–500 °C were identified as the ternary SiCH

Class II hybrid without graphite-like carbon, since the Raman spectra of these samples exhibited several peaks due to the organic groups without those attributed to graphite-like carbon typically detected at 1347.5 and 1596.5 cm^{-1} assigned as D-band (for disordered graphite) and G-band (for the sp^2 graphite network), respectively [12,13] (Fig. 3-8). Based on these results, the heat treatment of AHPCS was achieved at 300, 400 and 500 $^{\circ}\text{C}$ for the synthesis of powder and membrane samples.

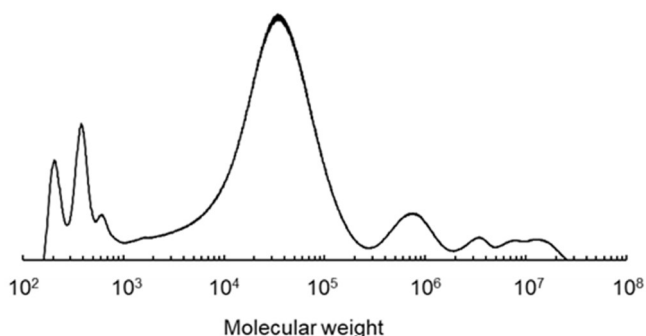


Fig. 3-4. Molecular weight distribution of as-received AHPCS.

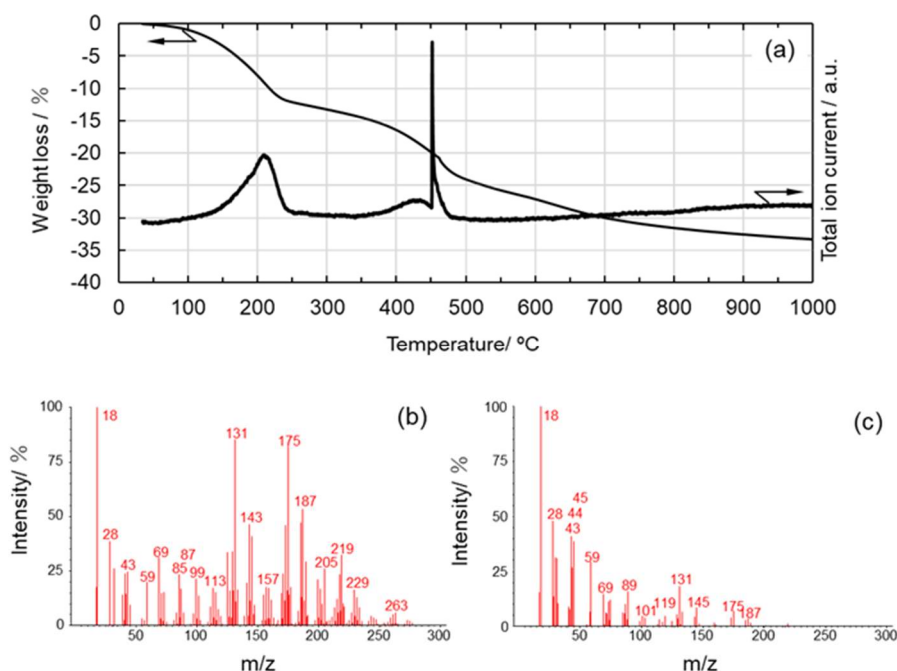


Fig. 3-5. Thermal behavior of as-received AHPCS. (a) TG curve and total ion current chromatogram (TICC) under flowing He, and typical mass spectra recorded during (b) the first weight loss from 100 to 250 $^{\circ}\text{C}$ and (c) the second weight loss from 350 to 500 $^{\circ}\text{C}$.

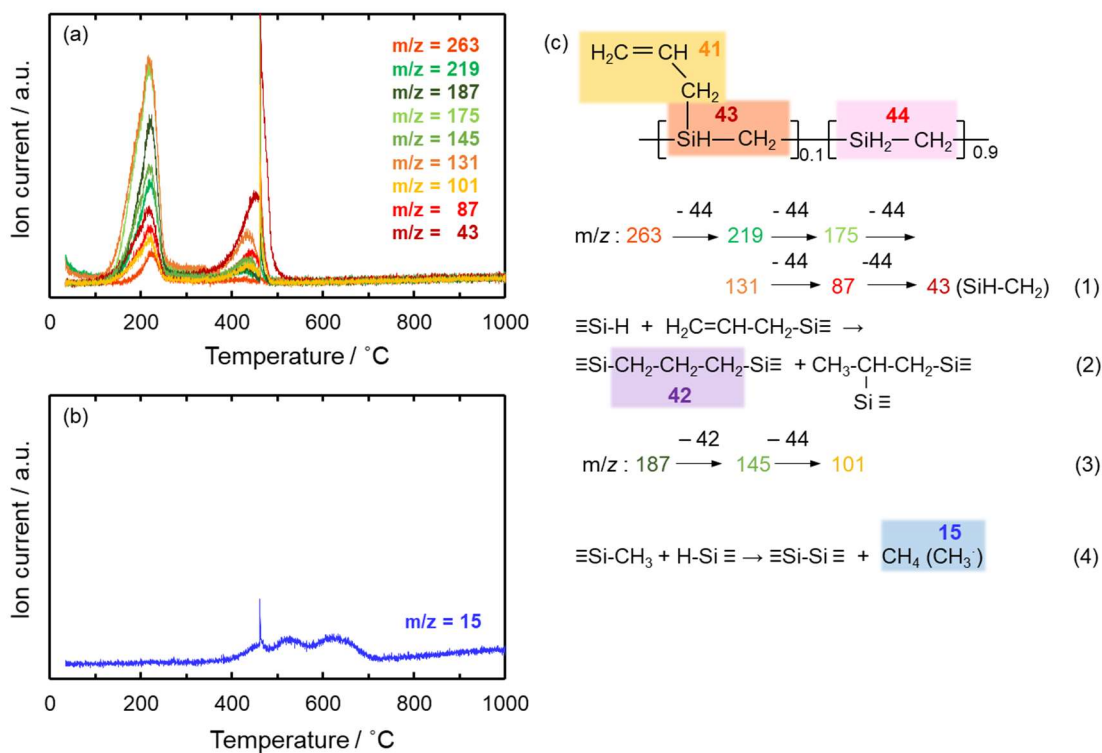


Fig. 3-6. Continuous in-situ monitoring of gaseous species by mass spectrometry: (a) Fragments derived from low molecular weight fraction of as-received AHPCS during the first weight loss from 100 to 300 °C and the second one from 350 to 500 °C and (b) methane (CH₄) at 400 to 700 °C. (c) Fragments suggested for gaseous species derived from low molecular weight fraction of as-received AHPCS (Eq. (1)), m/z= 42 ((CH₂)₃) from AHPCS after cross-linking via hydrosilylation between ≡Si-H and CH₂=CH-CH₂-Si≡ (Eqs. (2) and (3)) and m/z= 15 (CH₄) due to the thermal crosslinking between ≡Si-H and ≡Si-CH₃ groups to afford ≡Si-Si≡ above 350 °C (Eq. (4)) [6].

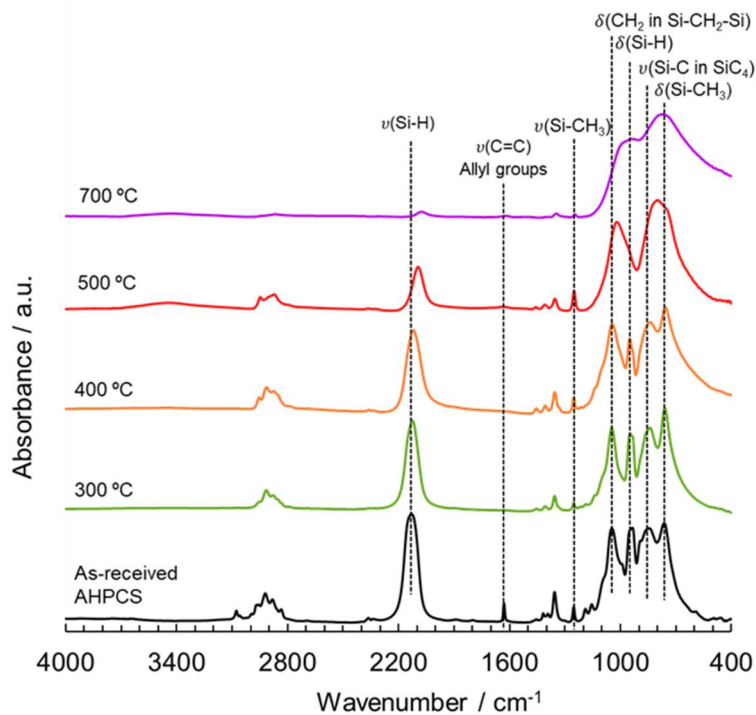


Fig. 3-7. FT-IR spectra for as-received AHPCS and those after heat treatment at 300 to 700 °C in Ar.

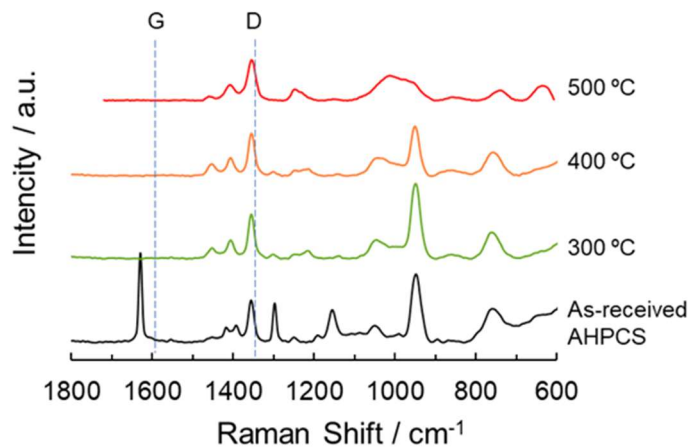


Fig. 3-8. Raman spectra for as-received AHPCS and those after heat treatment at 300 to 500 °C in Ar. Spectra indicated the heat-treated samples were free from graphite-like carbon typically detected at 1347.5 and 1596.5 cm^{-1} attributed to the D-band (for disordered graphite) and G-band (for the sp^2 graphite network), respectively [12,13].

3.3.2 Hydrophobicity

The water vapor adsorption–desorption isotherms at 25 °C measured for the powder samples are shown in Fig. 3-9. The AHPCS heat-treated at 300 and 400 °C generated a type III isotherm [14,15], which showed a weak interaction to water molecule. The maximum amount of the water adsorption ($V_a(\text{H}_2\text{O})$) of these samples was below 2 $\text{cm}^3(\text{STP})\text{g}^{-1}$. The 500 °C-heat treated AHPCS also showed relatively high hydrophobicity, and the $V_a(\text{H}_2\text{O})$ remained at 6.3 $\text{cm}^3(\text{STP})\text{g}^{-1}$.

The $V_a(\text{H}_2\text{O})$ values evaluated for the AHPCS-derived SiCH were much lower than that of highly hydrophilic mesoporous $\gamma\text{-Al}_2\text{O}_3$ (297 $\text{cm}^3(\text{STP})\text{g}^{-1}$) characterized in the section 2.3.1 in Chapter 2.

On the other hand, the 700 °C-heat treated AHPCS presented a type V [14,15] -like isotherm with a large open loop of hysteresis at $p/p_0(\text{H}_2\text{O})$ above 0.3, and the $V_a(\text{H}_2\text{O})$ reached 42.5 $\text{cm}^3(\text{STP})\text{g}^{-1}$. As shown in Fig. 3-7, the thermal decomposition of the organic groups in AHPCS was almost completed at 700 °C, which led to the analyzed hydrophilic character.

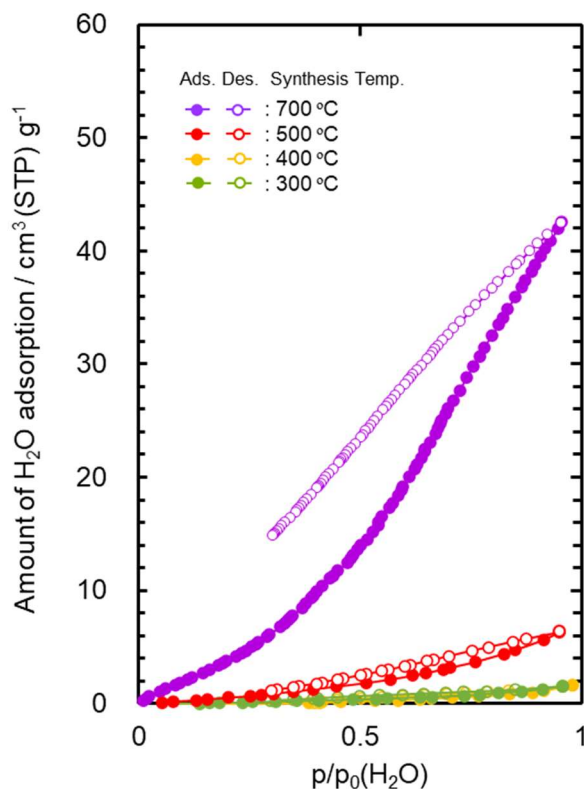


Fig. 3-9. Water vapor adsorption–desorption isotherms at 25 °C for SiCH organic-inorganic hybrid powder samples synthesized by heat treatment of AHPCS at 300–700 °C in Ar.

3.3.3 Properties of SiCH hybrid/ $\gamma\text{-Al}_2\text{O}_3$ composite membrane

(1) Structure of the composite membrane

As a typical observation, Fig. 3-10(a) presents a cross-sectional SEM image of a supported γ - Al_2O_3 membrane after dip coating of the AHPCS xylene solution and subsequent heat treatment at 400 °C under flowing Ar. There was no additional layer on the γ - Al_2O_3 membrane surface. Then, an EDS analysis was performed on the modified membrane. As shown in Fig. 3-10(b), the line scan of the EDS mapping for Si derived from AHPCS was detected within the γ - Al_2O_3 membrane having approximately 2.5 μm thickness. Accordingly, the resulting composite membranes in this study were composed of γ - Al_2O_3 with mesopore channels infiltrated by the AHPCS-derived SiCH hybrid.

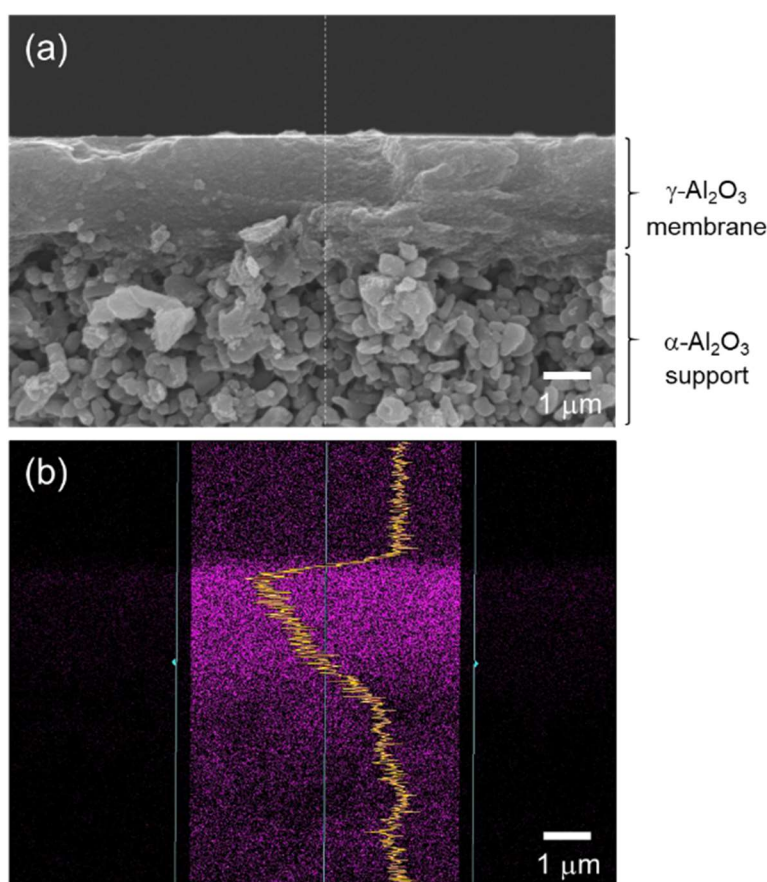


Fig. 3-10. (a) A typical cross-sectional SEM image of the γ - Al_2O_3 membrane on a microporous α - Al_2O_3 support after modification with AHPCS and subsequent heat treatment at 400 °C in Ar. (b) Line scan of EDS mapping for Si derived from AHPCS detected within the mesoporous γ - Al_2O_3 membrane having a thickness of approximately 2.5 μm .

(2) Gas permeation behaviors under dry condition

Arrhenius plots of He, H_2 and N_2 permeances evaluated for the SiCH hybrid/ γ - Al_2O_3 composite membranes synthesized at 300, 400 and 500 °C are shown in Fig. 3-11 (a), (b) and (c), respectively. Despite the low permeation temperature of 25 °C, the composite

membranes exhibited a relatively high H₂ permeance of 1×10^{-7} to 4×10^{-6} mol m⁻² s⁻¹ Pa⁻¹ with a H₂/N₂ permselectivity ($\alpha(\text{H}_2/\text{N}_2)$) of 9.2–17, apparently higher than that of the theoretical one (3.73) based on the Knudsen's diffusion.

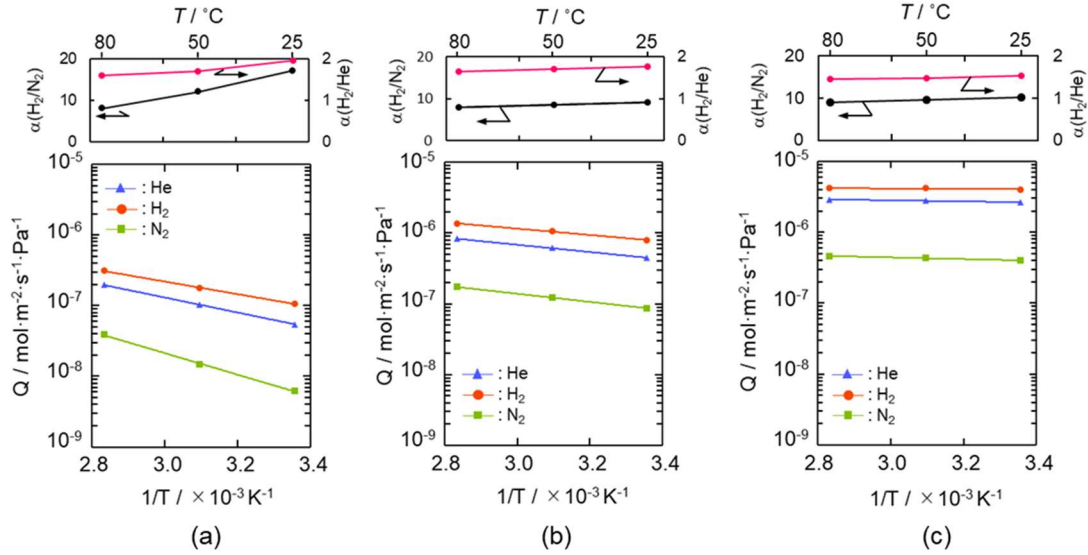


Fig. 3-11. Gas permeation behaviors under dry condition of the supported mesoporous $\gamma\text{-Al}_2\text{O}_3$ membrane after modification with AHPCS and subsequent heat treatment under flowing Ar at (a) 300 °C, (b) 400 °C and (c) 500 °C.

The gas permeation behavior through each composite membrane was similar, and all the gas permeances increased linearly with the permeation temperature and thus followed the Arrhenius law. Since the gas permeations through the supported mesoporous $\gamma\text{-Al}_2\text{O}_3$ membrane exhibited a typical Knudsen's diffusion characteristics described in the section 2.3.3.1 of Chapter 2, the gas permeation behaviors observed for the present composite membranes suggested that all the gases permeated through the microporous SiCH hybrid, which filled in the mesopore channels of the $\gamma\text{-Al}_2\text{O}_3$, and the dominant mechanism for the gas permeations was activated diffusion. However, at all permeation temperatures from 25 to 80 °C, the composite membranes exhibited a unique $\alpha(\text{H}_2/\text{He})$ of 1.44–1.95, which was higher than the theoretical one (1.41) based on the Knudsen's diffusion.

To highlight this unique gas permeation behavior, the gas permeances measured at 50 °C were characterized and are shown in Fig. 3-12 by plotting the kinetic diameter dependence of the normalized gas (*i*) permeance relative to the He permeance (Q_i/Q_{He}), and compared with the ideal value ($Q_{K,i}/Q_{K,\text{He}}$) by the Knudsen model [16,17],

$$\frac{Q_{K,i}}{Q_{K,\text{He}}} = \frac{\sqrt{M_{\text{He}}}}{\sqrt{M_i}} \quad (3-3)$$

where M_i and M_{He} are molecular weights of gas-*i* and He, respectively.

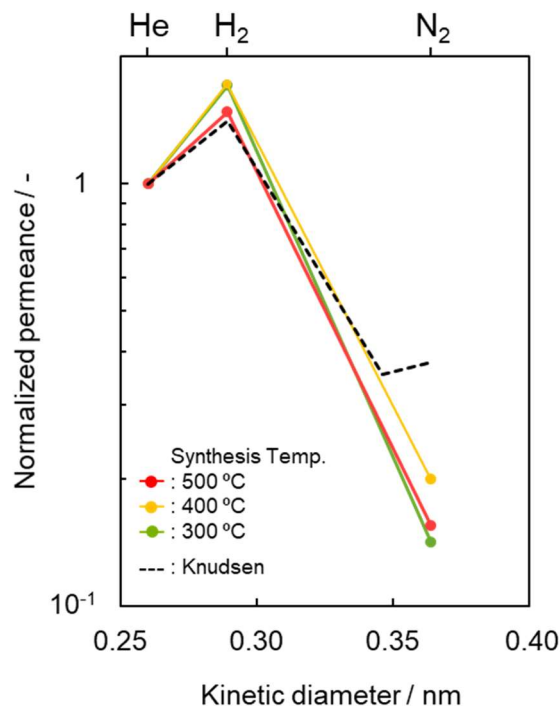


Fig. 3-12. Kinetic diameter dependence of normalized gas permeance based on He permeance (Q_i/Q_{He}) at 50 °C through the SiCH hybrid/ γ - Al_2O_3 composite membrane synthesized at different temperatures of 300, 400 and 500 °C. Dotted line indicates predicted values by the Knudsen diffusion model based on He permeance.

The apparent activation energies for He and H_2 permeations were evaluated by the Arrhenius plot (Fig. 3-11) and are listed in Table 3-1. The apparent activation energy (E_a) for He permeation was 20.3–1.4 kJ mol^{-1} , while that for H_2 permeation was 17.0–0.5 kJ mol^{-1} .

Table 3-1. Activation energies for He and H_2 permeations through the supported mesoporous γ - Al_2O_3 membrane after modification with AHPCS and subsequent heat treatment at 300–500 °C.

SiCH Hybrid/ γ - Al_2O_3 Composite Membrane Synthesis Temp.	Activation Energy (E_a) / kJ mol^{-1}	
	He	H_2
300 °C	20.3	17.0
400 °C	9.8	8.6
500 °C	1.4	0.5

The E_a values for both He and H₂ permeations decreased with the composite membrane synthesis temperature. This tendency was well consistent with the result of TG-MS analyses (Figs. 3-5 and 3-6) and the gas permeation behaviors (Fig. 3-11): weight loss due to the volatilization of the low molecular weight fraction of as-received AHPCS contentiously proceeded at 300–500 °C (Fig. 3-6), and resulting yields of the SiCH hybrid at 300, 400 and 500 °C were measured to be 87, 83 and 76%, respectively (Fig. 3-5), while all the gas permeances through the composite membrane increased with the synthesis temperature (Fig. 3-11). Thus, the observed E_a values for He and H₂ permeations could depend on the density of the AHPCS-derived SiCH-based organic-inorganic hybrid network. However, a unique point was that, regardless of the synthesis temperature, the E_a for H₂ permeation was found to be smaller than that for He permeation, which was a clear contrast to those evaluated for the H₂-selective microporous amorphous silica membranes [18–22]. Then, an attempt was made for study on the hydrogen affinity of the AHPCS-derived SiCH-based organic-inorganic hybrid: The amount of H₂ adsorption on the AHPCS-derived SiCH film was measured by using a quartz-crystal microbalance (QCM). The SiCH sample film was formed on the quartz crystal unit surface by following the procedure for the composite membrane synthesis at 300 °C (effective film area corresponded to A_e in Eq. (3-2), $3.93 \times 10^{-5} \text{ m}^2$). The sample film was exposed to He atmosphere under the strictly regulated isothermal condition at 30 °C (± 0.1 °C) for more than 90 ks. After the He adsorption reached equilibrium, weight gain was monitored by exposing the sample film to H₂ atmosphere under the same isothermal condition. As shown in Fig. 3-13, the weight gain increased with H₂ exposure time and reached 7.14 ng ($1.82 \times 10^{-4} \text{ g m}^{-2}$) after the additional 88,130 s. Since the molecular weight of H₂ (2.016) was approximately one-half of He (4.002), the weight gain measured under the H₂ atmosphere revealed preferential adsorption of H₂ relative to He, *i.e.*, existence of H₂ affinity of the AHPCS-derived SiCH organic-inorganic hybrid, which might contribute to the experimentally observed unique $\alpha(\text{H}_2/\text{He}) > 1.41$ and high H₂ permeances (10^{-7} – $10^{-6} \text{ mol m}^{-2} \text{ s}^{-1} \text{ Pa}^{-1}$ order at 25–80 °C).

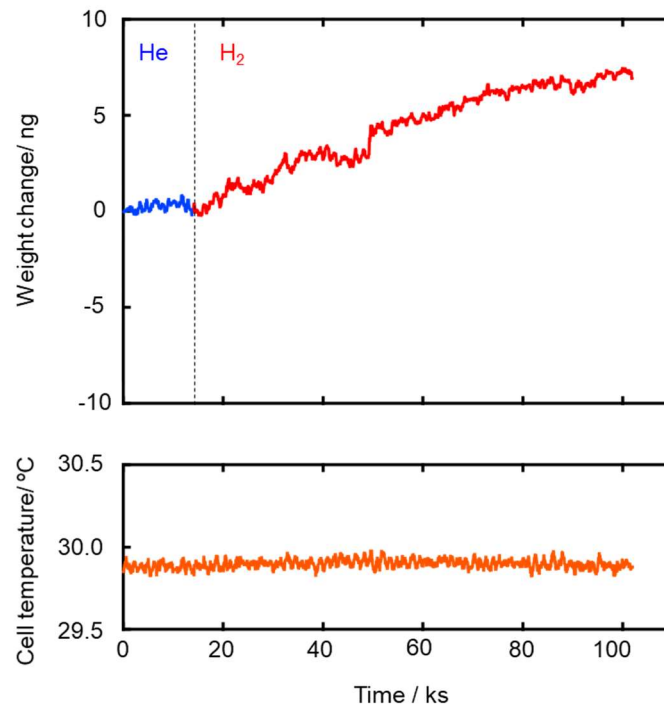


Fig. 3-13. Weight gain measured at 30 °C for H₂ adsorption to the sample film of the SiCH-based organic-inorganic hybrid prepared by 300 °C-heat treatment in Ar.

(3) Gas permeation behaviors under the wet condition

For study on the potential application to the solar hydrogen production system, the gas permeation measurement was performed on the composite membranes by using a mixed H₂-N₂ feed gas in the molar ratio 2:1 under dry and saturated water vapor partial pressure (p/p_0 (H₂O) = 1) at 50 °C. The results are summarized and shown in Fig. 3-14. The composite membranes were found to be water vapor permeable and the permeance was measured to be $2.7\text{--}3.8 \times 10^{-7} \text{ mol m}^{-2} \text{ s}^{-1} \text{ Pa}^{-1}$.

The $\alpha(\text{H}_2/\text{N}_2)$ of the composite membranes was 6.0–11.3, and regardless of the synthesis temperature, there was no significant degradation under the highly humid condition at 50 °C. The 300 °C-synthesized composite membrane kept relatively high gas permeances. The retentions evaluated for the H₂ and N₂ permeances under the p/p_0 (H₂O) = 1 at 50 °C were 69 and 67%, respectively. However, with increasing synthesis temperature, the permeance retention of both H₂ and N₂ decreased, in other words, the hydrophobicity in terms of stable gas permeation property degraded with the synthesis temperature. This degradation tendency is consistent with the temperature dependence of the SiCH hybrid polymer/highly cross-linked SiCH hybrid conversion yield as described above, and thus is related to the quantity of organic groups remained in the SiCH hybrid and the microporosity or volume of the SiCH hybrid, which infiltrated the mesopore channels of the composite membrane.

Then, the 500 °C-synthesized composite membrane was further modified with polycarbosilane (PCS) by the 120 °C-melt impregnation established by our previous study shown in Chapter 2. As shown in Fig. 3-14, under the dry condition at 50 °C, the PCS-modified composite membrane showed a relatively high H₂ permeance of $8.4 \times 10^{-7} \text{ mol m}^{-2} \text{ s}^{-1} \text{ Pa}^{-1}$ with a significantly improved $\alpha(\text{H}_2/\text{N}_2)$ of 29.6. Moreover, under the $p/p_0(\text{H}_2\text{O}) = 1$ at 50 °C, the PCS-modification successfully improved the membrane performance: H₂ permeance and $\alpha(\text{H}_2/\text{N}_2)$ were measured to be $3.5 \times 10^{-7} \text{ mol m}^{-2} \text{ s}^{-1} \text{ Pa}^{-1}$ and 36, respectively.

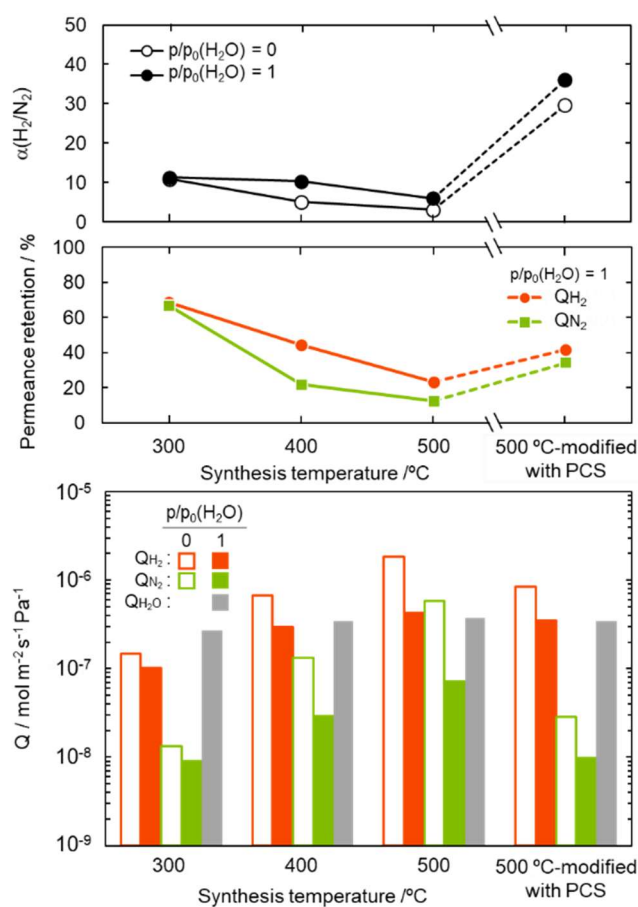


Fig. 3-14. Gas permeation properties under the dry ($p/p_0(\text{H}_2\text{O}) = 0$) and wet ($p/p_0(\text{H}_2\text{O}) = 1$) condition at 50 °C, and water vapor permeation properties at $p/p_0(\text{H}_2\text{O}) = 1$ at 50 °C evaluated for SiCH hybrid/ $\gamma\text{-Al}_2\text{O}_3$ composite membranes synthesized at different temperatures of 300, 400 and 500 °C, and the 500 °C-synthesized membrane further modified with PCS by the melt impregnation at 120 °C.

Gas permeation properties under the wet condition at 50 °C of the composite membranes were also assessed by cyclic gas permeance measurements under $p/p_0(\text{H}_2\text{O})$ ranging from 0.1 to 1.0 and compared with those of the supported mesoporous $\gamma\text{-Al}_2\text{O}_3$ membrane itself. As shown in Fig. 3-15(a), H₂ and N₂ permeances through the supported

mesoporous $\gamma\text{-Al}_2\text{O}_3$ membrane drastically decreased above $p/p_0(\text{H}_2\text{O}) = 0.74$. This degradation is due to the highly hydrophilic property of $\gamma\text{-Al}_2\text{O}_3$, which leads to the blockage of the gas permeable mesopore channels by adsorption and subsequent condensation of water molecules as the permeate (as discussed in Chapter 2). On the other hand, the 300 °C-synthesized composite membrane exhibited stable gas permeations at all the $p/p_0(\text{H}_2\text{O})$ up to 1.0 (Fig. 3-15(b)). A slight decrease in the gas permeances at $p/p_0(\text{H}_2\text{O}) > 0.74$ was due to the pressure-drop caused by the water vapor condensation within the mesopore channels of hydrophilic $\gamma\text{-Al}_2\text{O}_3$ partly remained without surface modification with the AHPCS-derived hydrophobic hybrid. The 500 °C-synthesized composite membrane also showed the decreasing tendency in gas permeances, however further modification with PCS successfully improved the membrane performance at the final gas permeation measurement under the saturated humidity at 50 °C: H_2 permeance remained at 10^{-7} mol m^{-2} s^{-1} Pa^{-1} order with $\alpha(\text{H}_2/\text{N}_2) > 30$ under (Fig. 3-15(c)), and the resulting separation factor (SF) evaluated based on the gas permeation data shown in Table 3-2 was found as 26.

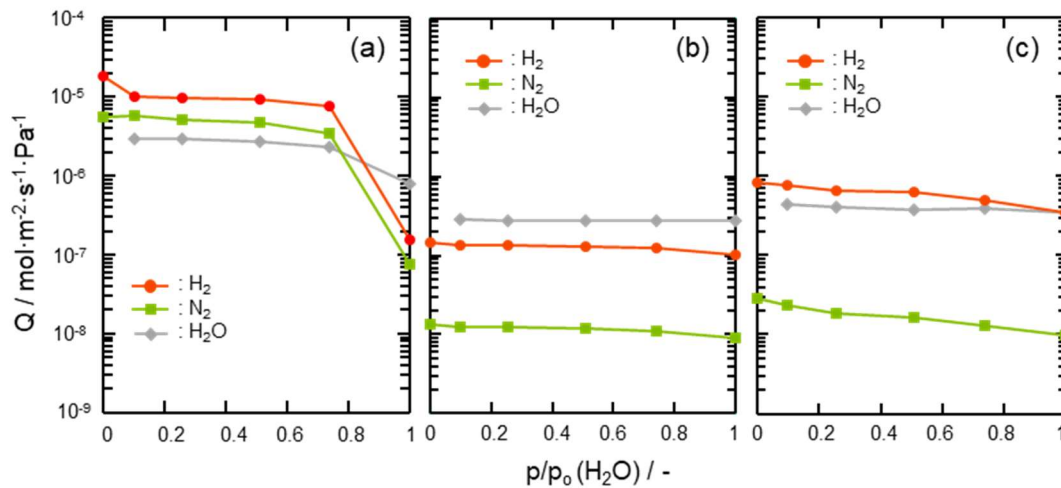


Fig. 3-15. Results of cyclic gas permeation measurements at 50 °C under $p/p_0(\text{H}_2\text{O}) = 0\text{--}1.0$ using the $\text{H}_2\text{-N}_2$ (2:1) mixed feed gas evaluated for (a) a supported mesoporous $\gamma\text{-Al}_2\text{O}_3$ membrane, (b) a 300 °C-synthesized SiCH hybrid/ $\gamma\text{-Al}_2\text{O}_3$ composite membrane and (c) a 500 °C-synthesized composite membrane further modified with PCS.

Table 3-2. Gas permeation data of 500 °C-synthesized membrane further modified with PCS measured at 50 °C under $p/p_0(\text{H}_2\text{O}) = 1.0$ using a $\text{H}_2\text{-N}_2$ (2:1) mixed feed gas.

Feed Side		Permeate Side				Separation Factor (SF)
Flow Rate, $V_F / \times 10^{-5}$ mol s^{-1}		Flow Rate, $V / \times 10^{-5}$ mol s^{-1}		Flux, $J / \times 10^{-5}$ mol m^{-2} s^{-1}		
V_{F, H_2}	V_{F, N_2}	V_{H_2}	V_{N_2}	J_{H_2}	J_{N_2}	
14.7	7.4	2.2	0.043	2971.8	56.6	26

Moreover, the polymer-derived SiCH-based organic-inorganic hybrid investigated in this study showed sufficient stability under the present high humidity conditions at 50 °C: Fig. 3-16 presents the top surface view of the 500 °C-synthesized composite membrane modified with PCS before and after the cyclic gas permeation measurements under $p/p_0(\text{H}_2\text{O})$ up to 1.0 at 50 °C. Compared with the surface of the as-synthesized mesoporous $\gamma\text{-Al}_2\text{O}_3$ membrane over an $\alpha\text{-Al}_2\text{O}_3$ porous support (Fig. 3-16(a)), the composite membrane exhibited a smooth surface (Fig. 3-16(b)) and kept the surface without structural degradation after the cyclic gas permeation measurements (Fig. 3-16(c)). These results revealed that, in addition to hydrogen permselectivity, the modification with the polymer-derived SiCH-based organic-inorganic hybrid investigated in this study greatly improved the hydrophobicity in terms of stable gas permeations under the saturated water vapor partial pressure at 50 °C.

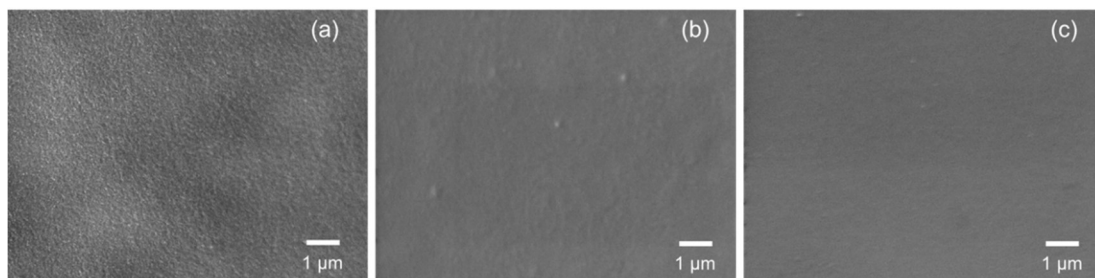


Fig. 3-16. SEM images of the top surface view of an (a) as-synthesized mesoporous $\gamma\text{-Al}_2\text{O}_3$ layer and 500 °C-synthesized membrane further modified with PCS (b) before and (c) after gas permeation measurements under $p/p_0(\text{H}_2\text{O})$ up to 1 at 50 °C.

The H_2 -permselectivities of the composite membrane measured in this study were briefly compared with those recently reported for other membranes composed of various materials systems, and their H_2 permeation data with $\alpha(\text{H}_2/\text{X})$ ($\text{X} = \text{N}_2$ (0.364 nm) [3] or O_2 (0.346 nm) [3]) measured under the dry condition at $T \leq 50$ °C are listed in Table 3-3 [23–34].

Among them, novel ultrathin (9 nm thickness) graphene oxide membrane formed on an anodic oxidized alumina support (#09) exhibited a H_2 permeance of approximately $1 \times 10^{-7} \text{ mol m}^{-2} \text{ s}^{-1} \text{ Pa}^{-1}$ with $\alpha(\text{H}_2/\text{N}_2)$ of 900 at 20 °C [33,34]. The zeolite imidazolate framework (ZIF) nanosheet membrane (#08) also showed H_2 permeance of $2.04 \times 10^{-7} \text{ mol m}^{-2} \text{ s}^{-1} \text{ Pa}^{-1}$ with high $\alpha(\text{H}_2/\text{N}_2)$ of 66.6 at 30 °C [31,32]. Among other practical membranes, SiO_2 -based organic-inorganic hybrid membrane (#03) showed the highest H_2 permeance of $10^{-6} \text{ mol m}^{-2} \text{ s}^{-1} \text{ Pa}^{-1}$ order, while the $\alpha(\text{H}_2/\text{N}_2)$ remained at 12 [24]. On the other hand, zeolite/CMC (carbon molecular sieve) composite membranes (#04, #05) showed a high $\alpha(\text{H}_2/\text{N}_2)$ of 61-100.2, however the H_2 permeance at 30 °C was 10^{-9} – $10^{-8} \text{ mol m}^{-2} \text{ s}^{-1} \text{ Pa}^{-1}$ order [27,28].

As shown in Figs. 3-11 and 3-12, in addition to the H₂/N₂ selectivity, the present composite membranes exhibited unique H₂/He selectivity due to the H₂ affinity of the AHPCS-derived highly cross-linked SiCH-based organic-inorganic hybrid in the composite membrane (Fig. 3-13). This unique H₂ preferential permeation property contributed to relatively high H₂ permeance of 8.4×10^{-7} mol m⁻² s⁻¹ Pa⁻¹ with $\alpha(\text{H}_2/\text{N}_2)$ of 29.6.

Table 3-3. H₂-permselectivities of composite membrane in this study and those of other membranes evaluated at $T \leq 50$ °C under the dry condition.

No.	Membranes	Temp./°C	H ₂ Permeance /mol m ⁻² s ⁻¹ Pa ⁻¹	H ₂ /X Selectivity		Ref.
				$\alpha(\text{H}_2/\text{X})$	X	
#01	500 °C modified with PCS, Dry Wet, p/p ₀ (H ₂ O) = 1.0	50	8.4×10^{-7}	29.6	N ₂	This study
		50	3.5×10^{-7}	36.1	N ₂	
#02	SiO ₂ -based organic-inorganic hybrid (BTESE)	40	7.66×10^{-7}	~ 20	N ₂	[24]
#03	SiO ₂ -based organic-inorganic hybrid (BTESM)	50	1.79×10^{-6}	12	N ₂	
#04	zeolite-β/CMS	30	2.64×10^{-9}	97	N ₂	[27][28]
		30	1.95×10^{-8}	67.3	N ₂	
#05	zeolite-Y/CMS	30	2.77×10^{-9}	100.2	N ₂	
		30	1.96×10^{-8}	61	N ₂	
#06	PFDA-based liquid membrane	30	2.4×10^{-9}	10	O ₂	[23]
#07	graphene nanosheet	RT	5.9×10^{-7}	16.5	N ₂	[29][30]
#08	ZIF nanosheet membrane	30	2.04×10^{-7}	66.55	N ₂	[31][32]
#09	ultrathin graphene oxide	20	$\sim 1 \times 10^{-7}$	~ 900	N ₂	[33][34]
#10	microporous polymer (PIM-EA(H ₂)-TB)	30	$(1.7 \times 10^{-12})^*$	22	N ₂	[25]
#11	microporous polymer (PIM-Trip(Me ₂)-TB)	25	$(1.8 \times 10^{-12})^*$	21.4	N ₂	[26]

*: H₂ permeability/mol m⁻¹ s⁻¹ Pa⁻¹.

The H₂-permeance and H₂/N₂ selectivity evaluated under dry and saturated humidity at 50 °C of the present composite membrane samples and those reported for other membranes evaluated at $T \leq 50$ °C under dry are compared and plotted in Fig. 3-17. Under dry condition, the performance of the present composite membrane is located on the “upper limit line” recognized for those of other reported membranes. However, even under the saturated humidity condition at 50 °C, the present composite membrane keep the performance without degradation.

For application to the purification of solar hydrogen, the long-term stability and robustness of H₂-selective membranes under the humid condition at around 50 °C are practical issues for us to pursue. In this context, there are few reports as mentioned above, and Oyama *et al.* reported [23] their pioneering study on the stability of PFDA-based liquid membrane (#06 in Table 3-3) under the humid condition (10 mol%) at 30 °C as a simulated condition for the purification of solar hydrogen, and they confirmed its stability for up to 48 h. The stabilities of the composited membranes characterized by the primary accelerated degradation test (Figs. 3-14, 3-15 and 3-16) were compatible with that of the

supported liquid membrane (#06 in Table 3-3) [23]. Under the scheme of the current NEDO R&D “Artificial Photosynthesis” Project, we plan to conduct the long-term stability test for the composite membranes by using a H₂-O₂ (2:1) mixed feed gas as a simulated syngas at the project facility with safety measures against explosion.

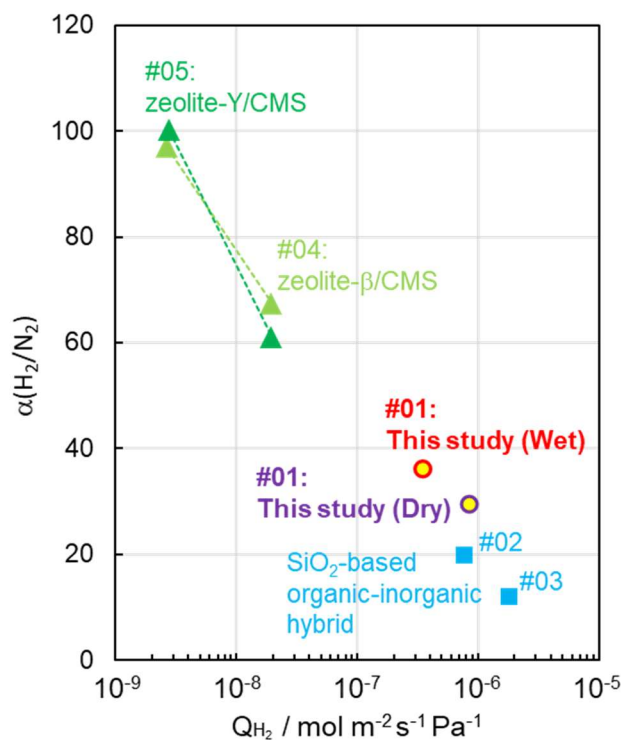


Fig. 3-17. H₂-permeance and H₂/N₂ selectivity evaluated under dry and saturated humidity at 50 °C of the composite membrane samples synthesized in this study and those reported for other membranes evaluated at T ≤ 50 °C under dry condition.

3.4 Summary

In this study, AHPCS was converted to highly cross-linked ternary SiCH-based organic-inorganic hybrid compounds by heat treatment at 300–500 °C under Ar atmosphere. The water vapor adsorption–desorption isotherm measurement revealed that the AHPCS-derived highly cross-linked SiCH hybrids exhibited excellent hydrophobicity, and the maximum amount of water vapor adsorption at 25 °C was 1.5–6.3 cm³ (STP) g⁻¹.

Aiming to develop H₂-selective membranes for the application of the novel solar hydrogen production system, a supported mesoporous γ-Al₂O₃ membrane with a thickness of about 2.5 μm was modified with AHPCS xylene solution and subsequently heat-treated at 300–500 °C under Ar atmosphere. SEM observation revealed that the mesoporous channels of the γ-Al₂O₃ membrane were coated by the AHPCS-derived SiCH to afford a SiCH hybrid/γ-Al₂O₃ composite membrane. Even at a low temperature of 25

°C, the composite membranes exhibited a high H₂ permeance of 1×10^{-7} to 4×10^{-6} mol m⁻² s⁻¹ Pa⁻¹ and a $\alpha(\text{H}_2/\text{N}_2)$ of 9.2–17 together with a unique $\alpha(\text{H}_2/\text{He})$ of 1.44–1.95.

The apparent activation energy for the H₂ permeation at 25–80 °C was 17.0–0.5 kJ mol⁻¹ and found to be smaller than that for He (20.3–1.4 kJ mol⁻¹). Moreover, the measurement of H₂ adsorption on an AHPCS-derived SiCH film by using a QCM revealed preferential H₂ adsorption at 30 °C. These results strongly indicate a significant H₂ affinity of the AHPCS-derived SiCH-based organic-inorganic hybrid, which contributes to the experimentally observed unique $\alpha(\text{H}_2/\text{He})$ and the high H₂ permeance at 25–80 °C.

As a simulated wet condition for the purification of solar hydrogen, the gas permeation measurement under saturated water vapor partial pressure at 50 °C was performed on the composite membranes by using a mixed H₂-N₂ feed gas in the molar ratio 2:1. The 300–500 °C synthesized composite membranes exhibited a relatively high H₂ permeance of $1.0\text{--}4.3 \times 10^{-7}$ mol m⁻² s⁻¹ Pa⁻¹ with a $\alpha(\text{H}_2/\text{N}_2)$ of 6.0–11.3. Further modification by the 120 °C-melt impregnation of PCS successfully improved the H₂-permselectivity of the 500 °C synthesized composite membrane by maintaining the H₂ permeance combination with improved $\alpha(\text{H}_2/\text{N}_2)$ as 3.5×10^{-7} mol m⁻² s⁻¹ Pa⁻¹ and 36. These results clearly revealed a promising potential of polymer-derived SiCH-based organic-inorganic hybrids to develop advanced H₂ selective membranes applicable to novel solar hydrogen production systems.

References

- [1] T. Yamada, K. Domen, Development of Sunlight Driven Water Splitting Devices towards Future Artificial Photosynthetic Industry, *ChemEngineering* 2 (2018) 36.
- [2] Development of Basic Chemical Processes for Carbon Dioxide as Raw Material, *New Energy Ind. Technol. Dev. Organ.* (2014).
https://www.nedo.go.jp/activities/EV_00296.html (accessed August 2, 2020).
- [3] D.W. Breck, *Zeolite Molecular Sieves: Structure, Chemistry, and Use*, John Wiley & Sons, New York, 1974.
- [4] D.A. Buttry, M.D. Ward, Measurement of Interfacial Processes at Electrode Surfaces with the Electrochemical Quartz Crystal Microbalance, *Chem. Rev.* 92 (1992) 1355–1379.
- [5] G. Sauerbrey, Verwendung von Schwingquarzen zur Wägung dünner Schichten und zur Mikrowägung, *Zeitschrift Für Phys.* 155 (1959) 206–222.
- [6] Q. Wang, M. Yokoji, H. Nagasawa, L. Yu, M. Kanezashi, T. Tsuru, Microstructure evolution and enhanced permeation of SiC membranes derived from allylhydridopolycarbosilane, *J. Memb. Sci.* (2020) 118392.
- [7] R. Sreeja, B. Swaminathan, A. Painuly, T. V. Sebastian, S. Packirisamy, Allylhydridopolycarbosilane (AHPCS) as matrix resin for C/SiC ceramic matrix composites, *Mater. Sci. Eng. B Solid-State Mater. Adv. Technol.* 168 (2010) 204–207.
- [8] S. Kaur, R. Riedel, E. Ionescu, Pressureless fabrication of dense monolithic SiC ceramics from a polycarbosilane, *J. Eur. Ceram. Soc.* 34 (2014) 3571–3578.
- [9] Q. Wen, Y. Xu, B. Xu, C. Fasel, O. Guillon, G. Buntkowsky, Z. Yu, R. Riedel, E.

- Ionescu, Single-source-precursor synthesis of dense SiC/HfC_xN_{1-x}-based ultrahigh-temperature ceramic nanocomposites, *Nanoscale* 6 (2014) 13678–13689.
- [10] V. Proust, M.C. Bechelany, R. Ghisleni, M.F. Beaufort, P. Miele, S. Bernard, Polymer-derived Si-C-Ti systems: From titanium nanoparticle-filled polycarbosilanes to dense monolithic multi-phase components with high hardness, *J. Eur. Ceram. Soc.* 36 (2016) 3671–3679.
- [11] M. Schmidt, C. Durif, E.D. Acosta, C. Salameh, H. Plaisantin, P. Miele, R. Backov, R. Machado, C. Gervais, J.G. Alauzun, G. Chollon, S. Bernard, Molecular-Level Processing of Si-(B)-C Materials with Tailored Nano/Microstructures, *Chem. - A Eur. J.* 23 (2017) 17103–17117.
- [12] A.C. Ferrari, J. Robertson, Interpretation of Raman spectra of disordered and amorphous carbon, *Phys. Rev. B.* 61 (2000) 14095–14107.
- [13] M.A. Pimenta, G. Dresselhaus, M.S. Dresselhaus, L.G. Cançado, A. Jorio, R. Saito, Studying disorder in graphite-based systems by Raman spectroscopy, *Phys. Chem. Chem. Phys.* 9 (2007) 1276–1291.
- [14] K.S.W. Sing, D.H. Everett, R.A.W. Haul, L. Moscou, R.A. Pierotti, J. Rouquerol, T. Siemienieska, Reporting physisorption data for gas/solid systems with special reference to the determination of surface area and porosity, *Pure Appl. Chem.* 57 (1985) 603–619.
- [15] S. Lowell, J.E. Shields, M.A. Thomas, M. Thommes, *Characterization of porous solids and powders*, Springer, Netherlands, 2004.
- [16] H.R. Lee, M. Kanezashi, Y. Shimomura, T. Yoshioka, T. Tsuru, Evaluation and fabrication of pore-size-tuned silica membranes with tetraethoxydimethyl disiloxane for gas separation, *AIChE J.* 57 (2011) 2755–2765.
- [17] T. Yoshioka, M. Kanezashi, T. Tsuru, Micropore size estimation on gas separation membranes: A study in experimental and molecular dynamics, *AIChE J.* 59 (2013) 2179–2194.
- [18] Y. Mise, S.J. Ahn, A. Takagaki, R. Kikuchi, S.T. Oyama, Fabrication and evaluation of trimethylmethoxysilane (TMMOS)-derived membranes for gas separation, *Membranes* 9 (2019) 123.
- [19] H. Kato, S.-T.B. Lundin, S.-J. Ahn, A. Takagaki, R. Kikuchi, S.T. Oyama, Gas Separation Silica Membranes Prepared by Chemical Vapor Deposition of Methyl-Substituted Silanes, *Membranes* 9 (2019) 144.
- [20] D. Lee, L. Zhang, S.T. Oyama, S. Niu, R.F. Saraf, Synthesis, characterization, and gas permeation properties of a hydrogen permeable silica membrane supported on porous alumina, *J. Memb. Sci.* 231 (2004) 117–126.
- [21] Y. Gu, S.T. Oyama, High Molecular Permeance in a Poreless Ceramic Membrane, *Adv. Mater.* 19 (2007) 1636–1640.
- [22] S.J. Ahn, G.N. Yun, A. Takagaki, R. Kikuchi, S.T. Oyama, Synthesis and characterization of hydrogen selective silica membranes prepared by chemical vapor deposition of vinyltriethoxysilane, *J. Memb. Sci.* 550 (2018) 1–8.
- [23] T. Yamaguchi, A. Takagaki, T. Sugawara, R. Kikuchi, S.T. Oyama, Supported fluorocarbon liquid membranes for hydrogen/oxygen separation, *J. Memb. Sci.* 520 (2016) 272–280.
- [24] X. Ren, T. Tsuru, Organosilica-based membranes in gas and liquid-phase separation, *Membranes* 9 (2019) 107.

- [25] E. Lasseuguette, R. Malpass-Evans, M. Carta, N.B. McKeown, M.C. Ferrari, Temperature and pressure dependence of gas permeation in a microporous Tröger's base polymer, *Membranes* 8 (2018) 1–11.
- [26] R. Malpass-Evans, I. Rose, A. Fuoco, P. Bernardo, G. Clarizia, N.B. McKeown, J.C. Jansen, M. Carta, Effect of bridgehead methyl substituents on the gas permeability of tröger's-base derived polymers of intrinsic microporosity, *Membranes* 10 (2020) 62.
- [27] L. Li, C. Wang, N. Wang, Y. Cao, T. Wang, The preparation and gas separation properties of zeolite/carbon hybrid membranes, *J. Mater. Sci.* 50 (2015) 2561–2570.
- [28] L. Li, R. Xu, C. Song, B. Zhang, Q. Liu, T. Wang, A review on the progress in nanoparticle/C hybrid CMS membranes for gas separation, *Membranes* 8 (2018) 134.
- [29] R. Zeynali, K. Ghasemzadeh, A.B. Sarand, F. Kheiri, A. Basile, Performance evaluation of graphene oxide (GO) nanocomposite membrane for hydrogen separation: Effect of dip coating sol concentration, *Sep. Purif. Technol.* 200 (2018) 169–176.
- [30] M. Nouri, K. Ghasemzadeh, A. Iulianelli, Theoretical evaluation of graphene membrane performance for hydrogen separation using molecular dynamic simulation, *Membranes* 9 (2019) 110.
- [31] Y. Li, L. Lin, M. Tu, P. Nian, A.J. Howarth, O.K. Farha, J. Qiu, X. Zhang, Growth of ZnO self-converted 2D nanosheet zeolitic imidazolate framework membranes by an ammonia-assisted strategy, *Nano Res.* 11 (2018) 1850–1860.
- [32] M. Fang, C. Montoro, M. Semsarilar, Metal and covalent organic frameworks for membrane applications, *Membranes* 10 (2020) 107.
- [33] H. Li, Z. Song, X. Zhang, Y. Huang, S. Li, Y. Mao, H.J. Ploehn, Y. Bao, M. Yu, Ultrathin, molecular-sieving graphene oxide membranes for selective hydrogen separation, *Science* 342 (2013) 95–98.
- [34] L. Huang, H. Lin, Engineering sub-nanometer channels in two-dimensional materials for membrane gas separation, *Membranes* 8 (2018) 100.

Chapter 4

Superhydrophobic polycarbosilane membranes for purification of solar hydrogen

4.1 Introduction

In Chapter 3, aiming to develop H₂-selective membranes for the application to the novel solar hydrogen production system, the mesoporous channels of the supported γ -Al₂O₃ membrane were filled by allyl-hydro-polycarbosilane (AHPCS) which was heat-treated at 300–500 °C under Ar to afford the AHPCS-derived SiCH-based organic-inorganic hybrid/ γ -Al₂O₃ composite membrane. Under the simulated wet condition for the purification of solar hydrogen, high H₂ permeance combined with improved H₂/N₂ selectivity as $3.5 \times 10^{-7} \text{ mol m}^{-2} \text{ s}^{-1} \text{ Pa}^{-1}$ with 36 was attained for the 500 °C-synthesized composite membrane after further modification by the 120 °C-melt impregnation of low molecular weight polycarbosilane (PCS).

In addition, the measurement of H₂ adsorption on an AHPCS-derived SiCH film by using the quartz crystal microbalance at 30 °C revealed preferential H₂ adsorption which indicating a significant H₂ affinity of the polymer-derived SiCH-based organic-inorganic hybrid. Moreover, the composite membrane exhibited a unique preferential H₂ permeation compared to that of He, smallest gas molecule. However, the dominant gas permeation mechanisms through the composite membrane as well as the preferential H₂ permeation observed for the polymer-derived SiCH-hybrid/ γ -Al₂O₃ composite membranes have not yet been clarified theoretically.

In this chapter, a layered composite membrane composed of SiCH hybrid membrane supported on the mesoporous γ -Al₂O₃ layer was attempted to fabricate to clarify the intrinsic gas permeation properties of the SiCH-hybrid membrane itself. This study was firstly dedicated to the characterization of the hydrophobicity of supported PCS membranes in terms of stable gas permeations and unique preferential H₂ permeation under high humidity conditions at low-temperatures around 50 °C. By using high molecular weight PCSs having melting point above 200 °C, we showed that a superhydrophobic PCS membrane could be deposited on a mesoporous γ -Al₂O₃-modified macroporous α -Al₂O₃ tubular support. Then, gas permeation properties of the supported PCS membrane were characterized by measuring single gas permeances of helium (He), hydrogen (H₂) and nitrogen (N₂) under dry condition at 25 to 80 °C. Finally, the H₂-permselectivity was evaluated under water vapor partial pressures ranging from 0.1 to 1 at 50 °C and compared with those of a conventional sol gel-derived SiO₂ membrane. Possible mechanisms for gas permeations through the supported PCS membranes were discussed based on the gas permeation behaviors with unique H₂/He selectivity under dry condition up to 200 °C, improved H₂/N₂ selectivity under the high-humidity conditions at 50 °C and significantly high hydrophobicity of the PCSs characterized by measuring water vapor adsorption-desorption isotherms at 25 °C. Moreover, excellent H₂-selectivity

under saturated humidity at 50 °C of the supported PCS membrane was demonstrated by using a H₂-N₂ (2:1) mixed feed gas as a simulated syngas produced by the novel solar hydrogen production via the PEC water-splitting reaction.

4.2 Experimental Procedures

4.2.1 Synthesis of PCS membranes

In this study, commercially available PCSs (Type A, UH and UUH, Artkagaku Co., Ltd., Ibaragi, Japan) were used as received. Table 4-1 listed melting point (m.p.) and chemical composition of the PCSs provided by the supplier [1]. As shown in Table 4-1 and Fig. 4-1, gel permeation chromatography (GPC) analysis at our laboratory revealed that the number average molecular weight (M_n) and the mean molecular weight (M_w) of PCS(UUH) were apparently higher than those of PCS(UH), which suggested that the m.p. of PCS(UUH) could be above 350 °C and/or no definite temperature as reported by the supplier [1].

Table 4-1. Properties of PCSs.

PCS Type	M _n / -	M _w / -	M _w /M _n	m. p. /°C [1]	Chemical composition / wt% [1]				
					Si	C	H	O	N
A	1318	4042	3.07	230	50	40	8.1	0.5	0.7
UH	1668	5920	3.55	350*	50	40	8.2	1.4	1.7
UUH	4183	8933	2.14	-	n.d.	n.d.	n.d.	n.d.	n.d.

*Partial melting

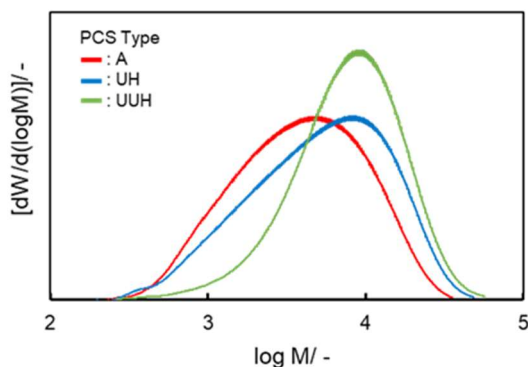


Fig. 4-1. Molecular weight distribution of as-received PCSs used for the membrane syntheses in this study.

A commercially available α -Al₂O₃ tubular support (6 mm outer diameter, 4 mm inner diameter and 60 mm length, total porosity of 40 %, Noritake Co., Ltd., Aichi, Japan) was used. This α -Al₂O₃ tubular support consisted of a core with a mean pore diameter (d_{core}) of 700 nm and a rim with a d_{rim} of 150 nm.

A mesoporous γ -Al₂O₃ layer with a thickness of about 3.5 μ m was fabricated on the outer surface of the macroporous α -Al₂O₃ tubular support by following reported procedures [2,3].

For PCS membrane synthesis, 1 wt% solution of as-received PCS/dry xylene (super dehydrated grade, 99.5 % purity, Wako Pure Chemical Co., Ltd., Osaka, Japan) was prepared for each type shown in Table 1. The PCS solution was dip-coated on the mesoporous γ -Al₂O₃ layer placed on the outer surface of the macroporous α -Al₂O₃ tubular support according to the procedures established by our previous study in Chapter 2. Then, the solvent (xylene) was removed from the PCS-coated layer by heat treatment at 120 °C to afford a PCS membrane supported on the mesoporous γ -Al₂O₃ layer placed on the outer surface of the macroporous α -Al₂O₃ tubular support (Hereafter, the supported PCS membrane was labeled as PCS(X), where X denoted type of PCS).

4.2.2 Characterizations

GPC measurement for as-received PCSs was performed on a Shodex GPC-104 system (Showa Denko K.K., Tokyo, Japan) equipped with two tandem columns (Shodex LF-404, Showa Denko K.K., Tokyo, Japan) calibrated against standard polystyrenes and with a Shodex RI-74S detector (Showa Denko K.K., Tokyo, Japan) using tetrahydrofuran (THF) as eluent with a flow rate of 1.0 mL min⁻¹ at 40 °C.

Water vapor adsorption-desorption isotherms of the powder samples were measured at 25 °C (Model BELSORP-aqua 3, MicrotracBEL Corp., Osaka, Japan). The powder samples of the as-received PCSs were prepared by solvent removal from the PCS(X) coating solution described above at 50 °C under vacuum followed by heat treatment at 120 °C for 1h. As a reference sample, the measurement was also performed on a SiO₂ powder prepared by drying SiO₂ sol coating solution at 60 °C for 1 h followed by heat treatment at 600 °C in air. The SiO₂ sol coating solution was prepared as follows: A mixture of 8.93 mL of tetraethoxysilane (99 %, Kishida Chemical Co., Ltd., Osaka, Japan) and 8.86 mL of ethanol (99.5 %, Kishida Chemical Co., Ltd., Osaka, Japan) was stirred, then peptized with a nitric acid aqueous solution of 0.357 g of HNO₃ (60.0-61.0 %, Kishida Chemical Co., Ltd., Osaka, Japan) and 4.465 g of distilled water for 15 min. The peptized mixture was refluxed at 80 °C for 3 h. After cooling down to room temperature, the reaction mixture was diluted with 110.57 g of ethanol to give a SiO₂ sol coating solution for SiO₂ membrane synthesis.

Cross-sectional structure of the PCS membrane supported on the mesoporous γ -Al₂O₃ layer was observed by a scanning electron microscope (SEM, Model JSM-6360LV, JEOL Ltd., Tokyo, Japan) and examined by the energy dispersive X-ray spectroscopic (EDS) analysis (Model JSM-6010LA mounted on SEM, JEOL Ltd., Tokyo, Japan).

Single gas permeances through the supported PCS membranes were measured by the volumetric method at constant pressure. Single gas permeances under dry condition at 25-80 °C were measured in order of a kinetic diameter for He (0.26 nm), H₂ (0.289 nm) and N₂ (0.364 nm) [4]. As for the PCS(UH), the single gas permeances were measured at temperatures up to 200 °C.

Under wet condition, single gas permeances through the PCS(A) were measured at the water partial vapor pressures (p/p_0 (H_2O)) ranging from 0.1 to 1 at 50 °C. As a reference, the same measurements were performed on a sol gel-derived SiO_2 membrane fabricated as follows: The SiO_2 sol coating solution described above was dip-coated on the outer surface of the mesoporous $\gamma\text{-Al}_2\text{O}_3$ -modified $\alpha\text{-Al}_2\text{O}_3$ macroporous tubular support under the same manner as mentioned for the supported PCS membrane synthesis, then dried at 60 °C and subsequently heat-treated at 600 °C for 1 h. This dip coating-drying-heating process was repeated 5 times.

As for the PCS(A), gas permeances were also measured using a mixed feed gas with a 2:1 molar ratio of H_2 and N_2 as a simulated syngas produced by the solar hydrogen production via the PEC water-splitting reaction.

The details of the procedures and the equipment setup for the gas permeation measurements have been reported in Chapter 1 (1.5.1). Single gas permeance of gas- i (Q_i) was calculated using Eq. (1-35). The pressure difference ($p_H - p_L$) in Eq. (1-35) was fixed as 100 kPa in this study.

Permselectivity was defined as the ratio of single gas permeances measured for the two kind of gases, for instance, the H_2/N_2 permselectivity ($\alpha(\text{H}_2/\text{N}_2)$) was evaluated as the ratio $Q_{\text{H}_2}/Q_{\text{N}_2}$.

When the gas permeances were evaluated using a $\text{H}_2\text{-N}_2$ (2 : 1) mixed feed gas, the permeate gas composition was determined by using a gas chromatograph (GC, Model CP-4900 Micro-GC, Varian medical systems Inc., CA, USA) and Ar sweep gas (50 mL min^{-1}). Each gas permeance of Q_{H_2} and Q_{N_2} was evaluated by using the analyzed composition and the measured permeate molar flow rate described in the section 3.2.3 in Chapter 3. The water vapor permeance was evaluated using a gas chromatograph for polar gas analysis (GC323, GL Sciences Inc., Tokyo, Japan) according to the procedures shown in the section 3.2.3 in Chapter 3.

4.3 Results and Discussion

4.3.1 Hydrophobicity of as-received PCSs

A significantly high hydrophobicity of as-received PCSs was characterized by measuring water vapor adsorption-desorption isotherms at 25 °C of powder samples (Fig. 4-2(a)). Compared with the mesoporous $\gamma\text{-Al}_2\text{O}_3$ (evaluated and shown in Chapter 2) which generated a type IV-like isotherm (Fig. 2-4 in the section 2.3.1), all the three types of PCSs showed a significantly low water vapor adsorption uptake and a type III isotherm, showing weak interactions between adsorbent and adsorbate. On the other hand, a reference sample, sol gel-derived SiO_2 generated a type I [5,6] -like isotherm. The slight water vapor adsorption uptake below 0.1 of $p/p_0(\text{H}_2\text{O})$ was related to capillary condensation within the micropores [5,6]. As shown in Fig. 4-2(b), the maximum amount of water vapor adsorption ($V_a(\text{H}_2\text{O})$) of the PCSs was below 4 $\text{cm}^3(\text{STP})\text{g}^{-1}$, which was much lower than those of $\gamma\text{-Al}_2\text{O}_3$ (297 $\text{cm}^3(\text{STP})\text{g}^{-1}$, evaluated and shown in Chapter 2) and the sol gel-derived SiO_2 (39.5 $\text{cm}^3(\text{STP})\text{g}^{-1}$).

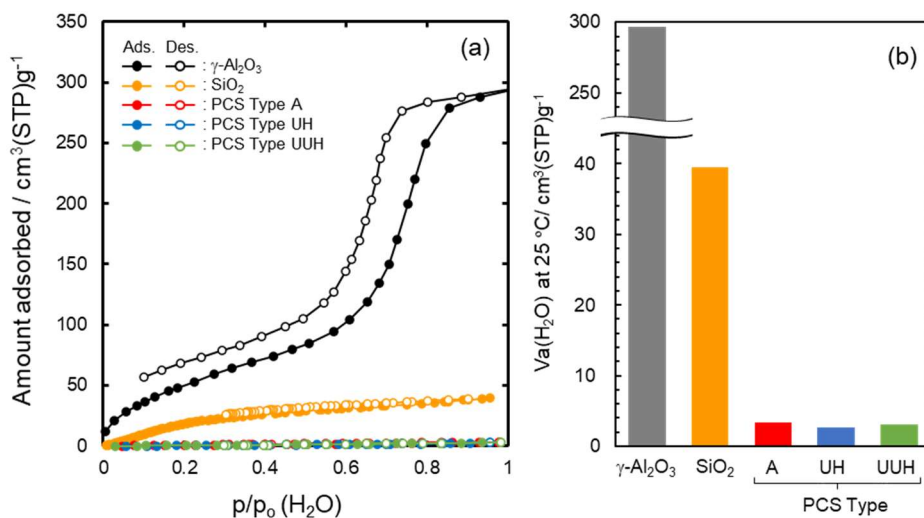


Fig. 4-2. Water vapor adsorption-desorption isotherms at 25 °C for (a) as-received PCSs, sol gel-derived SiO₂ and mesoporous γ -Al₂O₃. (b) Maximum amount of water vapor adsorption (Va(H₂O)) at 25 °C of the PCSs in comparison with those of sol gel-derived SiO₂ and mesoporous γ -Al₂O₃.

To examine the significantly high hydrophobic character of the PCSs in more details, FT-IR spectroscopic analysis was performed on the PCS powder samples (Fig. 4-3). The spectra of these samples presented common absorption peaks at 2950-2900 cm⁻¹ (ν C-H), 2100 cm⁻¹ (ν Si-H), 1450-1350 cm⁻¹ (ν C-H in CH_x (x=1-3)), 1250 cm⁻¹ (ν Si-CH₃), 1020 cm⁻¹ (γ CH₂ in Si-CH₂-Si) and around 800 cm⁻¹ (γ Si-CH₃ and ν Si-H in SiC₄) [7,8].

As expanded and shown in Fig. 4-3, these samples exhibited a weak broad peak around 3400 cm⁻¹ attributed to intermolecular hydrogen-bonded silanol (Si-OH) group and adsorbed water molecules, while the sharp peak centered at 3674 cm⁻¹ correspond to free Si-OH group [8]. As discussed previously in Chapter 2 [9,10], the polar Si-OH group acted as a preferential adsorption site for water molecules. Then, density of the free Si-OH group in each sample was evaluated by measuring the relative ratio of the FT-IR absorption peak intensities: I(Si-OH) at 3674 cm⁻¹/I(Si-CH₂-Si) at 1020 cm⁻¹. It was found to be as low as 0.02-0.04. Accordingly, in addition to the hydrophobic CH₃ groups attached to the Si-C backbone [8], extremely low density of the free Si-OH group lead to the superhydrophobicity of the PCSs characterized in this study.

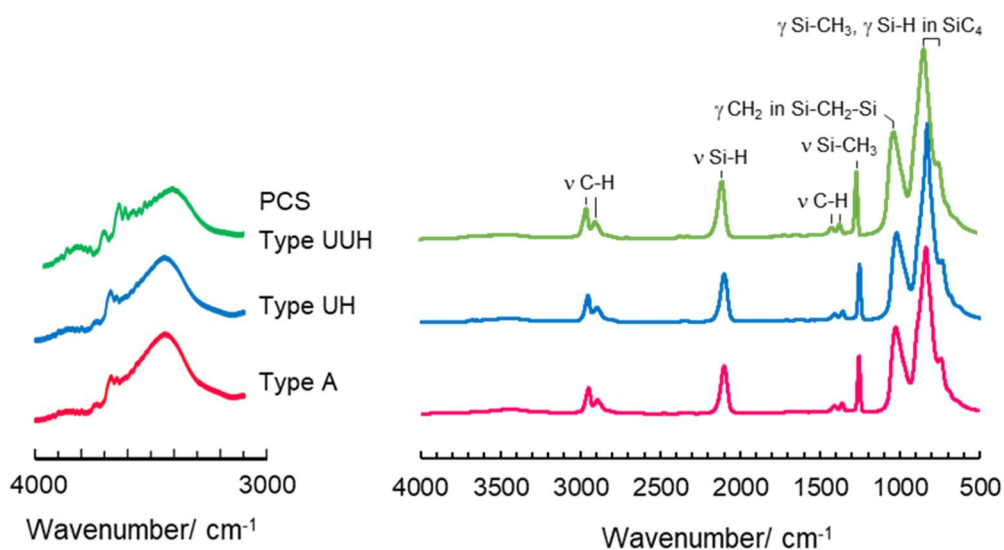


Fig. 4-3. FT-IR spectra for as-received PCSs investigated in this study.

4.3.2 Properties of supported PCS membranes

(1) Structure of PCS membranes

To confirm membrane formation of the PCS over the mesoporous γ - Al_2O_3 layer placed on a macroporous α - Al_2O_3 tubular support, SEM was performed through the observation of the cross-sectional SEM image of the alumina tubes functionalized by the PCS(UH) sample (Fig. 4-4). As a typical result, a thin dense layer with a uniform thickness of approximately 50 nm was observed on the outer surface of the mesoporous γ - Al_2O_3 layer which corresponds to the PCS(UH) membranes.

According to the EDS analysis for the cross-section (Fig. 4-5), Si and C elements present in PCS were also detected within the mesoporous γ - Al_2O_3 layer, and it was suggested that some part of the coated PCS infiltrated the γ - Al_2O_3 mesopore channels, but located discontinuously.

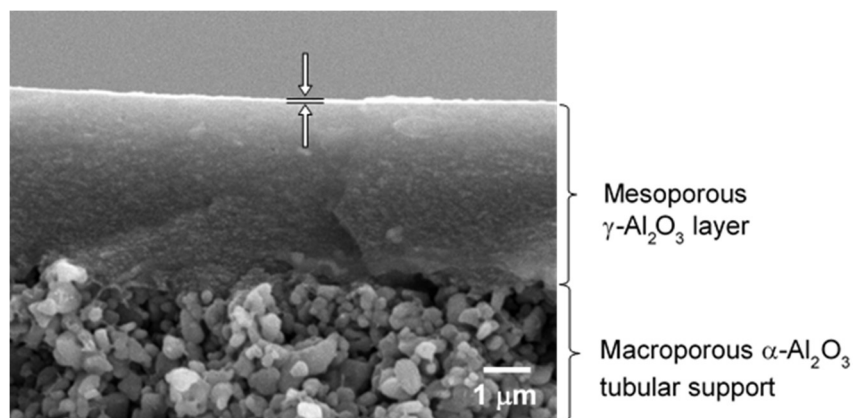


Fig. 4-4. A cross-sectional SEM image of PCS(UH).

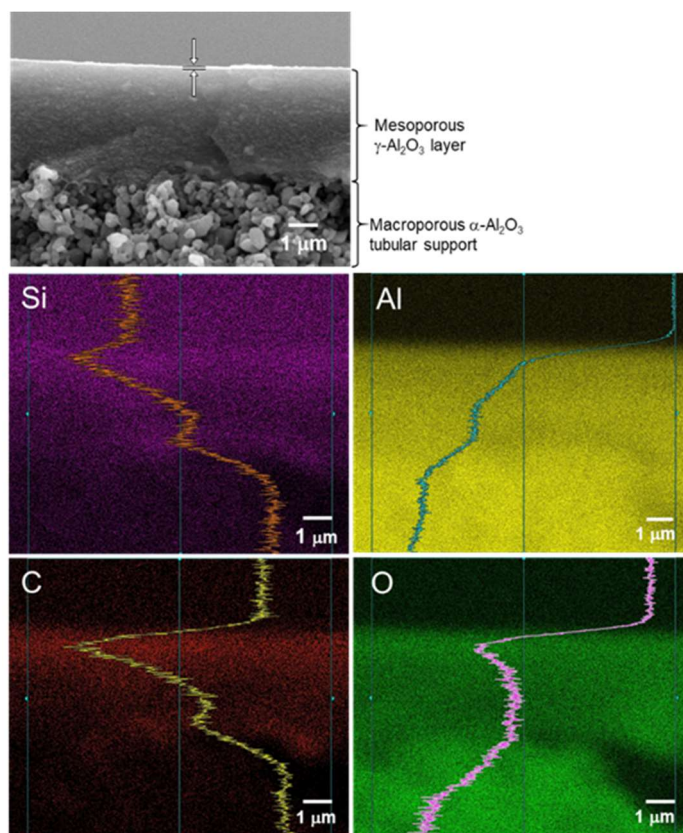


Fig. 4-5. A typical cross-sectional SEM image of PCS(UH) and line scan of EDS mapping for Si, C, Al and O detected at the top surface and within the mesoporous $\gamma\text{-Al}_2\text{O}_3$ layer.

(2) Gas permeation behaviors under dry condition

Figure 4-6 shows Arrhenius plots of He, H₂ and N₂ permeances measured for the supported PCS membranes and Figure 4-7 presents the effect of mean molecular weight (Mw) of starting PCS on the gas permeation properties at 50 °C of the supported PCS membranes shown in Fig. 4-6. Even at a low permeation temperature of 25 °C, the supported PCS membranes exhibited a relatively high H₂ permeance of $8.9\text{-}12 \times 10^{-7} \text{ mol m}^{-2} \text{ s}^{-1} \text{ Pa}^{-1}$ with a H₂/N₂ permselectivity ($\alpha(\text{H}_2/\text{N}_2)$) of 11.5-13.7. Furthermore, these membranes showed a similar temperature dependence of the gas permeations: all the gas permeances linearly increased with the permeation temperature, *i.e.* following the Arrhenius law.

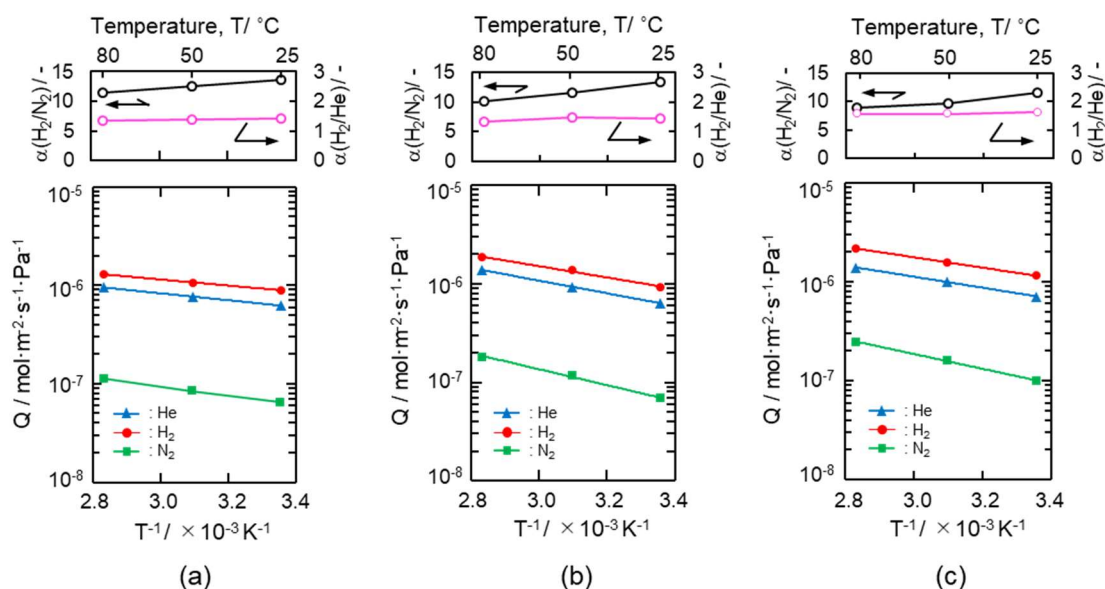


Fig. 4-6. Gas permeation behaviors under dry condition at 25 to 80 °C of the supported PCS membrane, (a) PCS(A), (b) PCS(UH) and (c) PCS(UUH).

As we reported previously (the subsection 2.3.3.1 in Chapter 2), gas permeations through the supported γ -Al₂O₃ layer itself was governed by the Knudsen's diffusion, and the $\alpha(\text{H}_2/\text{N}_2)$ was measured to be 3.41, which was a slight lower than the theoretical one (3.73) based on the Knudsen's diffusion. The $\alpha(\text{H}_2/\text{N}_2)$ values of the supported PCS membranes synthesized in this study were apparently higher than the theoretical one based on the Knudsen's diffusion. These superior H₂-selectivity could be provided by the PCS top-layer. However, as shown in Fig. 4-7, following tendencies were found: with increasing Mw of starting PCS, each gas permeance slightly increased, while $\alpha(\text{H}_2/\text{N}_2)$ decreased, *i.e.* compared with H₂, permeance of N₂ preferentially increased consistently with the Mw. These results suggested that a slight but appreciable amount of N₂ permeable pore channels by activated diffusion, *i.e.* micropore channels with a size closed to the kinetic diameter of N₂ (0.364 nm) [4] increased with Mw of the starting PCS.

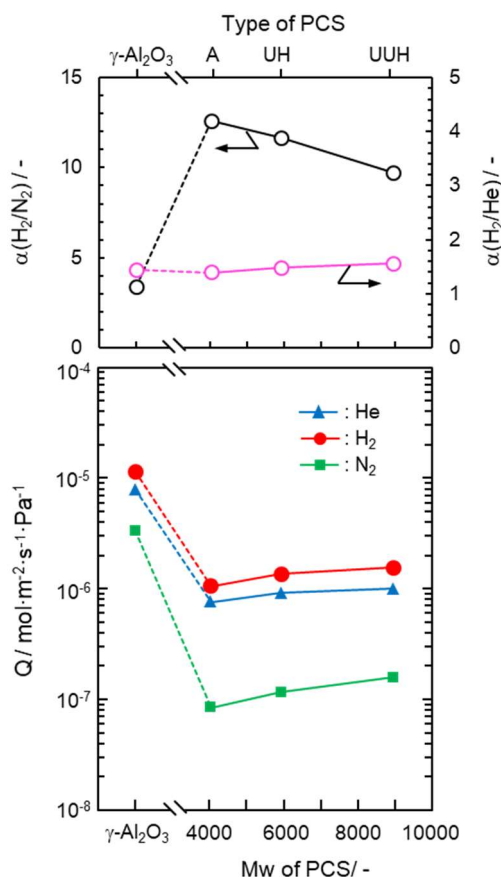


Fig. 4-7. Gas permeation properties at 50 °C under dry condition of PCS membranes supported on a mesoporous $\gamma\text{-Al}_2\text{O}_3$ layer as a function of Mw of starting PCS and those of the mesoporous $\gamma\text{-Al}_2\text{O}_3$ layer itself placed on a macroporous $\alpha\text{-Al}_2\text{O}_3$ tubular support (in Chapter 2).

The performance under dry condition of the present PCS membranes was compatible with SiO_2 -based organic-inorganic hybrid membranes [11]: organic methylene (CH_2) or ethylene (CH_2CH_2) group was introduced to amorphous silica network by using 1,2-bis(triethoxysilyl)methane (BTESM) or 1,2-bis(triethoxysilyl)ethane (BTESE) as a starting silicon alkoxide for the hybrid membrane synthesis through the sol-gel route. The hybrid membranes exhibited H_2 permeance of $7.7 - 18 \times 10^{-7} \text{ mol m}^{-2} \text{ s}^{-1} \text{ Pa}^{-1}$ with $\alpha(\text{H}_2/\text{N}_2)$ of approximately 12-20 at 40-50 °C [11]. However, an interesting gas permeation behavior was that, regardless of the Mw of the starting PCS, H_2 permeance was highest at all permeation temperatures from 25 to 80 °C, and the $\alpha(\text{H}_2/\text{He})$ of the supported PCS membranes was measured to be 1.4-1.6 (Figs. 4-6 and 4-7). This result was unexpected because the permeance order of $\text{H}_2 > \text{He} > \text{N}_2$ did not follow the kinetic diameter of gas molecule (He: 0.26 nm, H_2 : 0.289 nm and N_2 : 0.364 nm) [4]. Thus, the supported PCS

membranes synthesized in this study did not show simple molecular sieve properties based on the selective permeation of smaller gas molecules through micropore channels.

(3) Gas permeation behaviors under wet condition

Among the supported PCS membranes synthesized in this study, PCS(A) with the highest $\alpha(\text{H}_2/\text{N}_2)$ under dry condition was selected for further study on the gas permeation behavior under wet condition. Since the hydrogen purification process operation temperatures in the novel solar hydrogen production systems have been suggested as around 50 °C (as mentioned in Chapter 2 [12]), the measurements under wet condition in this study was performed at 50 °C.

As shown in Fig. 4-8(a), all the gas permeances except water vapor gradually decreased with the water vapor partial pressure ($p/p_0(\text{H}_2\text{O})$). However, even under the saturated water vapor partial pressure ($p/p_0(\text{H}_2\text{O}) = 1$) at 50 °C, the PCS(A) exhibited relatively a high H_2 permeance of $7.7 \times 10^{-8} \text{ mol}^{-1} \text{ m}^{-2} \text{ s}^{-1} \text{ Pa}^{-1}$.

Under the $p/p_0(\text{H}_2\text{O})$ ranging from 0.1 to 1.0, the $\alpha(\text{H}_2/\text{He})$ was almost constant (1.1 to 1.3), while the $\alpha(\text{H}_2/\text{N}_2)$ increased consistently with $p/p_0(\text{H}_2\text{O})$. Especially, above $p/p_0(\text{H}_2\text{O})$ of 0.74, the $\alpha(\text{H}_2/\text{N}_2)$ rapidly increased to reach 26 at the $p/p_0(\text{H}_2\text{O}) = 1.0$. Moreover, this rapid increase was found to be associated with the drastic increase in the $\alpha(\text{H}_2\text{O}/\text{N}_2)$. At the $p/p_0(\text{H}_2\text{O}) = 1.0$, the $\alpha(\text{H}_2\text{O}/\text{N}_2)$ got to be 107 (Fig. 4-8(b)).

When the measurement was performed using a $\text{H}_2\text{-N}_2$ (2:1) mixed feed gas (Figs. 4-8(c) and (d)), the $p/p_0(\text{H}_2\text{O})$ dependency up to $p/p_0(\text{H}_2\text{O}) = 0.74$ of the membrane performance in terms of the H_2 permeance and the $\alpha(\text{H}_2/\text{N}_2)$ was quite similar to that characterized by measuring single gas permeances. However, under the $p/p_0(\text{H}_2\text{O})$ above 0.74, N_2 permeance intensively decreased. Finally, at the $p/p_0(\text{H}_2\text{O}) = 1.0$, the N_2 permeance was below the limit of detection, and the PCS(A) was found to show an excellent H_2 -selectivity under the saturated water vapor partial pressure at 50 °C.

To investigate the gas permeation properties under the present humid conditions in more detail, the single gas permeances were measured for a reference sample, sol-gel derived SiO_2 membrane formed on the same type of mesoporous $\gamma\text{-Al}_2\text{O}_3$ -modified $\alpha\text{-Al}_2\text{O}_3$ macroporous support. As shown in Fig. 4-8(e), the H_2 permeance and $\alpha(\text{H}_2/\text{N}_2)$ of the supported SiO_2 membrane initially evaluated under dry condition at 50 °C were $7.1 \times 10^{-8} \text{ mol}^{-1} \text{ m}^{-2} \text{ s}^{-1} \text{ Pa}^{-1}$ and 39, respectively. Under wet condition, all the gas permeances immediately decreased at $p/p_0(\text{H}_2\text{O}) = 0.1$, then consistently decreased with $p/p_0(\text{H}_2\text{O})$. Finally, at $p/p_0(\text{H}_2\text{O}) = 1$, the He permeance was $2.1 \times 10^{-9} \text{ mol}^{-1} \text{ m}^{-2} \text{ s}^{-1} \text{ Pa}^{-1}$, while the H_2 and N_2 permeances were below the limit of detection.

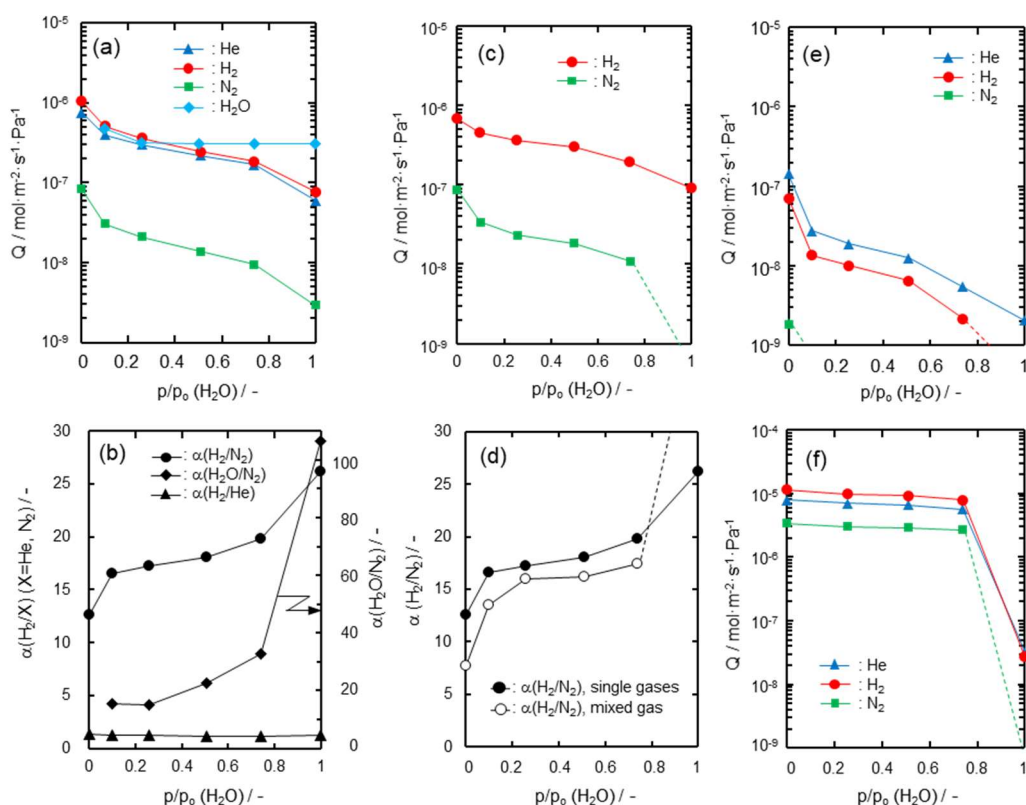


Fig. 4-8. Gas permeances and water vapor permeance at 50 °C evaluated for PCS(A) under $p/p_0(\text{H}_2\text{O})$ ranging from 0 to 1.0. The evaluation was performed by using (a), (b) single gases of He, H_2 and N_2 and (c) a mixed gas of H_2 and N_2 in the molar ratio 2 : 1. (d) Comparison of $\alpha(\text{H}_2/\text{N}_2)$ values evaluated based on the single gas permeances and those by using the H_2 - N_2 (2:1) mixed feed gas. Gas permeances evaluated for reference samples, (e) supported SiO_2 membrane and (f) supported mesoporous $\gamma\text{-Al}_2\text{O}_3$ membrane itself (in Chapter 2) under $p/p_0(\text{H}_2\text{O})$ ranging from 0 to 1.0 at 50 °C.

It was well known that microporous SiO_2 membranes having molecular-sieving properties were beneficial to H_2 separation [13–18]. Actually, under the initial dry condition, the smaller kinetic diameter below 0.3 nm of the permeate gas was, the higher permeance through the present sol-gel derived SiO_2 membrane showed.

The kinetic diameter of H_2O molecule was reported as 0.265 nm [4], sufficiently smaller than the suggested mean diameter of gas-permeable micropore channels within SiO_2 (0.3 nm [13]). Water vapor could permeate through the SiO_2 membrane, which lead to the plugging of gas-permeable micropore channels by adsorption and subsequent capillary condensation of H_2O molecules as the permeate [19–21]; the apparent decrease in gas permeances by presence of the minute water vapor ($p/p_0(\text{H}_2\text{O}) = 0.1$) agreed well with the hydrophilic characteristics of the sol-gel derived SiO_2 shown in Fig. 4-2(a).

However, the rapid degradation under the higher humid condition above $p/p_0(\text{H}_2\text{O})$ of 0.5 was inconsistent with the H_2O adsorption behavior shown in Fig. 4-2(a): At around

p/p_0 (H_2O) = 0.4, the amount of water vapor adsorption measured for the SiO_2 reached maximum, while both He and H_2 permeances decreased rather rapidly above p/p_0 (H_2O) = 0.5 (Fig. 4-8(e)). This was due to the high hydrophilicity of the mesoporous $\gamma\text{-Al}_2\text{O}_3$ layer beneath the SiO_2 membrane. As we reported in our previous study in Chapter 2, above p/p_0 (H_2O) = 0.4, the water vapor adsorption-desorption isotherm for the sol-gel derived mesoporous $\gamma\text{-Al}_2\text{O}_3$ exhibited a large hysteresis loop assigned to capillary condensation of H_2O molecules within mesopores, which lead to the drastic decrease in gas permeances through the supported mesoporous $\gamma\text{-Al}_2\text{O}_3$ layer itself under the high-humidity conditions at 50 °C (Fig. 4-8(f), as discussed in section 2.3.3.2 in Chapter 2). Accordingly, in addition to the intrinsic degradation by the permeate H_2O -induced plugging within the SiO_2 membrane, gas permeations through the supported SiO_2 membrane could be intensively restricted by condensation of the permeate H_2O molecules within mesopores located close to the hetero interface between the $\gamma\text{-Al}_2\text{O}_3$ layer and the top surface SiO_2 membrane.

As shown in Fig. 4-8(a), the PCS(A) exhibited a relatively high water vapor permeance of $3.1 \times 10^{-7} \text{ mol}^{-1} \text{ m}^{-2} \text{ s}^{-1} \text{ Pa}^{-1}$ at the p/p_0 (H_2O) = 1.0. This value was compatible with that previously measured for the supported mesoporous $\gamma\text{-Al}_2\text{O}_3$ layer itself ($7.1 \times 10^{-7} \text{ mol}^{-1} \text{ m}^{-2} \text{ s}^{-1} \text{ Pa}^{-1}$) (Fig. 2-10(a), as discussed in Chapter 2). Thus, gas permeation property of the PCS(A) could be also affected by the highly hydrophilic character of the mesoporous $\gamma\text{-Al}_2\text{O}_3$ layer. However, an interesting point was that the affection in terms of the decrease in permeance under the high-humidity conditions was mainly observed for N_2 gas, and such affection was more pronounced when the gas permeation measurement was performed by using a mixed $\text{H}_2\text{-N}_2$ (2:1) gas (Fig. 4-8(c)). These results suggested that the dominant permeation of N_2 and water vapor was diffusion through micropore channels within the PCS top-layer network. Under higher humid conditions above p/p_0 (H_2O) = 0.74, N_2 permeation was thought to be restricted by the highly hydrophilic mesoporous $\gamma\text{-Al}_2\text{O}_3$ layer as in the case of the supported SiO_2 membrane discussed above. On the other hand, the He and H_2 permeations through the PCS(A) were thought to be governed by diffusion through the hydrophobic and dense PCS top-layer network where neither H_2O nor N_2 could permeate.

4.3.3 Analysis of gas permeation behaviors

(1) He and H_2 permeations

In order to quantitatively explain the mechanism of He and H_2 permeation through the PCS top-layer network, the He and H_2 permeances were measured at room temperature to 200 °C (sufficiently high above 150 °C to examine the affection by physisorption of gas molecules [17,18]), and analyzed using a solid-state diffusion model [22–25]. In this analysis, another membrane sample, PCS(UH) having a higher m.p. (350 °C) was adopted.

Solid-state diffusion occurs with further decrease in the pore size than Knudsen diffusion occurs, where the gas molecule interacts strongly with the membrane material behaving as a dense material. In this case, the solubility of the gas molecule is necessary

to consider, so that the molecules permeance through the membrane (Q) can be expressed by the product of the solubility and the diffusivity. The solubility (S) is derived from the equilibrium between the solubility sites and the gaseous phase [26]. The diffusivity (D) is supposed that the process of gas atom movement between solubility sites in the membrane is a random walk process with an equilibrium established between atoms in solubility sites and those moving between sites [27]. Gas molecules, vibrating at solubility sites with a characteristic frequency, jump to an adjacent solubility site by surmounting a potential barrier. The permeance (Q = SD) is given by following equation, considering the effect of rotation of polyatomic gas molecule:

$$Q_{ss} = \frac{d^2 h^2}{6L} \left(\frac{1}{2\pi m k T} \right)^{\frac{3}{2}} \left(\frac{\sigma h^2}{8\pi^2 I k T} \right)^\alpha \times \frac{(N_s/N_A)}{(e^{h\nu^*/2kT} - e^{-h\nu^*/2kT})^2} e^{\frac{-\Delta E_{ss}}{RT}} \quad (4-1)$$

where Q_{ss} is the permeance through the membrane [$\text{mol m}^{-2} \text{s}^{-1} \text{Pa}^{-1}$], d is jump distance [m], h is Planck's constant [$\text{m}^2 \text{kg s}^{-1}$], L is the thickness of the membrane [m], m is the mass [kg], ν^* is vibrational frequency of the gas molecules in the passageways between the sorption sites [s^{-1}], k is Boltzmann's constant [J K^{-1}], T is the temperature [K], σ is the symmetry factor of the species ($\sigma=2$ for H_2), I is the moment of inertia [kg m^2], N_s is number of solubility sites per area [m^{-3}], N_A is Avogadro's number [mol^{-1}], ΔE_{ss} is activation energy for permeation [J mol^{-1}], α is an exponent accounting for incomplete loss of rotation ($\alpha = 0$ for monoatomic molecule, He, and $\alpha = 0.2$ for polyatomic molecule, H_2), R is the gas constant [$\text{J mol}^{-1} \text{K}^{-1}$].

As shown in Fig. 4-9(a), at all temperatures up to 200 °C (473 K), the experimental permeance of H_2 was higher than that of He, and each gas permeance monotonously increased with the permeation temperature. Then, the temperature dependence of the He and H_2 permeances were fitted to the non-linear curve by the Eq. (4-1) with three free parameters, N_s , ν^* and ΔE_{ss} which were determined using Igor Pro 7.00 (wavemetrics, Inc., OR, USA). The membrane thickness (L) was 50 nm as obtained from the SEM image shown in Fig. 4-4 and jump distance (d) was 0.8 nm which was used by following previous reports [22,28]. The calculated permeances of He and H_2 were well consistent with experimental data, so that the solid-state diffusion model fitting analysis was to be made appropriately.

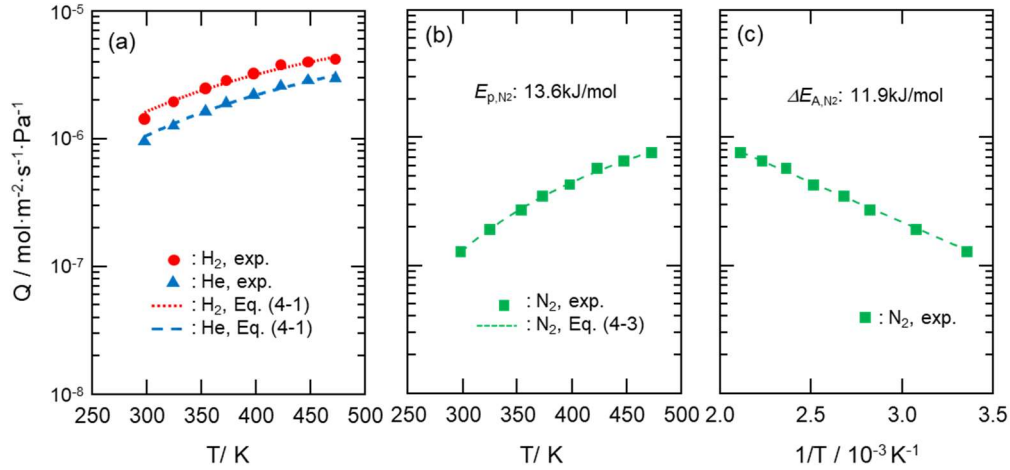


Fig. 4-9. Study on temperature dependence of gas permeances through the PCS(UH) at room temperature to 473 K (200 °C). Comparison of experimentally evaluated (a) H₂ and He permeances with those calculated using solid-state diffusion model (Eq. (4-1)) and (b) N₂ permeances with those calculated based on the modified gas-translational diffusion model (Eq. (4-3)). (c) Arrhenius plot of the experimentally evaluated N₂ permeances.

The fitting parameters obtained in this study were listed in Table 4-2, and compared with those for H₂-selective amorphous ceramic membranes previously reported by other research groups: polysiloxane-derived amorphous silicon oxycarbide (SiOC) membrane (#01) synthesized by pyrolysis at 700 °C in Ar [28], and CVD-derived SiO₂ membranes (#02~05) having different microporosity which Oyama *et al.* [24,25,29,30] systematically synthesized by varying the organic ligand of starting Si alkoxide precursor and CVD process temperature in Ar: #02 [29] and #03 [24] (tetraethoxysilane (TEOS) at 600 °C), #04 (vinyltriethoxysilane (VTES) at 600 °C) [25], #05 (35% trimethylmethoxysilane (TMMOS) -TEOS at 650 °C) [30].

Table 4-2. Comparison of H₂ permeation properties and fitting parameters.

No.	Membrane	H ₂ permeation properties				$N_s / 10^{25} \text{ m}^{-3}$		$\nu^* / 10^{12} \text{ s}^{-1}$		$\Delta E_{ss} / \text{kJ mol}^{-1}$	
		T/K	$Q_{H_2} / \text{mol m}^{-2} \text{ s}^{-1} \text{ Pa}^{-1}$	$\alpha(H_2/X)/-$	X	He	H ₂	He	H ₂	He	H ₂
This work	PCS(UH)	323	1.4×10^{-6}	11.7	N ₂	15.0	11.0	0.60	0.66	5.9	5.8
#01	SiOC [28]	573	1.78×10^{-8}	22.4	N ₂	1.3	0.76	0.082	0.089	8.5	7.9
#02	SiO ₂ [29]	873	1.2×10^{-7}	1800	CO	74.0	27.3	7.77	8.10	8.0	12.8
#03	SiO ₂ [24]	873	5.0×10^{-7}	5100	CO	62	38	7.0	7.3	4.2	10.4
#04	SiO ₂ [25]	873	5.4×10^{-7}	150	N ₂	47.5	33.5	2.21	2.39	3.4	7.3
#05	SiO ₂ [30]	923	1.1×10^{-6}	53	N ₂	15.7	8.7	2.94	3.02	-0.08	1.86

There were two criteria for this curve fitting study: (1) N_s , the number of solubility sites should be in inverse relation to the kinetic diameter of the permeate gas molecule because the larger gas molecule could not fit into more solubility sites, and thus N_s for H₂

(0.289 nm) < N_S for He (0.26 nm). (2) ν^* , the vibrational frequency should be higher for the permeate gas having the smaller molecular weight, *i.e.*, ν^* for H₂ (2.02 g mol⁻¹) > ν^* for He (4.00 g mol⁻¹). As shown in Table 4-2, the values of N_S and ν^* estimated for He and H₂ permeations through the PCS(UH) corresponded to the physical constants mentioned above, and similar to those previously reported for the membranes composed of SiOC (#01) [28] or SiO₂ (#02~05) [24,25,29,30].

Due to several differences in material factors of the network which composing active separation layer such as chemical composition and density, it was difficult to discuss on the difference in the fitting parameters, however, the values of N_S for He and H₂ permeations through the present PCS top-layer were compatible with those reported for the CVD-derived SiO₂ membrane (#05) with relatively low density, fabricated by using stating Si alkoxides having organic ligands such as 35%TMMOS-TEOS [30]. On the other hand, the ν^* values for both He and H₂ were apparently lower than those reported for the CVD-derived SiO₂ membranes (#02~05) [24,25,29,30], but were approximately one order of magnitude higher than those reported for the polymer-derived SiOC membrane (#01) [28].

One unique result was the ΔE_{ss} , activation energy obtained for the present PCS top-layer. ΔE_{ss} has an inverse relationship with N_S physically, because the larger molecules must overcome a larger energy barrier to migrate through the membrane. In this context, all the data reported for the SiO₂ membranes (#02~05) followed this relation, and the ΔE_{ss} for H₂ permeation was apparently higher than that of He [24,25,29,30]. On the other hand, the ΔE_{ss} for H₂ permeation through the PCS top-layer was evaluated as 5.8 kJ mol⁻¹ and found to be rather slight lower than that for the He permeation (5.9 kJ mol⁻¹). This result corresponded well with the unique H₂-permselectivity experimentally observed for the PCS(UH), H₂ permeance increased consistently with temperature, and at all temperatures up to 200 °C, the permeance of H₂ was higher than that of the smaller gas molecule of He (Fig. 4-9(a)).

Gurlo *et. al* reported that the polymer-derived SiOC membrane (#01) exhibited a similar H₂-permselectivity, and as shown in Table 4-2, their fitting study also resulted in the irregular relation, $\Delta E_{ss} / \text{kJ mol}^{-1}$ for He permeation (8.5) > for H₂ permeation (7.9) [28]. The PCS top-layer investigated in this study was ternary SiCH organic-inorganic hybrid polymer composed Si-C backbone substituted with considerable amount of CH₃ groups. Accordingly, it was suggested that the existence of such hydrocarbon groups allowed preferential dissolution and subsequent diffusion of H₂ explained by the solid-state diffusion mechanism discussed above. Moreover, it was found that the ΔE_{ss} (5.8 kJ mol⁻¹) for the H₂ permeation through the present PCS membrane was much lower than those (16.3-16.7 kJ mol⁻¹) of silicon oxycarbide (SiOC) membranes derived from polydimethylsilane (PMS) reported by Tsai *et al.* [31]. According to the reported membrane syntheses route, prior to the final pyrolysis at 300-600 °C, PMS was thermally converted to PCS via the Kumada rearrangement during the heat treatment at 460 °C for 14 h under Ar, then cured at 200 °C in air for 1h. The PCS formed in-situ could be highly

reactive to be well cross-linked during the long-time heat treatment at 460 °C. Moreover, the heat-treated PCS became infusible via Si-O-Si bond formations by the subsequent curing in air. These thermal treatments led to the formation of dense network like microporous amorphous SiO₂ in spite of the final low-temperature pyrolysis at 300 to 600 °C.

(2) N₂ permeation

In addition to He and H₂ permeances, the temperature dependence of N₂ permeance was measured for the same PCS(UH). As shown in Fig. 4-9(b), N₂ permeance also increased consistently with permeation temperature.

As discussed above, the dominant permeation of N₂ could be diffusion through micropore channels within the PCS top-layer network. Then, the temperature dependence of the N₂ permeance was examined using a permeation model equation recently proposed by Yoshioka *et al.* [17], which considering the effect of the potential field in a micropore [17,32]:

$$Q_{cKL} = \frac{k_0}{\sqrt{M_i RT}} (d_0 - d_i)^3 \exp\left(-\frac{E_{act,i} + E_{att,i}}{RT}\right), \quad k_0 = \frac{N_p \sqrt{2\pi}}{6\tau A_m L} \quad (4-2)$$

where Q_{cKL} [mol m⁻² s⁻¹ Pa⁻¹] is the Knudsen permeance of gas molecules that are concentrated by the attractive nature of the potential field of pore wall, d_0 is native pore diameter [m], d_i is kinetic diameter of i -th component [m], N_p is the number of pores with pore diameters of d_0 on the membrane, τ is the tortuosity [-], A_m is the membrane area [m²], L is the thickness of the membrane [m], M_i is the molar weigh of the i -th diffusing gas component [kg mol⁻¹], $E_{act,i}$ is the activation energy for the permeation of the i -th component [J mol⁻¹], $E_{att,i}$ is the attractive potential energy for the i -th component [J mol⁻¹], R is the gas constant [J mol⁻¹ K⁻¹], and T is the permeation temperature [K].

Equation (4-2) is a modified gas-translational (GT) diffusion [33–35] (mGT) model equation with the additional consideration of the effective diffusion length ($d_0 - d_i$) and provides a more detailed description of the gas permeation model equation by considering activation energy, adsorption energy and size of permeate gas molecule. Accordingly, the mGT model can be expected to achieve universal understandings of the permeation mechanisms in a micropore from Knudsen diffusion to activated diffusion [17,32].

In this study, Q_{cKL} was renamed as Q_{mGT} and expressed by simplifying Eq. (4-2) as:

$$Q_{mGT} = \frac{k_{0,i}}{\sqrt{M_i RT}} \exp\left(-\frac{E_{p,i}}{RT}\right) \quad (4-3)$$

where $k_{0,i} = k_0 (d_0 - d_i)^3$, and $E_{p,i} = E_{act,i} + E_{att,i}$. Then, the value of $E_{p,i}$ for the N₂ permeation was estimated by fitting Eq. (4-3) to the experimentally obtained temperature dependency data with two free parameters, $k_{0,i}$ and $E_{p,i}$. These parameters were also determined using Igor Pro 7.00. As shown in Fig. 4-9(b), the calculated permeance of N₂ was well

consistent with experimental data, and the fitting parameter, $E_{p,i}$ was found as 13.6 kJ mol^{-1} .

As we reported previously, the PCSs exhibited extremely low affinity toward N_2 , and it was impossible to measure the BET (Brunauer–Emmett–Teller) surface area by using N_2 as a probe molecule at 77 K [10]. Accordingly, even at room temperature, the E_{att,N_2} could be negligibly small, and thus $E_{p,N_2} \approx E_{act,N_2}$. Moreover, the E_{p,N_2} was compatible with the activation energy for N_2 permeation ($\Delta E_{A,N_2}$, 11.9 kJ mol^{-1}) obtained by the Arrhenius plot (Fig. 4-9(c)). The dominant mechanism for the N_2 permeation could be recognized as activated diffusion, which indicated that the PCS top-layer had a microporosity with the size of pore channels close to the kinetic diameter of N_2 gas molecule (0.364 nm).

(3) Effect of water vapor partial pressure on gas permeations

A schematic diagram of Fig. 4-10 presents possible gas permeation behaviors through the PCS membrane supported on a mesoporous $\gamma\text{-Al}_2\text{O}_3$ layer investigated in this study.

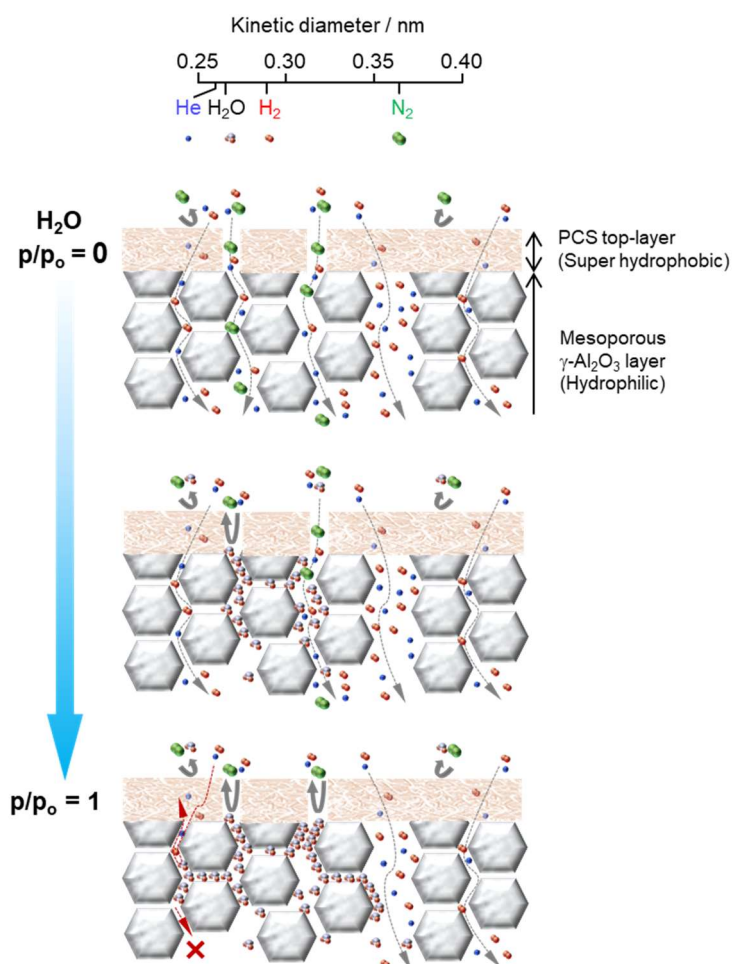


Fig. 4-10. Schematic of gas permeation behaviors through a PCS membrane supported on a mesoporous $\gamma\text{-Al}_2\text{O}_3$ layer under dry and wet conditions at $50 \text{ }^\circ\text{C}$.

He and H₂ dominantly permeated through the dense PCS top-layer network governed by the solid-state diffusion mechanism, while the dominant N₂ permeation was activated diffusion through the micropore channels within the PCS network. The size of the micropore channels could be close to the kinetic diameter of N₂ (d_{N_2} , 0.364 nm) [4].

The kinetic diameter of water vapor (H₂O molecule, 0.265 nm) [4] was sufficiently smaller than d_{N_2} . Moreover, the PCS was highly hydrophobic, which allowed stable water vapor permeation through the N₂-permeable micropore channels within the PCS top-layer. However, immediate adsorption and subsequent condensation of the permeate H₂O molecules could proceed at the entrance to the highly hydrophilic mesoporous γ -Al₂O₃ layer beneath the PCS top-layer, *i.e.* at the hetero interface between the PCS layer and mesoporous γ -Al₂O₃ layer.

Then, the relationship between the $p/p_0(\text{H}_2\text{O})$ and degree of the permeate H₂O-induced plugging was examined in the following attempt: The entrance to the mesoporous γ -Al₂O₃ layer was treated as a cylindrical pore having a mean effective diameter, $d_{ent.}$ Under the $p/p_0(\text{H}_2\text{O})$ ranging from 0.1 to 1.0, the $d_{ent.}$ was estimated by calculating the normalized Knudsen-based permeance (NKP) f_{NKP} , which is defined as the ratio of the permeance of a target component (Q_i) to standard gas permeance (Q_S), that considers the contribution of molar weight can be given as a function of gas molecular size, d_i by measuring the gas permeances of several gases at a given constant temperature [17],

$$f_{NKP} = \frac{Q_i}{Q_S} \sqrt{\frac{M_i}{M_S}} = \frac{(d_{ent.} - d_i)^3 \exp\left(-\frac{E_{p,i}}{RT}\right)}{(d_{ent.} - d_S)^3 \exp\left(-\frac{E_{p,S}}{RT}\right)} \approx \left(\frac{1 - \frac{d_i}{d_{ent.}}}{1 - \frac{d_S}{d_{ent.}}}\right)^3 \quad (4-4)$$

Under the limiting conditions of $d_S < d_i < d_{ent.}$, kinetic diameter depending on the f_{NKP} was fitted to the non-linear curve by Eq. (4-4) with two free parameters, f_{NKP} and $d_{ent.}$ which were determined using Igor Pro 7.00. The vales of f_{NKP} were calculated using the permeance through the PCS(A) under dry and wet condition at 323 K (50 °C) shown in Fig. 4-8(a). The permeance and molecular size of He were adopted as Q_S and d_S , respectively. In this estimation, the plots for H₂O and H₂ were excluded from the fitting, because H₂O was condensable under the present wet condition, while H₂ preferentially permeated through the PCS top-layer. The results are shown in Fig. 4-11. For comparison, the f_{NKP} values for H₂O and H₂ were marked or listed in this graph. The $d_{ent.}$ under the initial dry condition was estimated as 0.57 nm, then got to be smaller consistently with the $p/p_0(\text{H}_2\text{O})$. Finally, the $d_{ent.}$ at $p/p_0(\text{H}_2\text{O})=1.0$ was estimated as 0.47 nm.

The $d_{ent.}$ values estimated were indeed large enough for all the gases of He, H₂ and N₂ to permeate through, but plugging of a certain fraction of the entrance having a much smaller diameter (closed to d_{N_2} , 0.364 nm) could proceed under the high-humidity conditions of $p/p_0(\text{H}_2\text{O}) > 0.5$ at 50 °C.

As shown in Fig. 4-8(a), there was a tendency that all the gas permeances decreased with increasing p/p_0 (H_2O), which could be due to the increase in the pressure drop caused by increasing amount of the H_2O molecules condensed at around the hetero interface. This affection was more pronounced in the case using the H_2 - N_2 (2:1) mixed feed gas, *i.e.* when the driving force for N_2 gas permeation was reduced by decreasing the partial pressure difference between the gas feed side and permeate side of the membrane under the saturated water vapor partial pressure at 50 °C (Figs. 4-8(c) and (d)). On the other hand, at p/p_0 (H_2O) > 0.1, the water vapor exhibited a stable permeation with a relatively high permeance of approximately 3.0×10^{-7} [$\text{mol m}^{-2} \text{s}^{-1} \text{Pa}^{-1}$] at 50 °C (Fig. 4-8(a)). The observed water vapor permeation was thought to be governed by the surface diffusion/capillary condensation along with the extremely hydrophilic γ - Al_2O_3 mesopore wall.

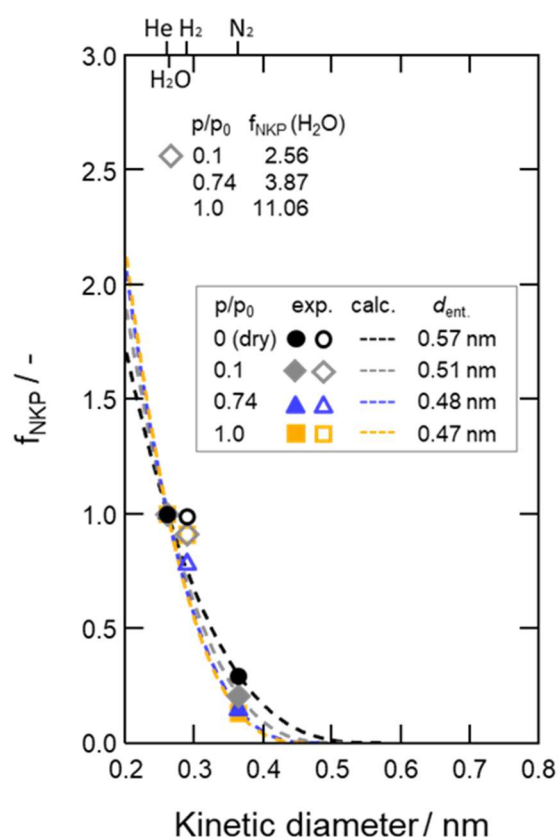


Fig. 4-11. Dependencies of normalized Knudsen-based permeance, f_{NKP} on kinetic diameter and p/p_0 (H_2O): f_{NKP} derived from experimentally evaluated gas permeances through the PCS(A) under dry (p/p_0 (H_2O) = 0) and wet condition at the p/p_0 (H_2O) of 0.1, 0.74 and 1.0 at 323 K (50 °C) shown in Fig. 4-8(a), and the mean pore diameter of the entrance to mesoporous γ - Al_2O_3 layer, d_{ent} , calculated based on the simple-NKP plot using solid plots of He and N_2 permeances.

4.4 Summary

In the present study, super hydrophobicity of PCSs was characterized by measuring water vapor adsorption-desorption isotherms at 25 °C. Then, the PCS membrane with a thickness of about 50 nm was successfully formed over a mesoporous γ -Al₂O₃ layer placed on an outer surface of a macroporous α -Al₂O₃ tubular support. Under dry and wet condition, gas permeances through the supported PCS membranes were assessed and discussed to clarify their possible permeation mechanisms. The results can be summarized as follows:

Water vapor adsorption-desorption isotherms measurements revealed that the amount of water adsorption under the saturated water vapor partial pressure at 25 °C of the PCSs was below 4 cm³(STP)g⁻¹, which showed significantly high hydrophobicity.

Under dry condition, the single gas permeances of He, H₂ and N₂ through the supported PCS membranes lineally increased with the permeation temperature, *i.e.* following the Arrhenius law. At 50 °C, the supported PCS membranes exhibited high H₂ permeance of 10⁻⁶ mol⁻¹ m⁻² s⁻¹ Pa⁻¹ order. Moreover, in addition to H₂/N₂ selectivity of 9.7-12.6, the supported PCS membranes exhibited unique H₂/He selectivity of 1.4 to 1.6. The gas permeation properties under dry condition was governed by the PCS top-layer network. The best membrane performance at 50 °C was achieved for the supported membrane synthesized using the PCS having Mw of 4042 (PCS(A)). The H₂ permeance, H₂/He and H₂/N₂ selectivities were measured to be 1.1 x 10⁻⁶ mol⁻¹ m⁻² s⁻¹ Pa⁻¹, 1.4 and 12.6, respectively.

Even under saturated water vapor partial pressure at 50 °C, the PCS(A) kept a relatively high H₂ permeance of 7.7 x 10⁻⁸ mol⁻¹ m⁻² s⁻¹ Pa⁻¹ with improved H₂/N₂ selectivity of 26.

The dominant mechanism for He and H₂ permeations through the PCS top-layer was suggested as solid state diffusion through the dense ternary SiCH organic-inorganic hybrid polymer network. Theoretical study using the solid state diffusion model performed on the He and H₂ permeations up to 200 °C supported the experimentally observed preferential H₂ permeation: The estimated activation energy for H₂ permeation through the PCS top-layer was 5.8 kJ mol⁻¹ and was found to be slightly lower than that for the He permeation (5.9 kJ mol⁻¹).

The activation energy for N₂ permeation through the supported PCS membrane was estimated by using a modified gas-translational diffusion (mGT) model as 13.6 kJ mol⁻¹. This value was compatible with that obtained by the conventional Arrhenius plot (11.9 kJ mol⁻¹). These results revealed that the N₂ permeation was activated diffusion through micropore channels within the PCS polymer network. The channel pore sizes were thought to be close to the kinetic diameter of N₂ gas molecule, 0.364 nm.

The enhanced H₂-permeability observed under the high-humidity conditions at 50 °C was explained by the synergistic effect of the preferential H₂ permeation through the dense PCS top-layer network and blockage of N₂ permeation pathway by the permeate

H₂O-induced plugging at around the hetero interface between the superhydrophobic PCS and highly hydrophilic γ -Al₂O₃ layers. As a result, when the H₂-N₂ (2:1) mixed feed gas was used for measuring gas permeances under saturated humidity at 50 °C, the N₂ permeance was below the limit of detection, which showed great potential of PCSs to develop high-performance membranes for hydrogen recovery from the syngas produced by the novel solar hydrogen production systems.

References

- [1] Currently, polycarbosilanes (“Nipusi®”) are available from Artkagaku Co. Ltd., <http://www.artkagaku.co.jp/contact/index.html>.
- [2] M.H. Zahir, K. Sato, Y. Iwamoto, Development of hydrothermally stable sol–gel derived La₂O₃-doped Ga₂O₃–Al₂O₃ composite mesoporous membrane, *J. Memb. Sci.* 247 (2005) 95–101.
- [3] M.H. Zahir, K. Sato, H. Mori, Y. Iwamoto, M. Nomura, S.I. Nakao, Preparation and properties of hydrothermally stable γ -alumina-based composite mesoporous membranes, *J. Am. Ceram. Soc.* 89 (2006) 2874–2880.
- [4] D.W. Breck, *Zeolite Molecular Sieves: Structure, Chemistry, and Use*, John Wiley & Sons, New York, 1974.
- [5] K.S.W. Sing, D.H. Everett, R.A.W. Haul, L. Moscou, R.A. Pierotti, J. Rouquerol, T. Siemienieska, Reporting physisorption data for gas/solid systems with special reference to the determination of surface area and porosity, 1985.
- [6] S. Lowell, J.E. Shields, M.A. Thomas, M. Thommes, *Characterization of porous solids and powders*, Springer, Netherlands, 2004.
- [7] S. Yajima, K. Okamura, J. Hayashi, M. Omori, Synthesis of Continuous SiC Fibers with High Tensile Strength, *J. Am. Ceram. Soc.* 59 (1976) 324–327.
- [8] Y. Sawai, Y. Iwamoto, S. Okuzaki, Y. Yasutomi, K. Kikuta, S. Hirano, Synthesis of Silicon Carbide Ceramics Using Chemically Modified Polycarbosilanes as a Compaction Binder, *J. Am. Ceram. Soc.* 82 (1999) 2121–2125.
- [9] M.N. Mohd Sokri, T. Onishi, Y. Daiko, S. Honda, Y. Iwamoto, Hydrophobicity of amorphous silica-based inorganic-organic hybrid materials derived from perhydropolysilazane chemically modified with alcohols, *Microporous Mesoporous Mater.* 215 (2015) 183–190.
- [10] Z. Mouline, K. Asai, Y. Daiko, S. Honda, S. Bernard, Y. Iwamoto, Amine-functionalized polycarbosilane hybrids for CO₂-selective membranes, *J. Eur. Ceram. Soc.* 37 (2017) 5213–5221.
- [11] X. Ren, T. Tsuru, Organosilica-based membranes in gas and liquid-phase separation, *Membranes* 9 (2019) 107.
- [12] T. Yamada, K. Domen, Development of Sunlight Driven Water Splitting Devices towards Future Artificial Photosynthetic Industry, *ChemEngineering* 2 (2018) 36.
- [13] Y. Iwamoto, Precursors-Derived Ceramic Membranes for High-Temperature Separation of Hydrogen, *J. Ceram. Soc. Japan* 115 (2007) 947–954.
- [14] R.M. de Vos, H. Verweij, High-Selectivity, High-Flux Silica Membranes for Gas Separation, *Science* 279 (1998) 1710–1711.
- [15] Y. Iwamoto, K. Sato, T. Kato, T. Inada, Y. Kubo, A hydrogen-permselective amorphous silica membrane derived from polysilazane, *J. Eur. Ceram. Soc.* 25 (2005) 257–264.

- [16] A.K. Prabhu, S.T. Oyama, Highly hydrogen selective ceramic membranes: Application to the transformation of greenhouse gases, *J. Memb. Sci.* 176 (2000) 233–248.
- [17] T. Yoshioka, M. Kanezashi, T. Tsuru, Micropore size estimation on gas separation membranes: A study in experimental and molecular dynamics, *AIChE J.* 59 (2013) 2179–2194.
- [18] M. Kanezashi, T. Tsuru, Design of Amorphous Silica Network Structure for Molecular Sieving Membranes and Evaluation of Pore Size by Normalized Knudsen-based Permeance (NKP), *Zeolite* 35 (2018) 13–22.
- [19] K. Tanaka, Y. Sakata, Present and Future Prospects of Hydrogen Production Process Constructed by the Combination of Photocatalytic H₂O Splitting and Membrane Separation Process, *Membrane* 36 (2011) 113–121.
- [20] A. Burneau, J. Lepage, G. Maurice, Porous silica-water interactions. I. Structural and dimensional changes induced by water adsorption, *J. Non. Cryst. Solids* 217 (1997) 1–10.
- [21] T. Tsuru, T. Hino, T. Yoshioka, M. Asaeda, Permporometry characterization of microporous ceramic membranes, *J. Memb. Sci.* 186 (2001) 257–265.
- [22] S.T. Oyama, D. Lee, P. Hacarlioglu, R.F. Saraf, Theory of hydrogen permeability in nonporous silica membranes, *J. Memb. Sci.* 244 (2004) 45–53.
- [23] S.T. Oyama, M. Yamada, T. Sugawara, A. Takagaki, R. Kikuchi, Review on mechanisms of gas permeation through inorganic membranes, *J. Japan Pet. Inst.* 54 (2011) 298–309.
- [24] Y. Gu, S.T. Oyama, High Molecular Permeance in a Poreless Ceramic Membrane, *Adv. Mater.* 19 (2007) 1636–1640.
- [25] S.J. Ahn, G.N. Yun, A. Takagaki, R. Kikuchi, S.T. Oyama, Synthesis and characterization of hydrogen selective silica membranes prepared by chemical vapor deposition of vinyltriethoxysilane, *J. Memb. Sci.* 550 (2018) 1–8.
- [26] P.L. Studt, J.F. Shackelford, R.M. Fulrath, Solubility of Gases in Glass—A Monatomic Model, *J. Appl. Phys.* 41 (1970) 2777–2780.
- [27] J.S. Masaryk, R.M. Fulrath, Diffusivity of helium in fused silica, *J. Chem. Phys.* 59 (1973) 1198–1202.
- [28] R.M. Prasad, Y. Jüttke, H. Richter, I. Voigt, R. Riedel, A. Gurlo, Mechanism of gas separation through amorphous silicon oxycarbide membranes, *Adv. Eng. Mater.* 18 (2016) 721–727.
- [29] D. Lee, L. Zhang, S.T. Oyama, S. Niu, R.F. Saraf, Synthesis, characterization, and gas permeation properties of a hydrogen permeable silica membrane supported on porous alumina, *J. Memb. Sci.* 231 (2004) 117–126.
- [30] Y. Mise, S.J. Ahn, A. Takagaki, R. Kikuchi, S.T. Oyama, Fabrication and evaluation of trimethylmethoxysilane (TMMOS)-derived membranes for gas separation, *Membranes* 9 (2019) 123.
- [31] L.-L. Lee, D.-S. Tsai, A Hydrogen-Permeable Silicon Oxycarbide Membrane Derived from Polydimethylsilane, *J. Am. Ceram. Soc.* 82 (1999) 2796–2800.
- [32] T. Yoshioka, E. Nakanishi, T. Tsuru, M. Asaeda, Experimental studies of gas permeation through microporous silica membranes, *AIChE J.* 47 (2001) 2052–2063.
- [33] A.B. Shelekhin, A.G. Dixon, Y.H. Ma, Theory of gas diffusion and permeation in inorganic molecular-sieve membranes, *AIChE J.* 41 (1995) 58–67.

- [34] R.S.A. de Lange, K. Keizer, A.J. Burggraaf, Analysis and theory of gas transport in microporous sol-gel derived ceramic membranes, *J. Memb. Sci.* 104 (1995) 81–100.
- [35] A.J. Burggraaf, Single gas permeation of thin zeolite (MFI) membranes: Theory and analysis of experimental observations, *J. Memb. Sci.* 155 (1999) 45–65.

Chapter 5 Conclusions

This study aims at development of novel hydrogen permselective membranes for purification of solar hydrogen produced via photoelectrochemical water-splitting reaction at $T \leq 50$ °C. For application to this advanced hydrogen production system, there are several technical issues for current H₂ gas separation membranes: higher operating temperatures of approximately above 90 °C for polymer membranes and 350 °C for metal membranes, reverse reaction of molecular H₂ with O₂ to afford H₂O on the surface of metal membranes, water-induced swelling of polymer membranes and serious performance degradation by adsorption and subsequent condensation of H₂O molecules as permeate for hydrophilic microporous SiO₂-based membranes.

In this study, Si-based polymer-derived Si-C-H ternary organic-inorganic hybrid materials were selected based on their excellent stability toward ambient moisture and capability for the formation of surface coatings, membranes and composites via the conventional hydrocarbon-based polymer processing routes such as dip-coating and melt impregnation of fusible starting polymers. Moreover, the SiCH hybrids are categorized as Class II hybrid composed of hydrophobic alkyl substituents chemically bonded to inorganic Si-C polymer backbones which can be expected to show molecular sieve-like property for H₂-permselectivity, and thus resulting synergistic properties derived from the organic and inorganic components of the SiCH hybrid are highly expected to overcome the technical issues.

In Chapter 2, characterization of excellent hydrophobicity of PCS-derived SiCH-based organic-inorganic hybrids was performed by measuring water vapor adsorption-desorption isotherms at room temperature. Then, modification of the mesoporous γ -Al₂O₃ intermediate layer with the PCS-derived SiCH hybrid was investigated.

The water vapor adsorption-desorption isotherms measurement revealed that the maximum amount of water adsorption ($V_a(\text{H}_2\text{O})$) at room temperature of the conventional sol-gel-derived γ -Al₂O₃ was as high as 297 cm³(STP)g⁻¹. Under the humid condition at 50 °C, the permeances of He, H₂ and N₂ gas molecules through the supported mesoporous γ -Al₂O₃ membrane slightly decreased with increasing water vapor partial pressure ($p/p_0(\text{H}_2\text{O})$), and then, under $p/p_0(\text{H}_2\text{O}) = 1.0$, all the gas permeances dropped below the detection limit. It was experimentally confirmed that the degradation of the gas permeation properties could be due to the blockage of the gas permeable micro- and meso-pore channels by condensation of water molecules as permeate.

In contrast, the $V_a(\text{H}_2\text{O})$ measured at room temperature of the PCS-derived SiCH-based organic-inorganic hybrid was below 8 cm³(STP)g⁻¹, showing excellent hydrophobicity. By the 120 °C-melt impregnation of the low molecular weight PCS, the mesoporous γ -Al₂O₃ membrane was almost entirely modified with the PCS-derived SiCH-based organic-inorganic hybrid. The modified mesoporous γ -Al₂O₃ membrane exhibited stable gas permeations even under the saturated water vapor partial pressure

($p/p_0(\text{H}_2\text{O})=1.0$) at 50 °C: all the gas molecules of He, H₂ and N₂ kept high permeances of 1.2 to 3.0 × 10⁻⁶ mol m⁻² s⁻¹ Pa⁻¹.

In Chapter 3, to achieve the H₂-selectivity by the PCS-modification, mesopore channels of the highly hydrophilic γ -Al₂O₃ supported layer was filled with polymer-derived SiCH hybrids. For this composite membrane formation, another PCS derivative, allyl-hydro-polycarbosilane (AHPCS) was used. The AHPCS was successfully converted to highly cross-linked SiCH-based organic-inorganic hybrid with enhanced thermal stability via hydrosilylation between the Si-H and C=C in allyl groups presented within the AHPCS.

Even at a low temperature of 25 °C under dry condition, the composite membranes exhibited a unique $\alpha(\text{H}_2/\text{He})$ of 1.44–1.95, which was higher than the theoretical one (1.41) based on the Knudsen's diffusion, irrespective of heat treatment temperatures. The apparent activation energy for the H₂ permeation at 25–80 °C was 17.0–0.5 kJ mol⁻¹ and found to be smaller than that for He (20.3–1.4 kJ mol⁻¹). Moreover, the measurement of H₂ adsorption on an AHPCS-derived SiCH film at 30 °C revealed preferential H₂ adsorption. These results indicated a significant H₂ affinity of the SiCH-hybrid, which contributes to the experimentally observed unique $\alpha(\text{H}_2/\text{He})$ and the high H₂ permeance at 25–80 °C.

Under a H₂-N₂ (2:1) mixed gas flow and humid condition as a simulated syngas for the purification of solar hydrogen, the composite membranes exhibited a relatively high H₂ permeance of 1.0–4.3 × 10⁻⁷ mol m⁻² s⁻¹ Pa⁻¹ with a $\alpha(\text{H}_2/\text{N}_2)$ of 6.0–11.3. Further modification by the 120 °C-melt impregnation of PCS successfully improved the H₂-permeability of the 500 °C synthesized composite membrane by maintaining the H₂ permeance combination with improved $\alpha(\text{H}_2/\text{N}_2)$ as 3.5 × 10⁻⁷ mol m⁻² s⁻¹ Pa⁻¹ and 36.

In Chapter 4, a novel layered-composite membrane, the SiCH-hybrid top-layer supported on a mesoporous γ -Al₂O₃ layer was designed and synthesized. This layered composite structure design was expected to be essential to clarify the intrinsic gas permeation properties of the PCS-derived SiCH organic-inorganic hybrid itself.

The dominant mechanism for H₂ permeations through the PCS-derived top-layer was suggested as solid-state diffusion. The activation energy for the H₂ permeation was estimated as 5.8 kJ mol⁻¹ and was found to be slightly lower than that for the He permeation (5.9 kJ mol⁻¹). That is, the observed preferential H₂ permeation could be dominantly based on the solid-state diffusion through the dense SiCH-hybrid network having H₂ affinity.

The activation energy for N₂ permeation through the supported PCS membrane was estimated as 13.6 kJ mol⁻¹ by using the modified gas-translational diffusion (mGT) model. This value was compatible with that obtained by the conventional Arrhenius plot (11.9 kJ mol⁻¹). These results revealed that the N₂ permeation was activated diffusion through the micropore channels formed in-situ within the PCS-derived SiCH-hybrid network.

The enhanced H₂-permeability observed under the high-humidity conditions at 50 °C was explained by the synergistic effect of the preferential H₂ permeation through

the dense PCS top-layer network and blockage of N₂ permeation pathway by the permeate H₂O-induced plugging. As a result, when the H₂-N₂ (2:1) mixed feed gas was used for measuring gas permeances under saturated humidity at 50 °C, the N₂ permeance was below the limit of detection.

Future aspects

Polymer-derived SiCH-based organic-inorganic hybrid membranes developed in this study are promising candidates as advanced H₂-selective membranes for application to novel solar hydrogen production systems. Theoretically, without N₂ permeable channels, *i.e.* defect-free SiCH-hybrid could bring outstanding H₂-permeability.

Alternatively, it was found that, under high humidity condition, N₂ permeable micro- and meso-pore channels within the SiCH-hybrid/mesoporous γ -Al₂O₃ layered composite membrane were blocked by water molecules as permeate, which leading to the excellent H₂-selective performance.

Further research and development on this topic will be expected to evaluate the long-term stability toward the ideal syngas of H₂-O₂ (2:1) mixed gas under the humid condition for actual use with safety measures against explosion. Moreover, to increase a gas separation processing capacity, it is also required to develop a scale-up technology for the integrated membrane-module production.

List of Publication

Chapter 2

(1) “A hydrostable mesoporous γ -Al₂O₃ membrane modified with Si-C-H organic-inorganic hybrid derived from polycarbosilane”

Journal of Membrane Science, 598 (2020) 117799.

Miwako Kubo^a, Misako Kojima^a, Ryota Mano^a, Yusuke Daiko^a, Sawao Honda^a and Yuji Iwamoto^a

^a Department of Life Science and Applied Chemistry, Graduate School of Engineering, Nagoya Institute of Technology, Gokiso-cho, Showa-ku, Nagoya, 466-8555, Japan

Chapter 3

(2) “Hydrogen Selective SiCH Inorganic-Organic Hybrid/ γ -Al₂O₃ Composite Membranes”

Membranes, 10 (2020) 258.

Miwako Kubo¹, Ryota Mano¹, Misako Kojima¹, Kenichi Naniwa¹, Yusuke Daiko¹, Sawao Honda¹, Emanuel Ionescu², Samuel Bernard³, Ralf Riedel² and Yuji Iwamoto¹

¹ Department of Life Science and Applied Chemistry, Graduate School of Engineering, Nagoya Institute of Technology, Gokiso-cho, Showa-ku, Nagoya 466-8555, Japan

² Institut für Materialwissenschaft, Technische Universität Darmstadt, Otto-Berndt-Str. 3, 64287 Darmstadt, Germany

³ CNRS, IRCER, UMR 7315, University of Limoges, F-87000 Limoges, France

Chapter 4

(3) “Superhydrophobic polycarbosilane membranes for purification of solar hydrogen”
Separation and Purification Technology, 258 (2021) 117998.

Miwako Kubo^a, Kohei Okibayashi^a, Misako Kojima^a, Ryota Mano^a, Yusuke Daiko^a, Sawao Honda^a, Samuel Bernard^b and Yuji Iwamoto^a

^a Department of Life Science and Applied Chemistry, Graduate School of Engineering, Nagoya Institute of Technology, Gokiso-cho, Showa-ku, Nagoya 466-8555, Japan

^b CNRS, IRCER, UMR 7315, University of Limoges, F-87000 Limoges, France

Acknowledgements

I would like to express my appreciation to Professor Yuji Iwamoto (Nagoya Institute of Technology) for giving me the opportunity to carry out this study and for his thoughtful guidance as a supervisor and a chair.

I hereby express my deepest gratitude to Professor Shinobu Hashimoto (Nagoya Institute of Technology), Professor Wataru Sakamoto (Chubu University), and Associate Professor Isao Kagomiya (Nagoya Institute of Technology) for their advice and guidance on the details of this thesis.

I hereby express my deepest gratitude to Professor Dr. Ralf Riedel (Institut für Materialwissenschaft, Technische Universität Darmstadt), Doctor Emanuel Ionescu (Institut für Materialwissenschaft, Technische Universität Darmstadt) and Doctor Samuel Bernard (University of Limoges, Institute of research for ceramics, UMR, CNRS 7315) for their insightful comments and suggestions to my thesis.

I would like to thank Associate Professor Yusuke Daiko (Nagoya Institute of Technology) and Assistant Professor Sawao Honda (Nagoya Institute of Technology) for valuable discussions.

I am grateful to Kohei Okibayashi and Ryota Mano (graduates of Nagoya Institute of Technology), Misako Kojima and Kenichi Naniwa (graduate students of Nagoya Institute of Technology) for their high-quality investigations. And I would like to thank members of the Chemical Process Laboratory for their kindness. I hereby express my deepest gratitude.

Finally, I am grateful to co-workers, friends and my family for their supports.

久保美和子
January 2021